IDŐJÁRÁS

QUARTERLY JOURNAL
OF THE HUNGARIAN METEOROLOGICAL SERVICE

CONTENTS

VOL. 120 * NO. 2 * APRIL – JUNE 2016

IDŐJÁRÁS

Quarterly Journal of the Hungarian Meteorological Service

Editorial Office: Kitaibel P.u. 1, H-1024 Budapest, Hungary
P.O. Box 38, H-1525 Budapest, Hungary
E-mail: journal.idojaras@met.hu
Fax: (36-1) 346-4669

Indexed and abstracted in Science Citation Index Expanded™ and Journal Citation Reports/Science Edition
Covered in the abstract and citation database SCOPUS®

Subscription by mail:
IDŐJÁRÁS, P.O. Box 38, H-1525 Budapest, Hungary
E-mail: journal.idojaras@met.hu

IDŐJÁRÁS

Quarterly Journal of the Hungarian Meteorological Service
Vol. 120, No. 2, April – June, 2016, pp. 127–161

Effect of weather conditions on annual and intra-annual basal area increments of a beech stand in the Sopron Mountains in Hungary

Ernő Führer[1], **Márton Edelényi**[2], **László Horváth**[3*], **Anikó Jagodics**[1], **László Jereb**[2], **Zoltán Kern**[4], **Andrea Móring**[5], **Ildikó Szabados**[6], and **Zoltán Pödör**[2]

[1]*National Agricultural Research and Innovation Centre, Forest Research Institute, Paprét 17, 9400 Sopron, Hungary*

[2]*Institute of Informatics and Economics, Simonyi Károly Faculty of Engineering, Wood Sciences and Applied Arts, University of West Hungary, Bajcsy-Zsilinszky utca 9, 9400 Sopron, Hungary*

[3]*MTA-SZIE Plant Ecology Research Group, Szent István University, Páter Károly utca 1, Gödöllő, 2100, Hungary*
and
Hungarian Meteorological Service, Gilice tér 39, 1181 Budapest, Hungary

[4]*Institute for Geological and Geochemical Research, Research Centre for Astronomy and Earth Sciences, MTA, Budaörsi út 45, 1112 Budapest, Hungary*

[5]*Centre for Ecology and Hydrology, Penicuik, EH16 0QB, United Kingdom, and University of Edinburgh, Edinburgh, EH9 3JN, United Kingdom*
and
Hungarian Meteorological Service, Kitaibel Pál utca 1, 1024 Budapest, Hungary

[6]*Ministry of Agriculture Kossuth tér 11, 1055 Budapest, Hungary*

[*]*Corresponding author Email: horvath.laszlo.dr@gmail.com*

(Manuscript received in final form February 29, 2016)

Abstract—We studied the effect of meteorological parameters such as average monthly temperature and sum of precipitation on basal area increment (BAI) of a beech stand in the Sopron Mountains in subalpine climate in Hungary between 1985 and 2007. The applied multivariate regression analysis takes into account the influence of the weather conditions on increments also in the previous two years. Results indicated that precipitation generally stimulated the BAI in the studied stand, while above average temperature during the growing season depressed it. One of the dominant periods for growing of basal area is the autumn of the penultimate year when precipitation and temperature has positive and negative effect on increment, respectively. In the main growing period (spring-early summer) the previous year's precipitation has positive, while autumn temperature has negative effect. Current spring to early summer precipitation enhances the beech growth, and in contrary, the mean temperature in June-July has negative effect on the BAI. There is a breakpoint in the trend of meteorological variables at about 1999. A significant decrease was observed in the growth of beech in the summer months in the period of 2000–2007 compared to growth between 1985 and 1999 probably caused by the changed meteorological conditions. The maximum growth shifted from June to May, and the relative share of spring months in the BAI has increased since 2000. Drastic loss in increments can be observed in July and August, which was partly compensated in autumn. The long-term trend of annual BAI is continuously decreasing; comparing the two periods, the average yearly increments decreased from 21 cm^2 to 12 cm^2. According to forecasted climate change, not only further loss in growth but also drastic decay in vitality and tolerance can be expected for beech at this site over the 21st century.

Key-words: beech, growth, basal area increment, climate change, production

1. Introduction

At the beginning of the 1990's, several studies reported a more intensive growth of forests over Central Europe in the last third of the 20th century than before (*Pretzsch*, 1992; *Bräker*, 1996; *Spiecker et al.,* 1996; *Zingg*, 1996; *Kahle et al.*, 2008). Studying the reasons, it was found that the change in growth was related partly to the longer vegetation period (*Hasenauer et al.*, 1999), and partly to earlier blooming and leaf unfolding (*Menzel* and *Fabian*, 1999). Changes in the climatic conditions significantly enhanced the intensity of photosynthetic activity and respiration, resulting in change of growth (*Kozlowski et al.*, 1991; *Larcher*, 2001; *Somogyi*, 2008). However, the results are frequently contradictory when studying the relation of changing climate and tree growth in larger geographical scale. One of the reasons is that in the comparisons of different observations and measurements, the favorable or unfavorable climate conditions of the investigated areas were disregarded (*Mátyás et al.*, 2010). When water supply is not limited, the rising temperature can lead to substantial, even 50% increase in growth for beech in contrast to arid regions.

Numerous reports have been published concerning tree growth, especially for organic matter production of beech. These studies mainly focused on the causal relationships as consequences of changed climatic conditions. For

example, *Dittmar et al.* (2003) studied the effect of climate on the growth of beech stands in European mountainous (>800 m) and hilly (<700 m) regions. They found that temperature and precipitation in the summer of the given year have an inverse effect on annual growth. While in higher regions there is positive relation with increasing temperature, higher precipitation reduces the yearly growth. For lower regions these relations are just the opposite.

Cool and wet autumn at the year before was found to enhance the radial growth of beech for a Romanian stand (*Kern* and *Popa*, 2007). On the other hand, the late summer high temperature has negative influence on the growth.

Ježík et al. (2011) studied the influence of climate on the yearly production in the whole growing season, on the basis of biweekly dendrometer observation in Slovakia. They showed a positive effect of precipitation at the beginning of growing season, and this influence tends to be reverse with time during summer period with parallel growing importance of precipitation, especially at the end of summer and beginning of autumn.

Another Slovakian study reported positive effect of precipitation on beech growth in August in the previous year and in June-July in the same year; while temperature of the previous summer reduced the growth (*Petráš* and *Mecko*, 2011). Other investigations in Germany (*Scharnweber et al.*, 2011; *van der Maaten*, 2012) and France (*Michelot et al.*, 2012) pointed out positive effect of precipitation in the given year and negative influence of temperature.

In Slovenia (*Čufar et al.*, 2008), it was found that the May and July precipitation enhances the production significantly; similarly to the precipitation in August of the previous year. Other dominant climate parameters are the temperature minima in March and the maxima in August.

In this study we analyzed the weekly observations of basal area increment (BAI) in a beech stand for 22 years (1985–2007) in relation to the main meteorological parameters determining the growth, i.e., monthly mean air temperature and sum of precipitation. The length of data series allows a reliable correlation analysis between the increments and meteorological factors as well as to fit a model to the growth by multivariate linear regression analysis. A relatively rich literature can be found dealing with annual growth rates based primarily on tree-ring derived parameters, however, the strength of this study is the length of the intra-annual time series offering a unique opportunity to analyze the intra-annual growth trends of European beech on a 22-year timescale. The results will support evaluation of future growth expectations; namely, which climate components and in which periods have the greatest effect on the basal area increment of trees. The aim of this study is to evaluate this effect.

2. Methods and materials

2.1. Characterization of the site of investigation

During the selection of the test stand, it was a primary criterion that the tree species, i.e., the beech (*Fagus sylvatica* L.) should be important in the given landscape from both an ecological as well as forest economical point of view. The Sopron Mountains lie at the border of Austria and Hungary (*Fig. 1*), where beech is indigenous (*Magri*, 2008; *Führer et al.*, 2010). The forest type is *Oxalis acetosella* with a single crown-storied, completely closed beech forest. Its age at the beginning of the observations was 85 years based on the data of National Forestry Database in 1985. In the early 2008 the forest was harvested. Due to the forest restoration technology used between the World Wars, which succeeded in 5–15 years, there can be a difference of about 10 years among certain trees. The stand was on a slight, south-east facing slope at approximately 400 meters above the mean sea level. Coordinates are: 47° 39'20"N and 16° 28'58" E, the bedrock is gneiss, and the soil is a type of Luvisols according to the WRB 2014 classification system (*IUSS*, 2014). The climate is sub-alpine.

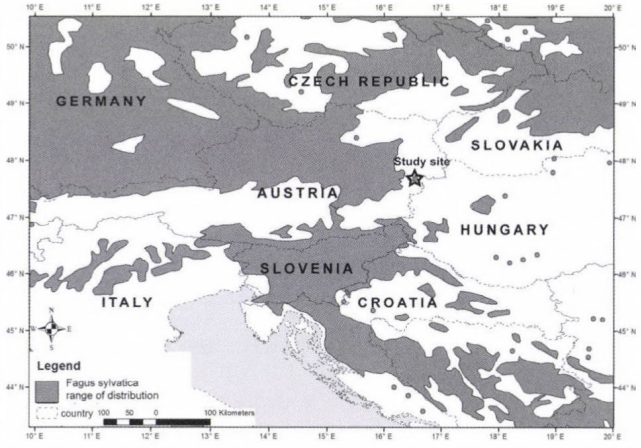

Fig. 1. Location of the study site and the distribution of beech (*Fagus sylvatica*). Distribution boundaries are retrieved from the *EUFORGEN* (2009) database.

The studied plot was a 50×50 m parcel, representing average stand in its characteristics. The height and diameter at breast height (DBH) of every tree were surveyed regularly. The stand was well growing; stem number was 362 pcs ha^{-1}, stand volume is 732 m^3 ha^{-1}, average DBH and height were 37 cm and 32 m, respectively.

Based on the survey – trunk by trunk –, we determined the social position (dominant, co-dominant, suppressed) of trees and the structure of the stand. Using the results of this analysis, we selected seven beech trees (*Table 1*) with average parameters, representative for the whole stand. Suppressed trees were not considered in the selection since their growth is heavily affected by their social status beside weather.

Table 1. Initial data of trunks equipped by dendrometers at the start of measurement; *d*=diameter at breast height (DBH); *BA* = basal area; *h* = tree height

Number of trunks	*d* (cm)	*BA* (cm^2)	*h* (m)
11	37.5	1103	32.0
14	38.2	1147	32.0
15	37.7	1117	33.0
16	33.2	864	31.5
19	41.7	1368	33.8
20	37.7	1117	32.2
21	37.8	1125	31.0
mean	**37.7**	**1120**	**32.2**

2.2. Dendrometer measurements

We installed Liming-dendrometers (*Liming*, 1957) on selected trees for weekly observations, and the change of perimeter over 22 years (1985–2007, without the year of 1998) was recorded. Following forestry practice, the bronze dendrometer-bands were installed permanently at breast-height. It should be emphasized that the circumferential change represents the total change in circumference outside the bark and not necessarily the actual wood increment. The largest source of noise could be the thermal expansion of the stem. Linear thermal expansion coefficient of bronze is 17–18 $\mu m\ m^{-1}\ °C^{-1}$ (*Hidnert* and *Krider*, 1947). Respecting that the monthly mean air temperature is similar at the start and at the end of yearly observations (March: 3.0±2.32 °C and November: 2.8±2.02 °C), differences in thermal expansion in March and November are practically negligible. For vegetation period, however, we estimated the anomaly caused by thermal expansion by comparing the circumferential increment of trees with thermal expansion. The calculated error was below 1 percent.

In spite of weekly observations, first of all we aimed to get information of monthly, seasonal, and yearly increments. Beside monthly growth increments of different stages of growing periods (initial: April, main: May-August, and final:

September-October), monthly meteorological parameters were also analyzed. The separation of the different growth stages (*Table 2*) enables the examination of change in these growth stages in relation to climate conditions over the long (more than two decades) observation period. To assess the effect of climate variability, investigation of yearly distribution of growth intensity is indispensable. Many papers have been published studying increments on a shorter (daily) time-scale (e.g., *Deslauriers et al.*, 2003; 2007a; 2007b). In these studies, with the applied measurement methodology, short-term growth of trees was separated from swelling and shrinkage caused by temperature and humidity. These observations are suitable to find deeper eco-physiological relationships. However, our observations, due to the potential, future application of the results in forestry practice, aimed the exploration of organic matter production of longer periods (within a year) as a function of weather parameters.

Table 2. Mean meteorological data (*p*: precipitation, *t*: temperature) in the reference (1961–1984) and observation (1985–2007) periods in different time intervals. The significance level in temperature differences was calculated by t-test.

Growing periods	Months												Measurement intervals						t-test for *t*
													1961–1984		1985–2007		1961–2007		
	1	2	3	4	5	6	7	8	9	10	11	12	*p* (mm)	*t* (°C)	*p* (mm)	*t* (°C)	*p* (mm)	*t* (°C)	significance level
Year	■	■	■	■	■	■	■	■	■	■	■	■	757	7.5	764	8.2	761	7.9	0.0013**
Dormant	■	■	■								■	■	211	–0.3	230	0.2	221	0.0	0.2023
Growing				■	■	■	■	■	■	■			546	13.1	533	13.9	540	13.5	0.0001**
Initial				■									62	7.6	54	8.3	58	8.0	0.0663*
Main					■	■	■	■					355	15.7	342	16.8	349	16.2	0.0001**
Intensive						■							100	15.5	89	16.1	95	15.8	0.9950
Critical							■						93	17.5	79	18.8	86	18.2	0.0200**
Final									■	■			129	10.7	137	11.0	133	10.9	0.3798

* indicates significance levels, below 0.1,
** indicates significance levels, below 0.05

2.3. Characterization of climate

For characterization of the climate of the test site – generally and for the examined period –, we used gridded climate data interpolated from homogenized monthly precipitation and temperature series derived from the network of the Hungarian Meteorological Service (*Szentimrey et al.*, 2010; *Lakatos et al.*, 2013). By homogenization the effect of any disturbance affecting

the measurements over the studied period is removed, keeping the signal of the climate change. Beside the climate characterizations, we attempted to find relationship between increments and monthly precipitation and temperature variations in the different years.

2.4. Evaluation methods

The basal area implement (BAI) is steadily increasing or asymptotically stabilizing for mature trees (*Bouriaud* and *Popa*, 2009; *Fekedulegn et al.*, 2003; *Muzika et al.*, 2004; *Piovesan et al.*, 2008). Since studied trees were obviously mature specimens (older than 85 years), from the beginning to the termination of observations the prevailing negative BAI trend (see Results) cannot reflect a biological trend; therefore, the otherwise mandatory detrending step was neglected and the raw BAI series were used.

According to a survey of European literature, both simple monthly mean weather data (*Dittmar et al.*, 2003; *Szabados*, 2006; *Kern* and *Popa*, 2007; *Maxime* and *Hendrik*, 2011; *Scharnweber et al.*, 2011) and data for longer periods (*Pichler* and *Oberhuber*, 2007; *Novák et al.*, 2010) were used in studying the relationship between weather conditions and growth of trees. The delayed effect of changing weather conditions are taken into account applying pre-defined periods within a year (*Briffa et al.*, 2002; *Büntgen et al.*, 2006; *Gutiérrez et al.*, 2011). Weather conditions of these periods can be represented by the combination (sums or averages) of parameters for different months. For this purpose, beside the analysis of monthly increments, we used the CReMIT method (Cyclic Reverse Moving Intervals Technique, *Pödör et al.*, 2014). A brief description is provided in the Appendix.

The basal area increment and organic matter production of trees are closely related to the transpiration (water flux) and photosynthetic activity. These physiological processes relate to leaves so the quantity and quality of foliage fundamentally affect the growth of trees. For deciduous species, the area and quality of leaves, reproduced year-by-year, depend on the quality and quantity of shoots. Many studies take into account the effect of meteorological parameters of the previous year (*Dittmar et al.*, 2003; *Di Filippo et al.*, 2007; *Kern* and *Popa*, 2007; *Maxime* and *Hendrik*, 2011; *Scharnweber et al.*, 2011; *Michelot et al.*, 2012; *Tegel et al.*, 2014). According to *Gruber* (2004), the number of shoots is determined by the circumstances of initiation of bud growth (primordia): i) this process is determined two years before the appearance of leaves on shoot; ii) the differentiation of primordia into short or long shoots happens a year before the formation of foliage. The more buds are developing long shoots the higher is the probability of higher leaf number; iii) the morphological quality of leaves (surface area and thickness) are determined in the given year, especially in April and May.

We were looking for relationships between climatological statistics and the increments of trees by linear regression analysis, and checked the significance of the found relationships by t-test.

2.5. Multivariate regression models

Based on the above calculations, we constructed multivariate linear regression models for all possible, at least two-component subgroups of independent variables. Using the significant ($p<0.1$) components, we generated all of the mathematically possible multivariate climate index (CI) models for temperature and precipitation and for the two components together on monthly and periodic level, and for the combination of these terms. Then, from the derived regression equations we selected the relevant and statistically significant ones ($p<0.05$). Beyond the ecophysiological considerations we selected them according to the value of the corrected coefficient of determination (R2adj). R2adj, in contrast with the simple coefficient of determination, takes into account the number of parameters as well as observations used in the model; hence, it is more suitable for comparison of multivariate models. In this way, taking into account the relevant and the most significant parameters, we derived the climate indices that have relatively the strongest influence on the increment over the 22 years.

2.6. Breakpoint analysis

A long data series usually includes significant breakpoints. This is true for not only our increment data series but also for our homogenized climate dataset, which – as we mentioned above – is still affected by climate change. During analyses we have to try to separate the data – though by controlled way – into sub-intervals as objectively and uniformly as possible by a principle equally applicable for all of variables. However, changes occur in longer time-interval we can still mark out breakpoints that relatively sharply separate the data series into fragments. There are different methods in the literature to mark breakpoints to detect shift in data series, e.g., by comparison of partial means by Students' t-test, by minimizing the standard deviation, by cumulative sum of anomalies, by Pettitts' non-parametric approach (*Pettitt*, 1979), and by analyzing the signal to noise ratio (*Sneyers*, 1992; *Mares* and *Mares*, 1994).

In our work, we applied the first approximation based on the theory that the difference in averages of sub-intervals separated by breakpoints are significantly higher than that of sub-intervals separated randomly. We tried to divide our meteorological time series into only two parts. To compare means we applied the t-test. This method supposes the normal distribution of meteorological datasets, which was verified by the Shapiro-Wilk test.

3. Results

3.1. Climate description of the test site

Between 1961 and 2007, the average yearly precipitation amount was 761 mm. The share of this was 540 mm in the growing period (April-October), while the rest (only 221 mm) was measured in the dormant period (November-March) (*Table 2*). This means that, beside the water stored in the soil in the dormant period, the water supply was enough in the physiologically active growing season for organic matter production. Regarding the share of precipitation in the different growing periods, the ratios were 11% in the initial growing period (58 mm), 65% in the main growing period (349 mm), and 24% (133 mm) in the final growing period. In the most intensive growing period in June, the average precipitation of 47 years was 95 mm month^{-1} (18%).

The annual mean air temperature at the test site was 7.9 °C. Average temperatures of growing and dormant periods were 13.5 and 0.0 °C, respectively. The average temperature in the different phases of growing season were: 8.0 °C in the initial, 16.2 °C in the main, and 10.9 °C in the final periods.

Due to their high temperature, July and sometimes August are the most critical months; in these months the mean monthly temperature exceeds the 18 °C, and the daily maxima are frequently between 30 and 35 °C. These high extremes substantially depress the photosynthetic activity. Weather conditions changed comparing the measurement period (1985–2007) to the previous years (1961–1984), especially in temperature, where an evident increase can be observed between the two periods (*Table 2*). The performed t-test shows that – excluding the dormant and final periods – there are statistically significant differences between the two examined periods at the $p<0.1$ significance level. The mean air temperature of the main growing season was higher by 1.1 °C in the measurement period. The difference is even higher in the critical month (July) when it is 1.3 °C, accompanied by a reduced amount (14% less) of precipitation. This means that the probability of drought was higher in the measurement period than before.

The mean growing season air temperature shows an evident (significant) change, especially for the period of BAI measurements (*Fig. 2*). Regarding the extremes, there were five years (1962, 1965, 1978, 1980, 1984) with lower than 15 °C mean temperature for the main growing phase during the reference period (1961–1984), while in the observation period there was not any years with the same mean temperature below 15 °C. Furthermore, in the main growing period of reference years (1961–84), year with average temperature higher than 17 °C occurred once (1983), whilst it was observed seven times in the following 23 years (1992, 1994, 2000–2003, and 2007). We can also see that the highest monthly mean temperature in the main growing season was 17.4 °C (1983) in the reference period, in contrast with 19.4 °C (2003) in the observation period.

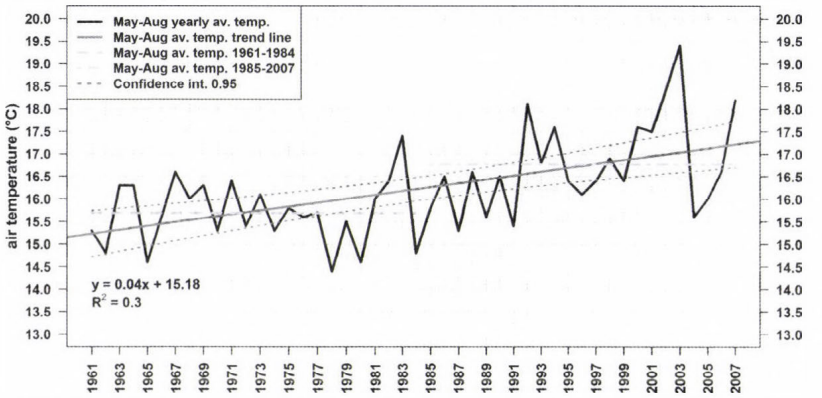

Fig. 2. Trend of average air temperature in the main growing season at the test site in the reference years (1961–1984) and in the observation period (1985–2007) (n=47, $p<0.001$).

The changes are represented also by the climate classification of the years according to forestry climate categories. Based on the forestry aridity index (FAI) developed for Hungary (*Führer et al.*, 2011), there were 18 years (75%) with beech climate category between 1961 and 1984, while in the observation period there was only 11 years (48%) (*Table 3*). Hence, drier and warmer years than beech climate, i.e., hornbeam-oak, sessile oak-Turkey oak, and forest-steppe climate were more frequent in the observation period (52%) than before (25%). It means that the climate did not evidently belong to beech category during the observation period. Respecting the whole 47 years we can conclude, that in most part of the period, the site can be characterized as beech climate zone (in 62% of years), whilst other years (38%) were characterized by warmer-drier weather conditions as *Table 3* shows.

Table 3: Share of years in different forestry climate categories according to Forestry Aridity Index by *Führer et al.* (2011)

Periods	Forestry climate categories			
	Beech	Hornbeam-oak	Sessile oak-Turkey oak	Forest-steppe
Reference years 1961–1984	18 (75%)	2 (8.3%)	2 (8.3%)	2 (8.3%)
Observation period 1985–2007	11 (48%)	9 (39%)	2 (8.7%)	1 (4.3%)
Total 1961–2007	29 (62%)	11 (23%)	4 (8.5%)	3 (6.4%)

There were substantial variations in the precipitation and temperature conditions among different months also in the observed period. On the basis of the above mentioned t-test and breakpoint analysis, we were looking for years in the period of 1985–2007, where precipitation and temperature averages before

and after the given year were significantly different concerning simple monthly and special periodic data (*Table 4*). We supposed, that when significant change is observed in the given year or one year before/after in monthly or periodic climatic variables determining the growth, a parallel change is expected in the basal area growth as well in the same period. In the vegetation period (April-October), significant change of temperature and precipitation were observed between 1990 and 2000 over the 22-year-long period of investigations. While in the months determining the growth, the precipitation amount was decreasing, upward shifts were observed for the temperature after the breakpoint. For example, the mean temperature in June was higher by 1.86 °C after 1992 and the average yearly precipitation amount were lower by 41 mm after 1998 than before.

Table 4. Breakpoint analysis of monthly precipitation and temperature data

Months	Precipitation (mm)				Temperature (°C)			
	Year	Before	After	Difference	Year	Before	After	Difference
4	2000	58.46	43.86	–14.60	1998**	7.82	9.08	1.26
5	2000**	101.09	66.42	–34.67	1993	12.84	14.07	1.23
6	1998**	112.88	71.43	–41.45	1992**	14.85	16.71	1.86
7	1996*	67.11	97.98	30.87	2001*	18.51	19.62	1.11
8	1990**	113.6	85.82	–27.78	1990*	17.53	18.82	1.29
9	1995	68.19	92.97	24.78	1995	13.95	13.05	–0.90
10	1990**	28.32	60.64	32.32	1998	7.99	9.01	1.02
9–10	1990**	91.72	148.06	56.34	1990	11.31	10.83	–0.48
5–8	2000	384.28	311.50	–72.78	1992**	15.99	17.14	1.15
4–10	2000*	574.45	498.87	–75.58	1998**	13.56	14.37	0.81

significance levels: *indicates $p<0.1$; **indicates $p<0.05$

3.2. Interannual, seasonal, and monthly variation of increments

The annual average increment calculated from weekly observations was 17.9 cm^2, with a minimum of 5.52 and a maximum of 31.3 cm^2 in the whole observation period. The growth begins in the first half of April and ends by the middle of October. Data in *Table 5* shows that 88% of organic matter is produced in the main

growing season, while its fractions are only 5.3% and 6.2% for the initial and final periods, respectively. These results are in accordance with previous results from Hungary (*Somogyi*, 2008; *Mátyás et al.*, 2010). Increments of different trees differ not only in yearly growth but also in the share in growth of the different growing periods. For example, the tree with poor growth (No. 14) showed that the less increment is produced in the main growth period the larger is the production in the initial and final period compared to an "average" tree.

Table 5. Absolute (BAI) and relative (RBAI) increments of beech trees in different growing periods in average and in cases of trees with the largest (No. 15) and the smallest (No. 14) growth

Growing periods	Average tree		Tree No. 15		Tree No. 14	
	BAI (cm^2)	RBAI (%)	BAI (cm^2)	RBAI (%)	BAI (cm^2)	RBAI (%)
Initial	0.94	5.3	1.74	5.5	0.56	10.2
Main	15.9	88.5	27.8	88.8	4.33	78.4
Final	1.11	6.2	1.81	5.7	0.63	11.4
Total	17.9	100	31.3	100	5.52	100

BAI records showed quite strong coherence among the measured trees for all seasons and the full period as well. The temporarily stable and good coherence is substantiated by the high mean within-tree correlation coefficients (at least $r=0.37$ in all cases at $p=0.05$ or lower significance level), which validates that a common signal is captured by the averaged BAI record (*Fig. 3*). The annual BAI shows a significant decreasing trend during the investigated period. According to the findings of *Fekete* (1958) and *Mendlik* (1967), beech stands between the ages of 80–120 years grow slowly but significantly in basal area. A negative trend in BAI of mature trees is a strong indication of a stress induced decline in tree growth (*Pedersen*, 1998; *Jump et al.*, 2006; *Peñuelas et al.*, 2008; *Piovesan et al.*, 2008). The trend can be correlated with the evident temperature increase in the given period (*Fig. 2*).

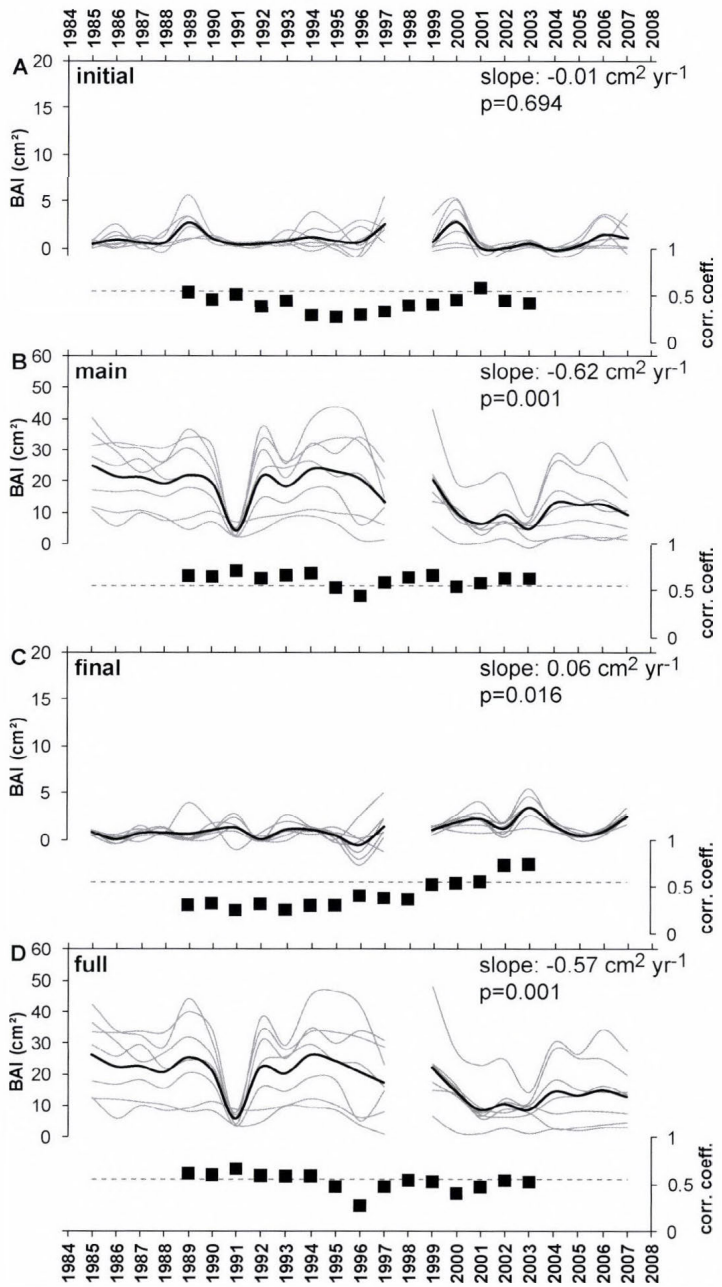

Fig. 3. Aggregated basal area increment (BAI) records of the 7 monitored beech trees and their coherence. The measurement records (A: initial period, B: main period, C: final period, D: full growing period) are shown as thin grey curves. The slope of the linear regression and the corresponding p-value are displayed at the top right corner. The average coefficients of between-tree moving window correlation calculated in 9-year windows are shown below the curves (black square). Dashed horizontal lines show the p=0.1 level.

The year of 1991 was extraordinary, because the mean growth was only 5.77 cm^2 that is only one third of the multi-year average (*Table 6*). In this year, the share of growth in the initial and final periods was higher than the average: 8% (0.44 cm^2) and almost 23% (1.31 cm^2), respectively, while in the main period it was only 70% (4.02 cm^2).

Table 6. Absolute (BAI) and relative (RBAI) yearly increments in different growing periods in average and in a wet-cool (1991) and a dry-warm (2003) year

Growing periods	1985–2007		1991		2003	
	BAI (cm^2)	RBAI (%)	BAI (cm^2)	RBAI (%)	BAI (cm^2)	RBAI (%)
Initial	0.94	5.3	0.44	7.6	0.52	6.0
Main	15.9	88.5	4.02	69.7	6.09	70.8
Final	1.11	6.2	1.31	22.7	1.99	23.2
Total	17.9	100	5.77	100	8.60	100

Fig. 3 shows that in the years 1991 and 2001–2003, the yearly increment values were well below the average. The reason for rather low growth in 1991, beside biological reasons, can be the extreme weather in that year. The yearly precipitation was 849 mm, 12% higher than the multi-year average. However, the distribution of precipitation among the growing phases was unfavorable. The precipitation amount in the winter half-year (November 1990–April 1991), which is an essential water supply for the growth in April, was 190 mm, 32% less than the 47 year average (279 mm). It suggests that recharge of the shallow groundwater reservoir of soil in the dormant and the initial periods were only partial.

In the following two months (May–June), when growth is generally the highest, the precipitation was 329 mm, 84% higher than the multi-year average (178 mm). In the same time, the mean monthly air temperature in these months was 14.4 °C lower by 2.2 °C than the average. Consequently, because of suppressed transpiration induced by the higher humidity and the lower temperature, the intensity of photosynthesis reduced as well, resulting in lower assimilation. This deficit in growth was not recovered in later phases not even with the 330 mm precipitation in the rest of the growing cycle. The growth in the final growing period is 23%, which ratio is systematically higher than that of the 22-year average (6.7%).

The year of 2003 was extreme as well. The yearly precipitation was only 558 mm, 27% less as usual. While precipitation in the dormant and initial periods (216 mm) was similar to the long-term mean (221 mm), in May and June, in the intensive period was only 108 mm, 39% less than the average

(178 mm). At the same time, the average monthly temperature in these months was 18 °C in contrast to the average, 14.5 °C. The means of daily maxima were 21 and 25 °C in May and June, respectively, so drought and heat stress were accompanied, suppressing the organic matter production. The BAI in this year was 8.6 cm^2, shared by 6% in the initial period, and 71% in the main growing period (*Table 6*). It seems that trees tried to partly compensate the loss of production by the largest growth detected for the final period (1.99 cm^2) in this year (*Fig. 3c*).

From the analysis of different years it seems, that the yearly BAI showed a great variability not only year-by-year but also in share among the different growing periods (*Fig. 4*). Generally, when the increment is less in the main period, the ratio is higher in the final stage. This kind of relationship cannot be found in growth between the initial and the main period. The highest growth in the initial period (2.84 cm^2, and 20%) was observed for the year of 2000. This phenomenon can be attributed to the favoring weather conditions, i.e., in the dormant and initial periods the precipitation was 340 mm in total, 21% higher than the 47-year average. The water supply from soil was enough to start the physiological processes, and at the same time the mean monthly temperature was higher by 1.1 and 3.4 °C than the averages (2.9 and 7.9 °C) in March and April, respectively, both favoring the early and intensive growing.

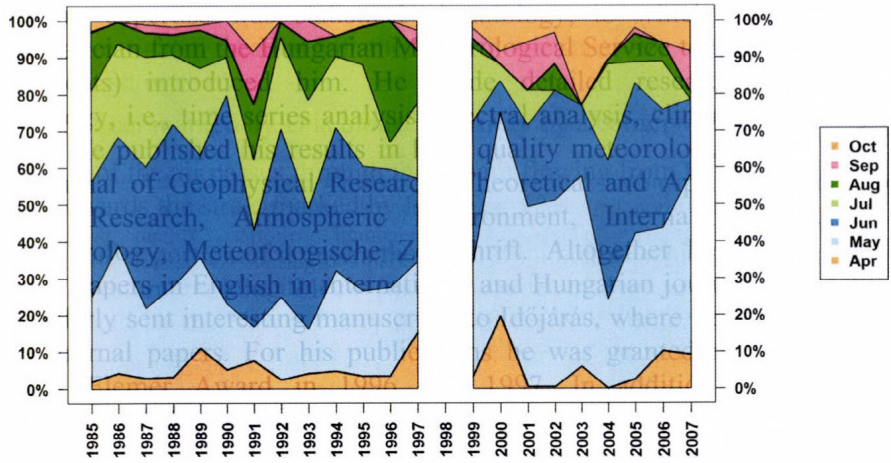

Fig. 4. Share of relative monthly increments of different years.

The length of the initial period was relatively short in agreement with observations in the last two decades: the transition period between winter and summer passes quickly. On the other hand, the main growing period became warmer and warmer, and in July and August, the photosynthesis frequently

halted almost completely because of the high daily temperature and low humidity (*Lin et al.* 2012). Later, when hot days were over, it starts again, especially from the beginning of fall to the middle of it. Measurements confirm that ratio of organic matter produced in the final growing cycle is higher and higher, and the magnitude is in a close relationship with growing conditions prevailed in the previous periods; i.e., when organic matter production is low in the main period it is higher than the average in the final cycle. While BAI in the initial period does not show any significant variation during the 22 years, growth significantly decreased in the main and increased in the final periods (*Fig. 5*).

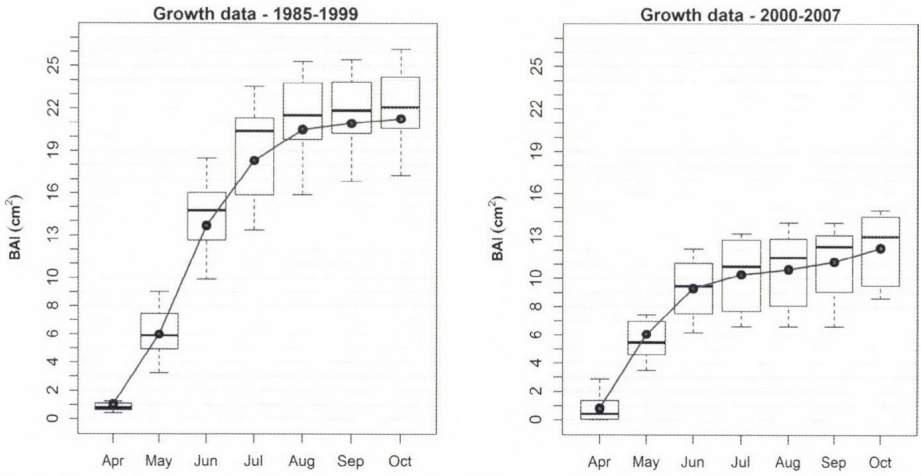

Fig. 5. Cumulative average monthly increments in the periods of 1985–1999 and 2000–2007.
circle: arithmetic mean,
horizontal black line: median,
bottom and top of boxes: lower (Q1) and upper (Q3) quartiles,
error bars: minima and maxima when they are within the 1.5 times of interquartile range (IQR); otherwise the 1.5 times of IQR from Q3 and Q1.

Analyzing the monthly increments separately, we can observe the highest average growth in June (6.08 cm^2), followed by May (5.05 cm^2), July (3.31 cm^2), and August (1.52 cm^2) during the examined 22 years. On the basis of breakpoint analysis with exception of May, September, and October, significant changes are detected between 1999 and 2001 in each month in the main growing period (May-August), and in the whole vegetation period (April-October) (*Table 7*). The breakpoint analysis clearly shows significantly higher mean increments in years before breakpoint in summer, while the trend is just opposite

for autumn. For this reason, we analyzed separately the increments of the 1985–1999 and 2000–2007 time intervals. The mean monthly increments differed significantly in the two periods (*Fig. 6*), not only in absolute value but also in the share of the month in the total yearly growth. In years before breakpoint (1985–1999), the highest average increment was detected in June (7.69 cm^2), followed by increments, in order: May: 4.94 cm^2, July: 4.64 cm^2, August: 2.19 cm^2, April: 1.04 cm^2, September: 0.45 cm^2, and October: 0.30 cm^2. In contrast, after the breakpoint (2000–2007), the highest mean BAI appeared earlier, in May: 5.23 cm^2. It means a 6% increase compared to the monthly averages in earlier years. However, it was followed by a dramatic decrease in June, July, and August: 3.26; 0.99; and 0.37 cm^2 (–57; –79; –83% changes), respectively, that was only partly compensated by the slight growth enhancement detected in September (0.52 cm^2) and October (0.98 cm^2). Data clearly showed a drastic decrease in average yearly increments (from 21.19 cm^2 to 12.15 cm^2) in the second period. While the trend of growing does not differed substantially in April-May (*Fig. 3a*), the cumulative increments decreased by 32; 44; 48 % in June, July, and August of the second time interval, respectively (*Fig. 5*). The cumulative deficit in increments till August (48%) compared to the first period is partly compensated (down to 43%) by the relatively higher increments in September and October.

Table 7. Break-point analysis of increments

Month	Brake-point (year)	Increment (cm^2)		
		Before	After	Difference
4	2001*	1.16	0.51	–0.65
5	1990	5.92	4.79	–1.13
6	2000**	7.69	3.26	–4.43
7	2000**	4.64	0.99	–3.65
8	1999**	2.31	0.39	–1.92
9	1990	0.28	0.53	0.25
10	1994**	0.24	0.79	0.55
9, 10	1990*	0.62	1.17	0.56
5, 8	2000**	19.45	9.85	–9.60
4, 10	2000**	21.42	12.15	–9.27

significance levels: *indicates $p<0.1$; **indicates $p<0.05$

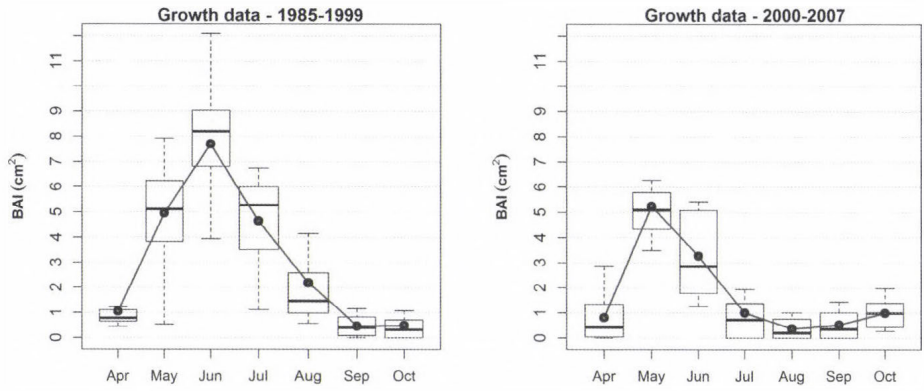

Fig. 6. Absolute average monthly increments in the periods of 1985-1999 and 2000-2007. Legends: refer to *Fig. 5.*

3.3. Relationship between increments and meteorological parameters

For evaluation we applied the linear correlation analysis based partly on monthly and partly on periodic (mean temperature and precipitation sum of a few neighboring months) components (CReMIT). Significant relations between them are compiled in *Table 8*. From correlation coefficients (r), the direction and the rate of the effect can be studied.

Table 8. Significant correlations between BAI and monthly (M) or periodic (P) meteorological variables

M	t_{-2} (Oct)	t_{-1} (Jun)	t_{-1} (Nov)	t (Jun)	p_{-2} (Jun)	p_{-2} (Nov)	p_{-1} (May)	p (Apr)	p (Jun)
r	–0.41*	–0.42*	–0.53**	–0.53**	0.50**	0.49**	0.44**	0.45**	0.46**

P	t_{-2} (Oct-Nov)	t_{-1} (Apr-Jun)	t_{-1} (Oct-Nov)	t (Jun-Jul)	p_{-2} (Jul-Sep)	p_{-2} (Oct-Nov)	p_{-1} (May-Jun)	p (Feb-Apr)	p (Apr-Jun)
r	–0.44**	–0.45**	–0.66**	–0.43**	–0.47**	0.47**	0.44**	0.47**	0.42*

r=correlation coefficient; *t*=temperature; *p*=precipitation; significance levels: *=p<0.1; **= p<0.05 lower indices –1 and –2 refer to the year before and two years before, respectively

It depends on many factors which month or time period has significant effect on the growth of European beech. *Jump et al.* (2010) and *Mátyás* (2010) found increasing climatic effect at the trailing edges compared to other sites. *Maxime* and *Hendrik* (2011) pointed out the importance of elevation above sea level in the investigation of climate and production relationship. *Dittmar et al.* (2003) showed that relations clearly depend on the elevation. These facts support the possible effects of site-specific features in relationships in many cases.

For monthly components (m), there are significant inverse relationships at 90% probability level between BAI and temperature in October two years before ($t_{-2(Oct)}$) and in June one year before ($t_{-1(Jun)}$), as well as at 95% level for temperature in November one year before ($t_{-1(Nov)}$) and in June in the same year ($t_{(Jun)}$). The negative sign indicates that the temperature conditions in the examined stand are out of optimum range for the beech species (*Čufar et al.*, 2008; *Petras* and *Mecko*, 2011; *Scharnweber et al.*, 2011; *Michelot et al.*, 2012). For monthly precipitation correlations are positive at 95% probability level in all cases (two years before in June: $p_{-2(Jun)}$ and November: $p_{-2(Nov)}$, one year before in May: $p_{-1(May)}$, and in the same year in April: $p_{(Apr)}$ and June: $p_{(Jun)}$), i.e., the higher precipitation favors growth (*Lebourgeois et al.*, 2005; *Werf et al.*, 2007; *Čufar et al.*, 2008; *Prislan et al.*, 2013). Significantly affecting components can be observed in the main periods of important physiological processes (budding, defoliation in previous year, organic matter production).

We handled maximum three consecutive months as a period. Over these periods we calculated average temperatures and precipitation sums. It can be noted that the months that are dominant in correlation for monthly components are also dominant in the periodic components.

The results of the multivariable linear regression analysis are displayed in *Table 9*, where beside the corrected coefficient of determination (R^2_{adj}), the simple coefficient of determination (R^2) are also indicated. The R^2_{adj} considers the number of independent variables in the models.

Based on the climate indices, CI_{tm} and $CI_{pm,}$, calculated from only monthly data, it can be concluded that monthly precipitation ($R^2_{adj} = 0.65$) has higher influence on growth than monthly temperature ($R^2_{adj} = 0.44$). This supports the finding of *Gutiérrez et al.* (2011), i.e., temperature affects the organic material production in shorter (days, weeks) periods than that of precipitation. The same findings were published firstly by *Ellenberg* (1988) and justified later also by others (*Geßler et al.*, 2007; *Werf et al.*, 2007). The relation is more significant, $R^2_{adj}=0.71$, in the case of joint climate index (CI_{tpm}), regarding monthly temperature and precipitation data.

Table 9. The selected climate index models (CI)

Model	R^2_{adj}	R^2
$CI_{tm} = -1.44 \times t_{-1(Nov)} - 1.79 \times t_{(Jun)} + 49.82$	0.44	0.49
$CI_{pm} = 0.10 \times p_{-2(Nov)} + 0.06 \times p_{-1(May)} + 0.07 \times p_{(Apr)} + 0.03 \times p_{(Jun)} - 1.04$	0.65	0.70
$CI_{tpm} = 0.09 \times p_{-2(Nov)} + 0.06 \times p_{-1(May)} - 0.87 \times t_{-1(Nov)} + 0.04 \times p_{(Apr)} - 0.9 \times t_{(Jun)} + 22.25$	0.71	0.77
$CI_{ts} = -2.01 \times t_{-2(Oct-Nov)} - 1.28 \times t_{-1(Apr-Jun)} - 2.80 \times t_{-1(Oct-Nov)} - 0.04 \times t_{(Jun-Jul)} + 61.18$	0.55	0.62
$CI_{ps} = 0.06 \times p_{-2(Oct-Nov)} + 0.04 \times p_{-1(May-Jun)} + 0.02 \times p_{(Apr-Jun)} - 1.39$	0.45	0.54
$CI_{tps} = -0.03 \times p_{-2(Jul-Sep)} - 2.13 \times t_{-2(Oct-Nov)} - 2.88 \times t_{-1(Oct-Nov)} + 0.04 \times p_{(Feb-Apr)} - 0.02 \times p_{(Apr-Jun)} - 0.42 \times t_{(Jun-Jul)} + 57.83$	0.65	0.73
$CI_{tpms} = 0.96 \times t_{-2(Oct)} + 0.1 \times p_{-2(Nov)} - 1.34 \times t_{-1(Apr-Jun)} + 0.03 \times t_{-1(May-Jun)} - 1.31 \times t_{-1(Oct-Nov)} + 0.06 \times p_{(Apr)} - 0.01 \times p_{(Jun)} - 0.98 \times t_{(Jun)} + 37.84$	0.71	0.81

t=temperature, p=precipitation, m=monthly, s=seasonal
lower indices –1 and –2 refer to the year before and two years before, respectively

The coefficient of determination calculated for the periodical additive temperature climate index (CI_{ts}) is $R^2_{adj} = 0.55$, a little higher than that for monthly components. In contrast, the same coefficient for precipitation (CI_{ps}) is lower than for the monthly components, $R^2_{adj} = 0.45$. That is, for periodic climate indices the temperature has higher influence than precipitation. When considering the additive effect of periodic temperature and precipitation parameters (CI_{tps}), we can conclude that the relation is less significant than for monthly components ($R^2_{adj} = 0.65$).

Corrected coefficient of determination of model calculated both with monthly and periodic components (CI_{tpms}) gives a strong relationship with $R^2_{adj} = 0.71$. Temporal variations of observed and modeled basal area increment are presented in *Fig. 7* for models of CI_{tpm}, CI_{tps}, and CI_{tpms}. Except of a few years (e.g., 1991), it is evident that observed values fits well within the upper and lower confidence limits of the models.

We have analyzed the relationship between monthly increments and meteorological variables. As we pointed out in the breakpoint analysis, year-by-year changes in meteorological conditions may be reflected in changes of increments. From results in *Table 7* it can be seen, that, e.g., substantial decrease occurred in June in increments from 2000. Two years before this decrease, a significant precipitation decrease started in June (*Table 4*, *Fig. 8*) accompanied by a delayed increase in growth in the following years. Mean temperature in June still increased well before this decrease (since 1992), probably also affecting the increments in June of later years. Therefore, we examined by linear regression analysis the relationship between increments and meteorological variables (precipitation, temperature) in each month of the vegetation period. *Table 10* shows significant relationships in increments as the function of mean

temperature and precipitation in May and June. In May, July, and August, the joint effect of temperature in the given month and a month before in the increments is more significant than that of the given month. The sign of correlation coefficient shows a positive effect of temperature in the monthly growth in spring (April, May), while later, rising temperature does not favor the increments.

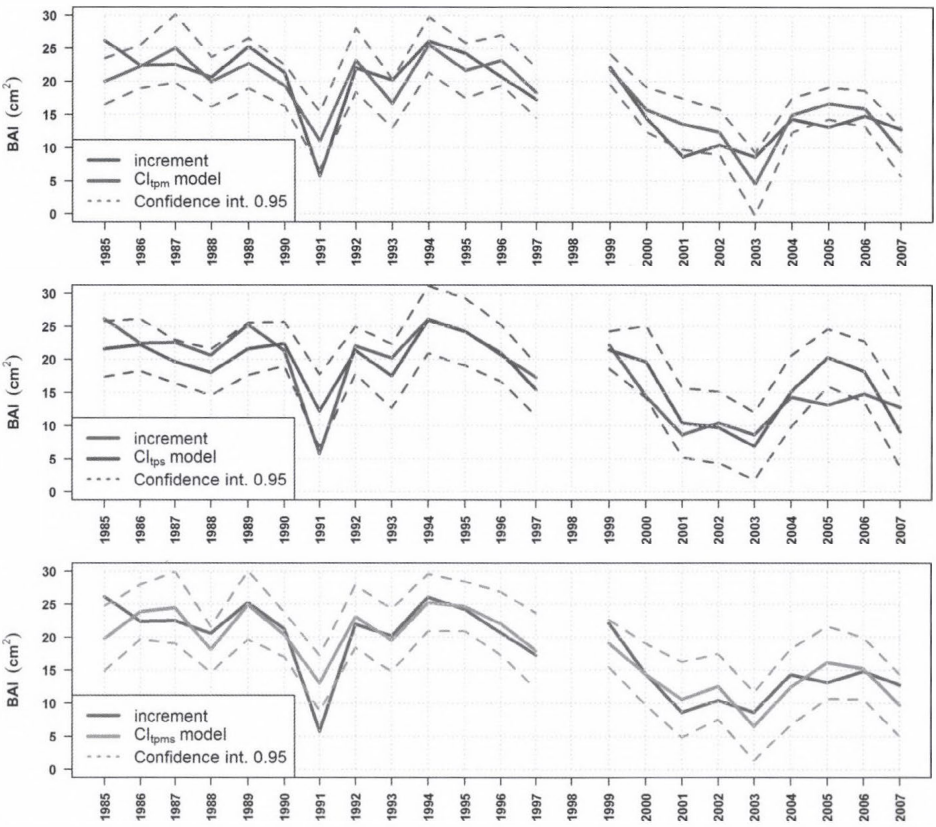

Fig. 7. Variation of the measured and modeled basal area increment (BAI) for models of CI_{tpm}, CI_{tps}, and CI_{tpms} (n=22, $p<0.001$).

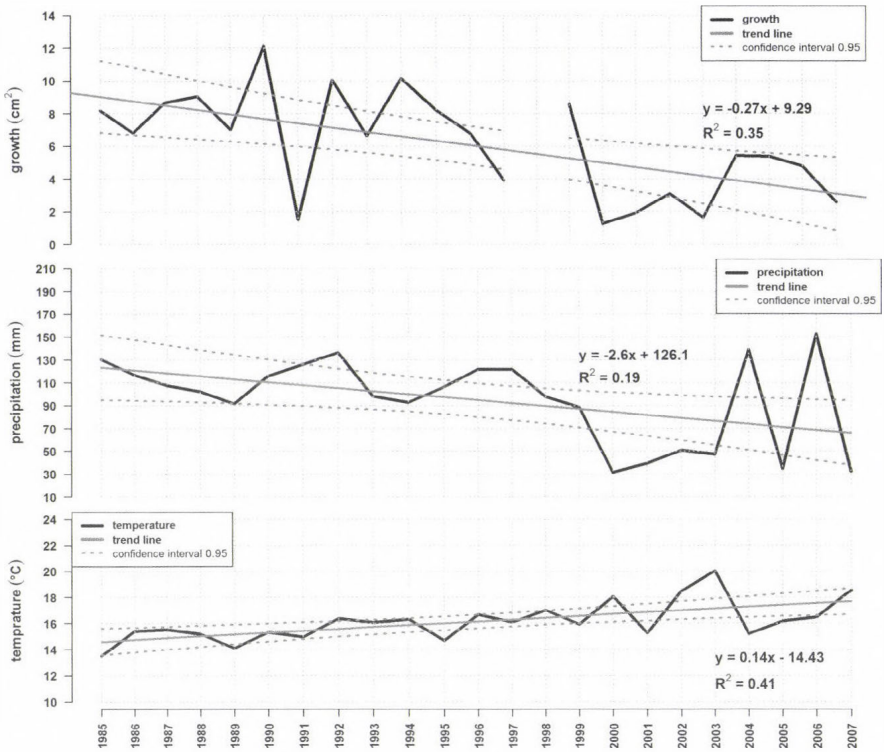

Fig. 8. Trend of increments (n=22, p<0.01), mean temperature, and precipitation in June (n=23, p<0.001).

Table 10. Correlation coefficients (r) of regression between monthly increments and meteorological variables

Meteorological parameters	**Months**						
	4	**5**	**6**	**7**	**8**	**9**	**10**
Precipitation in the given month	0.301	–0.371*	0.507**	–0.245	0.264	0.415*	–0.049
Precipitation in the given and preceding months	0.266	–0.125	0.250	0.236	0.288	0.167	–0.161
Mean temperature in the given month	0.196	0.392*	–0.506**	–0.051	–0.321	–0.273	–0.048
Mean temperature in the given and preceding months	0.315	0.653**	–0.412*	–0.488**	–0.489**	–0.157	–0.030

significance levels: *indicates $p<0.1$; **indicates $p<0.05$

4. Discussion

The largest growths were detected in May and June in the studied beech stand over the studied 22 years. Average BAI observed were 5.02 and 6.08 cm^2 (28 and 34%) in May and June, respectively (alltogether 62% of yearly growth). While in May trend could not be observed for growth ($y = -0.0018 \times x + 5.0698$, R2=4x 10–5), there was a negative significant trend in June (*Fig. 8*; $y = -0.27 \times x + 9.29$, R2=0.35). As a consequence, while in the first 11 years of observation the mean BAI in June was almost the double of that of May (8.03 vs. 4.84 cm2), in the second 11-year period growth in May exceeded the production of June (5.20 vs. 4.12 cm^2). This phenomenon was related to the positive trend of average temperature and the negative trend of increments in June over the years (*Fig. 8*) (there is no significant trend for precipitation in June). In contrast, in May there is a positive relationship between the BAI and the mean temperature (*Fig. 9*). This shows that the intensive growing period started earlier in the 2000s, which projects an increase of sub-Mediterranean climate influence at the observation site, obviously modifying the spread of beech. Our results underline the determining effect of May and June in organic matter production of beech in agreement with other studies from Europe (*Dittmar et al.*, 2003; *Lebourgeois et al.*, 2005; *Di Filippo et al.*, 2007; *Garamszegi* and *Kern*, 2014).

It is worth also mentioning, that the total BAI loss and the increased BAI in the final period is accompanied with opponent changes in growth signal coherence. Mean within-trees correlation slightly decreased for the total and significantly increased for the final period following the detected breakpoint.

As it can be seen from the calculated regressions (*Table 8*) as well as from the climate indices (*Table 9*), increments of trees are influenced by the climate of different months or periods not only in the given year but also in the previous two years. Analyzing the data, the following general tendencies can be seen. Taking into account the sign and magnitude of coefficients in the tables, the precipitation has positive effect on growth while the influence of temperature is the opposite.

Precipitation in autumn (October, November) two years before a given year has generally positive effect on girth growth. In the previous year, positive influence of precipitation can be observed in spring in the most intensive growing periods (May, June). In the given year, the precipitation – in spite of a few exceptions – has dominantly positive effect in the period of February-July, especially in the initial growing period (April) and at the beginning of the main growing period (May, June) when majority of increment is realized. Negative influence of air temperature is realized in autumn (October-November) one or two years before the given year but the effect of temperature can also be observed in spring-summer one year before, and it is evident in the given year in early summer, mostly in June.

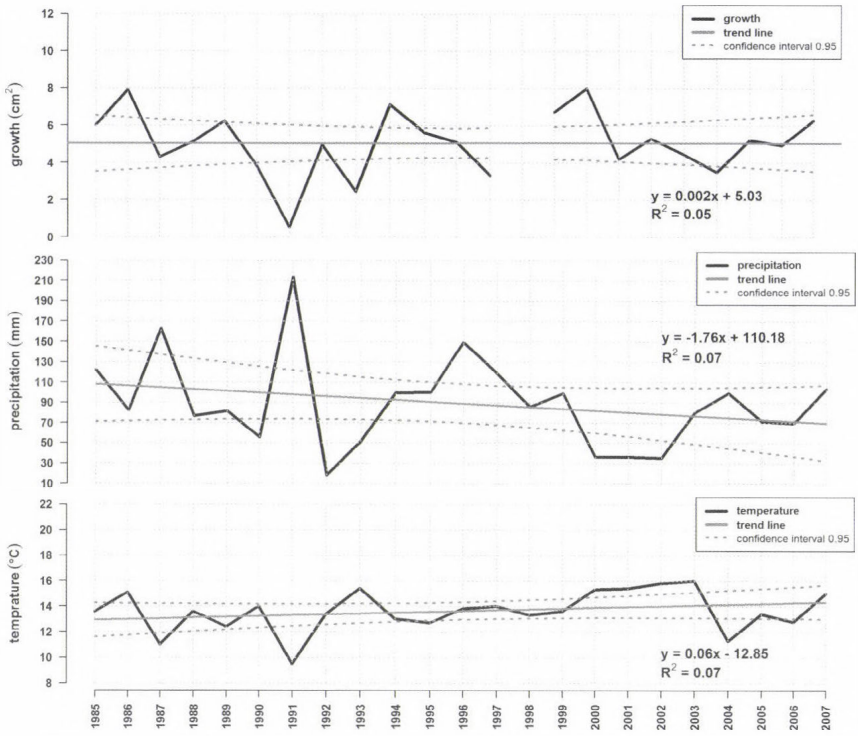

Fig. 9. Trend of increments (n=22, $p<0.01$), mean temperature, and precipitation (n=23, $p<0.001$) in May.

The examined stand according to the forestry aridity index (*Führer et al.*, 2011) definitely belonged to the beech climate zone. However, since the end of the 1980s, a drastic change was observed. The sum of precipitation decreased by 10%, nearly by 3%, and by 14% in the initial, main, and final growing stages, respectively, during the 1991–2007 period compared to the 1961–1990 reference period (*Table 11*). These changes are already higher than the forecasted data for 2035–2065 calculated by the REMO model (*Gálos et al.*, 2007). At the same time, temperature showed a steady increasing trend in almost each different growing (sub)period within the year. The change in the initial period is 0.7 °C, while in the main growing period it is as high as 1.2 °C. If the tendencies of precipitation and temperature keep on following the climate change scenario of the REMO model, living conditions of beech in the surroundings of the monitored stand will change to such an extent that can lead to not just increment decrease (*Piovesan et al.*, 2008), but also potential extinction.

Table 11. Climate parameters in the reference period (1961–1990), in the period of investigation (1991–2007), and forecasted by REMO model (*Gálos et al.*, 2007) (2035–2065) in absolute and relative values

Growing Period (Months 1–12)	Time intervals (years)									
	1961–1990		1991–2007				2035–2065			
	p (mm)	*t* (°C)	*p* (mm)	d*p* (%)	*t* (°C)	d*t* (°C)	*p* (mm)	d*p* (%)	*t* (°C)	d*t* (°C)
Year (1–12)	753	7.6	774	2.8	8.4	0.8	775	2.9	9.5	1.9
Dormant (11–3)	216	–0.2	228	5.5	0.4	0.6	238	10.2	1.7	1.9
Growing (4–10)	536	13.2	547	2.1	14.1	0.9	537	0.2	15.1	1.9
Initial (4)	60	7.7	54	–10.0	8.4	0.7	63	5.0	9.0	1.3
Main (5–8)	352	15.8	343	–2.6	17.0	1.2	332	–5.7	17.7	1.9
Final (9–10)	124	10.8	150	21.0	11.0	0.1	142	14.5	13.2	2.4
Intensive (6)	100	15.3	86	–14.0	16.5	1.2	91	–9.0	17.4	2.1

The coinciding breakpoint detected in the series of climate and BAI suggests that the significant change in climate parameters affected the production as well. Both the strength and the sign of the relationship between the climate and the growth data changed, as it is illustrated by the correlation coefficients between the BAI and the FAI (*Führer et al.*, 2011) or EQ (*Ellenberg*, 1988) drought indices (*Table 12*) separately in the two periods until and after 1999. While climate was favoring for growth of beech (1985–1999) represented clearly by beech climate (FAI=4.01), only the monthly precipitation sum in FAI from May to August had significant influence on the yearly production. The increase of summer precipitation negatively affected the yearly growth in this period. After the climate became dryer and warmer from 2000, the mean FAI has changed to the border of beech/hornbeam-oak climate (FAI=4.82), and this enhanced climate stress has stronger effects on the yearly growth. These results support the observations of *Mátyás* (2010) and *Garamszegi* and *Kern* (2014) who pointed out the increasing climate sensitivity of beech towards the border of beech/hornbeam-oak climate. This manifests not only in the decline or the fall of trees but also in the decrease of growth accompanied with unfavorable economic impact, i.e., the decreasing profitability of forest management (*Führer et al.*, 2013).

An earlier basal area increment survey performed near the town of Gödöllő, Hungary, between 1974 and 1983 (*Járó* and *Tátraaljai*, 1985) for different species (ten deciduous and seven pine stands) showed that the growth generally started before the middle of April for all species of deciduous trees and ended before the end of August. Growth in September was observed in the case of only a few species, such as black locust, hornbeam, and 'I-214' poplar,

and it lasted only for a few days. For pines, the growth started two weeks earlier and ended generally in the first third of October. Thus, the average length of the growing period for deciduous species was 139 and for pines it was 190 days.

Table 12. Correlation coefficients between average yearly BAI and drought indices (FAI, EQ); their precipitation (P_{FAI}, P_{EQ}) and temperature (T_{FAI}, T_{EQ}) components in periods of 1985–1999 and 2000–2007

Periods	P_{FAI}	P_{EQ}	T_{FAI}	T_{EQ}	FAI	EQ
1985–1999	–0.50*	–0.23	0.10	0.15	0.29	0.27
2000–2007	0.48	0.40	–0.75**	–0.37	–0.69*	–0.55

significance levels: * indicates $p<0.1$; **indicates $p<0.05$

According to our phenological observations parallel with BAI measurements in the Sopron Mountains, the beech came into leaf from the middle of April and ended at the end of the same month. The period of autumn discoloration of leaves ranged between the beginning and the end of October, while defoliation occurred till the middle of November. It means, that the average length of time period for photosynthetic, i.e., growing processes was 173 days.

Since the start of the initial growing period was the same in the Gödöllő region for 1974–83 as at the Sopron Mountains for 1985–2007, and the lengths were equally two weeks for both regions, the reason for the difference between the two growing periods is the different length of the main growing periods. In the Gödöllő region, the 103-day-long main growing period lasted till the middle of July, when 93.3% of organic material was produced. In the case of beech stand in the Sopron region the same portion of organic matter (93.3%) was produced, but it occurred till the end of August over a 140-day-long main growing period. The final period was of the same length at both areas, finished at the end of August and in the first third in October at Gödöllő and Sopron regions, respectively. The reason for the different length or timing of the main and final cycles, beside the differences in species, is the difference in climate conditions. Namely, whilst the average yearly precipitation in the Gödöllő region was 544 mm and the yearly average temperature was 9.5 °C, these values were much higher for precipitation (764 mm) and lower for temperature (8.2 °C) for the Sopron area in the measurement periods, i.e., the Gödöllő area is drier and warmer compared to the Sopron Mountain region.

Similar results to the Sopron region was reported for an old-growth beech near Solling, Germany (*Schulze*, 1970; *Schulze et al.*, 1977), where the number of days with positive carbon dioxide balance during a year reached 176, which implies that the growing period might be shorter. Partition of cambium can also be observed for beech at the later stage of growing period; that is, the initial

rapid growth of beech may even stop at the end of July and in August, starting again in September, lasting to early October (*Schmitt et al.*, 2000; *Werf et al.*, 2007). This phenomenon was also observed near Sopron in 2003, when, as the consequence of extremely dry summer, the growth was suppressed in July and August and started again in September lasting till the middle of October when an additional 20% of yearly growth was produced.

Although, it can be generally stated that annual increment is largely determined by weather conditions in the given year and also in the previous two years, months with the strongest impact are probably determined not only by climate parameters, but also the genetic properties of trees beside the seasonality in temperature and precipitation characteristics. While in the neighboring Slovenia precipitation in May-June of the given year has the most important effect on increments of trees (*Čufar et al.*, 2008), and in the Mediterranean region (Albania, Macedonia) the June-September temperature has a negative effect on growth (*Tegel et al.*, 2014), in the Sopron Mountains, where both the yearly precipitation amount and the temperature is lower, the dominant parameter for growth is the precipitation in April and June. In addition, while in Germany the temperature in July in the given year and a year before are dominant for growth (*Gruber*, 2002), in the Sopron region the June temperature in the given year and a year before are determinant.

This overview suggests that further research efforts on beech physiology is needed to give successful explanation on which climatic conditions (monthly or periodic) are the primary drivers of organic matter production through biochemical processes. For this reason, calculation of universal climate index for general use is still not possible, but it can be done in a similar way for stands in different climate and genetic conditions.

As we have already seen above, there were substantial variations in precipitation and temperature conditions among different months during the observed period. On the basis of linear regression analysis, the growth in May and June significantly depends on the average temperature and precipitation. The sign of correlation coefficient shows a positive relation between growth and temperature in spring, but in the following months the relation is negative (*Table 10*). The effect of precipitation is just the opposite; in springtime the precipitation shows negative correlation with growth, while in the following periods the relation is positive.

The breakpoint analysis in the period of 1985–2007 indicates significant shifts in the monthly precipitation and temperature between 1990 and 2000 (*Table 4*). After the breakpoints we found positive and negative shifts for temperature and precipitation, respectively. We suppose that the observed decrease of increments (*Table 7*) is due to the change in meteorological conditions, and taking into account the predicted climate change scenarios these phenomena will proceed in the future. The change in meteorological conditions are reflected not only in the decrease of yearly increment but also in decreasing

share of summer, increasing relative share of spring, and importance of autumn months' conditions in the yearly growth. In addition, growth in May became dominant after the breakpoint instead of June, and the share of July and August drastically decreased in that period (*Fig. 4*). E.g., the increments in July were zero in three years (2002, 2003, and 2007) and were, similarly, zero in four years in August (2000, 2001, 2003, and 2004). This phenomenon is in connection not only with the meteorological conditions of July/August in the given year but also with the climate in preceding months or periods even two year before.

The determining effect of May and June in organic matter production of beech were reported previously as well (*Dittmar et al.*, 2003; *Lebourgeois et al.*, 2005; *Di Filippo et al.*, 2007). According to earlier observations (*Járó* and *Tátraaljai*, 1985), in Hungarian conditions the maximum growth can be observed in June for almost all of tree species. *Knott* (2004) examined a beech stand in an average year of 2001 (elevation: 470 m, DBH: 38 cm, yearly mean air temperature: 7.9 °C, precipitation: 761 mm year^{-1}). The increments for trees have the maximum in summer (increments in July, June, Aug, May are: 30.3%, 27.4%, 21.6%, and 16.0%, respectively). Precipitation in July and August was above the average. This could be the reason of the relatively higher increments in the summer months compared to our test site. This statement is, however, no longer valid for our beech stand, where the maxima of growth shifted to May. It may be an indirect indication of the climate change (*Werf et al.*, 2007; *Ježík et al.*, 2011; *Čufar et al.*, 2012).

Signs of change in relative share of different months and the increasing share of spring in increments were reported earlier similarly to our findings. *Ježík* et al. (2011) investigated beech trees in 2003–2008 with similar climate conditions (elevation: 470 m, DBH: 32–36 cm, yearly mean air temperature: 7.9 °C, precipitation: 715 mm year^{-1}). They found that at the start of the vegetation season, increments positively correlated with temperature. In summer it was hampered by long-term heat waves and the positive influence of precipitation became more pronounced. In view of the predicted climate change, they expected a shift in the culmination of beech seasonal diameter increase towards May caused by warmer springs and a higher frequency of summer droughts and heat waves.

Werf et al. (2007) also pointed out the effect of drought in the year of 2003 to the increment. They measured the increments of beech when summer temperature was 2.1 °C higher and precipitation was 59% lower than the 100-year average (9.5 °C, 760 mm). In summer drought the growth ceased, but it recovered after the drought as it was observed in our test stand after a significant change in summer temperature and precipitation since 2000. The decrease in increment is evident in the dry season, since soil drought stimulates increased stomatal resistance with parallel decrease of photosynthetic activity for European beech (*Priwitzer et al.*, 2014).

5. Conclusions

There were characteristic breakpoints both in meteorological parameters and in beech increments in the Sopron Mountains between 1999 and 2000. The negative shift in precipitation and positive shift in temperature caused a dramatic decrease in growth in summer. There was a shift in maximum monthly increments from June to May, indicating the effect of the climate change on seasonal growth of beech. Significant, dramatic decrease in growth can be observed in July and August that was not observed before. Due to the warmer spring and the arid summer months, the relative share of spring and importance of autumn months increased and expectedly will be increasing in the future. The phenomena of low or zero growth in July and August, observed often after 2000, probably will be more frequent in the future, taking into account the predicted climate change scenarios. The long-term trend of yearly basal area increment is continuously decreasing; the average yearly increments halved between 1985 and 2007.

According to multivariable regression analysis on independent variables derived by CReMIT, the yearly basal area increment is affected not only by meteorological parameters but also the climate of the previous two years. Precipitation generally favors organic matter production in contrast with temperature. Interestingly, one of the dominant periods for basal area increment is the autumn two years before a given year (October-November), when precipitation has positive influence and temperature has negative effect on the increment, i.e., the wet and cool autumn in that year favors organic matter production. Regarding the preceding year, precipitation in the main growing period (spring-early summer) has positive while temperature in autumn has negative effect. Finally, in the current year, precipitation in spring-early summer (especially in April-June) helps the growth of trees, and in contrary, the temperature in that period has negative effect on the increment. There is a negative relationship between the observed basal area increment and the mean temperature in June (July).

The share of basal area increment in the main growing cycle is continuously decreasing which is partly compensated by a parallel increase of it in the final growing period as the climate at the studied region, in the Sopron region, Hungary has become warmer. This phenomenon underlines the general observations made in Hungary. The warming climate has negative effect on the production of trees. According to forecasted climate change, when temperature in early summer in Hungary will be higher and higher, not only the loss in growth but also the drastic decay in vitality and tolerance of trees can be expected.

It seems that the rate of increments is controlled by weather parameters in earlier phenological phases in previous years as well as through the effect of different physiological processes described above (defoliation, bud structure

production, cupules production, etc.), at least for the examined stand. The direct generalization of the observations is hardly possible regarding the high differences in species composition, genetics, climate, pedology, hydrology, etc., among the different regions, as we saw in the discussion through examples for other sites for Hungary as well as for Slovenia and Germany. However, the tools and methods applied in this paper are suitable to study other areas to determine which periods and which weather components have the greatest influence on the yearly increments of trees.

Acknowledgements—This work was supported by the Hungarian Scientific Research Fund (OTKA CK 80305/80335]; by the NAIK KFI (RD011-12) and the "Scientific analysis of Earth-system data and its communication for the society with tolls of recent informatics" (TAMOP-4.2.2.C–11/1/KONV-2012-0015) projects sponsored by the EU and the European Social Fund. Thanks to the "Lendület" program of the Hungarian Academy of Sciences (LP2012-27/2012). Authors thank *dr. Andreas Rigling* for the useful advices to improve the manuscript. Thanks to *Margit Horoszné Gulyás* for the basemap of *Fig. 1*.

Appendix

Brief description of CReMIT

Let be given a time series and its natural period denoted by P. The elements of this time series are stored in vector ts. Let the first element of ts, ts_1 be the chronologically latest element, and natural numbers will be assigned to the data accordingly:

$$ts = \begin{pmatrix} ts_1 \\ ts_2 \\ \vdots \\ ts_m \end{pmatrix}.$$

Let be denoted by SP ($1 \leq SP \leq P$) the starting point of the currently applied investigation, this is the SPth element of the vector ts. Special windows are applied on the vector ts, the time shifting (i) and width (j) values of a window are defined based on this index. The minimal value of time shifting can be 0 (i=0), and the minimal window width can be 1 (j=0). Based on the periodicity P of the basic time series, the above defined window will be periodically repeated with the maximum cycle number (MCN). The value of MCN depending on the defined parameters (SP, i, j) can be created:

$$MCN = \left[\frac{n-(SP+i+j)}{P}\right]+1,$$

where square brackets is for the integer part function.

The starting and end point indices of the windows created with the actual *SP*, *i*, and *j* values can be defined as $[SP + i + l \times P; SP + i + j + l \times P]$, where $0 \leq l \leq MCN$. Two temporal vectors are defined for the storage of the index values determining the limits of the windows using these parameters. Let us denote by:

$$index_{begin} = \begin{pmatrix} SP + i + 0 * P \\ SP + i + 1 * P \\ \vdots \\ SP + i + (MCN - 1) * P \end{pmatrix},$$

$$index_{end} = \begin{pmatrix} SP + i + j + 0 * P \\ SP + i + j + 1 * P \\ \vdots \\ SP + i + j + (MCN - 1) * P \end{pmatrix}.$$

By using the above defined index vectors, a pre-defined transformation function *TR* can be applied on the elements of the individual windows.

$$tr\_x_{SP,i,j} = \begin{pmatrix} TR(index_{begin}[1]; index_{end}[1]) \\ TR(index_{begin}[2]; index_{end}[2]) \\ \cdots \\ TR(index_{begin}[MCN]; index_{end}[MCN]) \end{pmatrix}$$

Based on the starting point ($1 \leq SP \leq P$), the maximum time shifting value *I* ($0 \leq i \leq I$), and the maximum window width *J* ($0 \leq j \leq J$) pre-defined on the basis of the task, all the potential $tr\_x_{SP,i,j}$ transformed vectors can be generated on a systematic way. The above mentioned *MCN* value defines the number of windows for the current parameters (*SP*, *i*, *j*) and the dimension of the transformed vector.

The different phases of the CReMIT are: i) data preparation, ii) creation of the secondary dataset, and iii) analyses of the whole datasets. Considering technical points of view, creation of secondary dataset can be determined by the maximum seasonal shift and length of the investigated period. Hence, by using an appropriate aggregation function (*TR*) (e.g., mean, sum, minimum, maximum) new, complex data sets can be derived consistently from the original data. The CReMIT has been applied for weather parameters in this work. The relevant time intervals to the growth data of the given year were selected using a maximum three years of shift compared to the data of increment, with a maximum of 12 month of an interval length. In this manner, beside the meteorological data for the given year, we involved the mean temperature and precipitation sum data also for the previous two years with a length of 1–12 months (secondary dataset).

References

Bouriaud, O. and *Popa, I.*, 2009: Comparative dendroclimatic study of *Scots pine*, *Norway spruce*, and *Silver fir* in the Vrancea Range, Eastern Carpathian Mountains. *Trees 23*, 95–106.

Bräker, O.U., 1996: Growth trends of Swiss forests, tree-ring data Case study Toppwald, In (Eds.: *Spiecker, H., Mielikäinen, K., Köhl, M., Skovsgaard, J.P.*) Growth trends in European forests. Springer, Berlin, Heidelberg pp. 199–217.

Briffa, K.R., Osborn, J.T., Schweingruber, H.F., Jones, D.P., Shiyatov, G.S., and *Vaganov, A.E.*, 2002: Tree-ring width and density data around the Northern Hemisphere, Part 1, local and regional climate signals. *Holocene 12*, 737–757.

Büntgen, U., Frank, C.D., Schmidhalter, M., Neuwirth, B., Seifert, M., and *Esper, J.*, 2006: Growth/climate response shift in a long subalpine spruce chronology. *Trees 20*, 99–110.

Čufar, K., Prislan, P., de Luis, M., and *Gričar, J.*, 2008: Tree-ring variation, wood formation and phenology of beech (*Fagus sylvatica*) from a representative site in Slovenia, SE Central Europe. *Trees 22*, 749–758.

Čufar, K., de Luis, M., Saz, M.A., Črepinšek, Z., and *Kajfež-Bogataj, K.*, 2012: Temporal shifts in leaf phenology of beech (*Fagus sylvatica*) depend on elevation. *Trees 26*, 1091–1100.

Deslauriers, A., Morin, H., Urbinati, C., and *Carrer, M.*, 2003: Daily weather response of balsam fir (*Abies balsamea* (L.) Mill.) stem radius increment from dendrometer analysis in the boreal forests of Québec (Canada). *Trees 17*, 477–484.

Deslauriers, A., Rossi, S., and *Anfodillo, T.*, 2007a: Dendrometer and intra-annual tree growth: What kind of information can be inferred? *Dendrochronologia 25*, 113–124.

Deslauriers, A., Anfodillo, T., Rossi, S., and *Carraro, V.*, 2007b: Using simple causal modeling to understand how water and temperature affect daily stem radial variation in trees. *Tree Physiol. 27*, 1125–1136.

Di Filippo, A., Biondi, F., Čufar, K., De Luis, M., Grabner M., Maugeri M., Presutti Saba E., Schirone, B., and *Piovesan, G.*, 2007: Bioclimatology of beech (*Fagus sylvatica* L.) in the Eastern Alps: spatial and altitudinal climatic signals identified through a tree-ring network. *J. Biogeo. 34*, 1873–1892.

Dittmar, C., Zech W., and *Elling, W.*, 2003: Growth variations of common beech (*Fagus sylvatica* L.) under different climatic and environmental conditions in Europe – a dendroecological study. *Forest Ecol. Manag. 173*, 63–78.

Ellenberg, H., 1988: Vegetation ecology of Central Europe. 4th ed. Cambridge University Press. Cambridge.

EUFORGEN, 2009: Distribution map of Beech (*Fagus sylvatica*) EUFORGEN 2009, www.euforgen.org. (last accessed: 15 Jan 2015).

Fekedulegn, D., Hicks, R.R., and *Colbert, J.J.*, 2003: Influence of topographic aspect, precipitation and drought on radial growth of four major tree species in an Appalachian watershed. *Forest Ecol. Manag. 177*, 409–425.

Fekete, Z., 1958: Fatermési és faállományszerkezeti vizsgálatok hazai bükkösökben. Mezőgazdasági Kiadó, Budapest, pp. 108.

Führer, E., Mátyás, C., Csóka, G., Lakatos, F., Bordács, S., Nagy, L., and *Rasztovits, E.*, 2010: Current status of European beech (*Fagus sylvatica* L.) genetic resources in Hungary. *Communicationes Instituti Forestalis Bohemicae 25*, 152–163.

Führer, E., Horváth, L., Jagodics, A., Machon, A., and *Szabados, I.*, 2011: Application of a new aridity index in Hungarian forestry practice. *Időjárás 115*, 103–118.

Führer, E., Jagodics, A., Juhász, I., Marosi, G., and *Horváth, L.*, 2013: Ecological and economical impacts of climate change on Hungarian forestry practice. *Időjárás 117*, 159–174.

Gálos, B., Lorenz, P., and *Jacob, D.*, 2007: Will dry events occur more often in Hungary in the future? *Envir. Res. Lett. 2*, 034006.

Garamszegi, B. and *Kern, Z.*, 2014: Climate influence on radial growth of *Fagus sylvatica* growing near the edge of its distribution in Bükk Mts., Hungary. *Dendrobiol. 72*, 93–102.

Geßler, A., Keitel, C., Kreuzwieser, J., Matyssek, R., Seiler, W., and *Rennenberg, H.*, 2007: Potential risks for European beech (*Fagus sylvatica* L.) in a changing climate. *Trees 21*, 1–11.

Gruber, F., 2002: Wachstum von Altbuchen (*Fagus sylvatica* L.) auf einem Kalkstandort (Göttinger/Södderich) in Abhängigkeit von der Witterung III Bohrkenanalysen. *Allgemeine Forst- und Jagdzeitung 173*, 117–122.

Gruber, F., 2004: Die Steuerung des sogenannten „Blattverlust" der Buche (*Fagus sylvatica* L.) durch die Witterung. *Allgemeine Forst- und Jagdzeitung 175*, 83–94.

Gutiérrez, E., Campelo, F., Camarero, J.J., Ribas, M., Muntán, E., Nabais, C., and *Freitas H.*, 2011: Climate controls act at different scales on the seasonal pattern of *Quercus ilex* L. stem radial increments in NE Spain. *Trees 25*, 637–646.

Hasenauer, H., Nemani, R.R., Schadauer, K., and *Running, S.W.*, 1999: Forest growth response to changing climate between 1961 and 1990 in Austria. *Forest Ecol. Manage. 122*, 209–219.

Hidnert, P. and *Krider, H.S.*, 1947: *Thermal expansion of some copper alloys*. U. S. Department of Commerce National Bureau of Standards Research Paper RP1838; J. Res. National Bureau of Standards 39, 419-424.

IUSS, 2014: IUSS Working Group WRB, World Reference Base for Soil Resources 2014. International soil classification system for naming soils and creating legends for soil maps. World Soil Resources Reports No. 106, FAO, Rome.

Járó, Z. and *Tátraaljai, E.*, 1985: A fák éves növekedése. *Erd. Kut. 76–77*, 221–234.

Ježík, M., Blaženec, M., Střelcová, K., and *Ditmarová, Ľ.*, 2011: The impact of the 2003–2008 weather variability on intra-annual stem diameter changes of beech trees at a submontane site in central Slovakia. *Dendrochronologia 29*, 227–235.

Jump A.S., Hunt J., and *Peñuelas J.*, 2006: Rapid climate change-related growth decline at the southern range edge of *Fagus sylvatica*. *Global Change Biol. 12*, 2163–2174.

Jump, A.S., Cavin, L., and *Hunter, P.D.*, 2010: Monitoring and managing responses to climate change at the retreating range edge of forest trees. *J. Environ. Monit. 12*, 1791–1798.

Kahle, H.P., Karjalainen, T., Schuck, A., Ågren, G.I., Kellomäki, S., Mellert, K., Prietzel, J., Rehfuess, K.E., and *Spiecker, H.* (Eds.), 2008: Causes and consequences of forest growth trends in Europe – Results of the Recognition Project. EFI Research Report 21. Brill Academic Publisher, Leiden, Boston, Köln, 262 pp.

Kern, Z. and *Popa, I.*, 2007: Climate-growth relationship of tree species from a mixed stand of Apuseni Mts, Romania. *Dendrochronologia 24*, 109–115.

Knott, R., 2004: Seasonal dynamics of the diameter increment of fir (*Abies alba* Mill.) and beech (*Fagus sylvatica* L.) in a mixed stand. *J. Forest Sci. 50*, 149–160.

Kozlowski, T.T., Kramer, P.J., and *Pallardy, S.G.*, 1991: The physiological ecology of woody plants. Academic Press, San Diego, London.

Lakatos, M., Szentimrey, T., Bihari, Z., and *Szalai, S.*, 2013: Creation of a homogenized climate database for the Carpathian region by applying the MASH procedure and the preliminary analysis of the data. *Időjárás 117*, 143–158.

Larcher, W., 2001: Ökophysiologie der Pflanzen. 6. Aufl. Ulmer, Stuttgart.

Lebourgeois, F., Bréda, N., Ulrich, E., and *Granier, A.*, 2005: Climate – tree-growth relationships of European beech (*Fagus sylvatica* L.) in the French permanent plot network (RENECOFOR). *Trees 19*, 385–401.

Liming, F.G., 1957: Homemade dendrometers. *Forestry 55*, 575–577.

Lin, Y.S., Medlyn, B.E., and *Ellsworth, D.S.*, 2012: Temperature responses of leaf net photosynthesis: the role of component processes. *Tree Physiol. 32*, 219-231.

Maaten, van der, E., 2012: Climate sensitivity of radial growth in European beech (*Fagus sylvatica* L.) at different aspects in southwestern Germany. *Trees 26*, 777–788.

Magri, D., 2008: Patterns of post-glacial spread and the extent of glacial refugia of European beech (*Fagus sylvatica*). *J. Biogeogr. 35*, 450-463.

Mares, C. and *Mares, I.*, 1994: *Climate change-points in the precipitation time series from Romania.* In: Atmospheric Physics and Dynamics in the Analysis and Prognosis of Precipitation Fields (Proceedings of the meeting). Rome, 176–180.

Mátyás, C., 2010: Forecasts needed for retreating forests (Opinion). *Nature 464*, 1271.

Mátyás, C., Nagy, L., and *Ujvári-Jármay, É.*, 2010: Genetically set response of trees to climatic change, with special regard to the xeric (retreating) limits. *Forstarchiv 81*, 130–141.

Maxime, C. and *Hendrik, D.*, 2011: Effects of climate on diameter growth of co-occurring *Fagus sylvatica* and *Abies alba* along an altitudinal gradient. *Trees 25*, 265–276.

Mendlik, G., 1967: A zalai bükkösök fatermési vizsgálata. *Az Erdő 16*, 76–82.

Menzel, L. and *Fabian, P.*, 1999: Growing season extended in Europe. *Nature 397*, 659.

Michelot, A., Bréda, N., Damesin, C., and *Dufrêne, E.*, 2012: Differing growth responses to climatic variations and soil water deficits of *Fagus sylvatica*, *Quercus petraea* and *Pinus sylvestris* in a temperate forest. *Forest Ecol. Manag. 265*, 161–171.

Muzika, R.M., Guyette, R.P., Zielonka, T., and *Liebhold, A.M.*, 2004: The influence of O_3, NO_2 and SO_2 on growth of *Picea abies* and *Fagus sylvatica* in the Carpathian Mountains. *Envir. Poll. 130*, 65–71.

Novák, J., Slodičák, M., Kacálek, D., and *Dušek, D.*, 2010: The effect of different stand density on diameter growth response in Scots pine stands in relation to climate situations. *J. Forest Sci. 56*, 461–473.

Pedersen B.S., 1998: The role of stress in the mortality of Midwestern oaks as indicated by growth prior to death. *Ecology 79*, 79–93.

Peñuelas, J., Hunt, J.M., Ogaya R., and *Jump, A.S.*, 2008: Twentieth century changes of tree-ring $\delta^{13}C$ at the southern range-edge of *Fagus sylvatica*: increasing water-use efficiency does not avoid the growth decline induced by warming at low altitudes. *Global Change Biol. 14*, 1076–1088.

Petráš, R. and *Mecko, J.*, 2011: Effect of climatic factors on the dynamics of radial increments of *Norway spruce*, *European beech* and *sessile oak. J. Forest Sci. 57*, 293–302.

Pettitt A.N., 1979: A non-parametric approach to the change-point problem. *Appl. Statist. 28*, 126-135.

Pichler, P. and *Oberhuber, W.*, 2007: Radial growth response of coniferous forest trees in an inner Alpine environment to heat-wave in 2003. *Forest Ecol. Manag. 242*, 688–699.

Piovesan, G. Biondi, F., Filippo, A.D., Alessandrini, A., and *Magueri M.*, 2008: Drought-driven growth reduction in old beech (*Fagus sylvatica* L.) forests of the central Apennines, Italy. *Global Change Biol.14*, 1265–1281.

Pödör, Z., Edelényi, M., and *Jereb, L.*, 2014: Systematic Analysis of Time Series – CReMIT. *Infocommunicat. J. 6*, 16-22.

Pretzsch, H., 1992: Zunehmende Unstimmigkeit zwischen erwartetem und wirklichem Wachstum unserer Waldbestande. *Forstwiss. Cent. Bl. 111*, 336–382.

Prislan, P., Gričar, J., de Luis, M., Smith, K.T, and *Čufar, K.*, 2013: Phenological variation in xylem and phloem formation in *Fagus sylvatica* from two contrasting sites. *Agr. Forest Meteorol. 180*, 142–151.

Priwitzer, T., Kurjak, D., Kmeť, J., Sitková, Z., and *Leštianska, A.*, 2014: Photosynthetic response of European beech to atmospheric and soil drought. *Lesn. Cas. For. J. 60*, 31–37.

Scharnweber, T., Manthey, M., Criegee, C., Bauwe, A., Schroder, C, and *Wilmking, M.*, 2011: Drought matters – Declining precipitation influences growth of *Fagus sylvatica* L., *Quercus robur* L. in north-eastern Germany. *Forest Ecol. Manag. 262*, 947–961.

Schmitt, U., Möller, R., and *Eckstein, D.*, 2000: Seasonal wood formation dynamics of beech (*Fagus sylvatica* L.) and black locust (*Robinia pseudoacacia* L.) as determined by the "pinning" technique. *Angewandte Botanik 74*, 10–16.

Schulze, E.D., 1970: Der CO_2-Gaswechsel der Buche (*Fagus silvatica* L.) in Abhängigkeit von den Klimafaktoren im Freiland. *Flora 159*, 177–232. (In German)

Schulze, E.D., Fuchs, M.I, and *Fuchs, M.*, 1977: Spatial distribution of photosynthetic capacity and performance in a mountain spruce forest of Northern Germany I Biomass distribution and daily CO_2 uptake in different crown layers. *Oecologia (Berl.) 29*, 43–61.

Sneyers, R., 1992: On the use of statistical analysis for the objective determination of climate change. *Meteorol. Z. 1*, 247–256.

Somogyi, Z., 2008: Recent trends of tree growth in relation to climate change in Hungary. *Acta. Silv. Lign. Hung. 4*, 17–27.

Spiecker, H., Mielkainen, K., Köhl, M., and *Skovsgaard, J.P.* (Eds). 1996: Growth Trends in European Forests: Studies from 12 Countries. European Forest Institute Research Report Nr. 5. Springer-Verlag, Berlin, 372 pp.

Szabados, I., 2006: The effect of the precipitation on the tree ring width. *Carpath. J. Earth. Env. 1*, 39–44.

Szentimrey, T., Bihari, Z., and *Lakatos, M.*, 2010: Quality control procedures in MISH-MASH systems. European Conference on Applied Climatology (ECAC), 13–17 September 2010, Zürich, Switzerland.

Tegel, W., Seim, A., Hakelberg, D., Hoffmann, S., Panev, M., Westphal, T., and *Büntgen, U.*, 2014: A recent growth increase of European beech (*Fagus sylvatica* L.) at its Mediterranean distribution limit contradicts drought stress. *Eu. J. Forest Res. 133*, 61–71.

Werf, van der, G.W, Sass-Klaassen, U.G.W, and *Mohren, G.M.J.*, 2007: The impact of the 2003 summer drought on the intra-annual growth pattern of beech (*Fagus sylvatica* L.) and oak (*Quercus robur* L.) on a dry site in The Netherlands. *Dendrochronologia 25*, 103–112.

Zingg, A., 1996: Diameter and basal area increment in permanent growth and yield plots in Switzerland. In (Eds.: *Spiecker, H., Mielikäinen, K., Köhl, M., Skovsgaard, J.P.*). Growth trends in European forests. Springer, Berlin, Heidelberg, 239–265.

IDŐJÁRÁS

Quarterly Journal of the Hungarian Meteorological Service
Vol. 120, No. 2, April – June, 2016, pp. 163–181

A closure study on aerosol extinction in urban air in Hungary

Ágnes Molnár [1*], **Dénes Párkányi** [2], **Kornélia Imre** [1], **Vera Gácser** [3], and **Edit Czágler** [4]

[1]*MTA-PE Air Chemistry Research Group, Veszprém, P.O.Box 158, H-8201 Hungary*

[2]*Centre for Energy Research, Hungarian Academy of Sciences, Budapest 114, P.O. Box 49, H-1525 Hungary*

[3]*University of Pannonia, Veszprém, P.O.Box 158, H-8201 Hungary*

[4]*Hungarian Meteorological Service, Budapest P.O. Box 39, H-1186 Hungary*

[*]*Corresponding author E-mail: amolnar@almos.uni-pannon.hu*

(Manuscript received in final form November 13, 2015)

Abstract—In this study, we present our results from an investigation into the use of visibility data as a viable tool for the survey of long-term variations in air quality. We found that visibility data in general can be used to estimate atmospheric aerosol extinction coefficients, and that PM_{10} can be successfully estimated from aerosol chemical composition. Our results indicate that PM_{10} concentrations provide a good basis for the reconstruction of aerosol extinction coefficients. It was also shown that both derived (from visibility) and reconstructed aerosol extinction coefficients were in good accordance with each other, mainly in the case of dry aerosols. Ambient values can be determined if an adequate hygroscopic growth rate for aerosol extinction is considered. We also found that a rather precise estimation of extinction coefficient can be reached if a modified version of the widely used IMPROVE formula is applied.

Key-words: visibility, reconstruction of extinction coefficient, PM_{10}, aerosol composition

1. Introduction

Visibility (VIS) is a good, simple indicator of air quality. It is well known that VIS is inversely related to atmospheric extinction. Light extinction is controlled by the scattering and absorption of air molecules and aerosol particles and is proportional to the number concentration of molecules and particles. The number of air molecules is a function of temperature and pressure; however, its variation does not result in a significant change in VIS. Drastic decreases or increases in visibility can be attributed to variations in aerosol concentration and changes in the physical and chemical properties of the particles.

According to the Koschmieder theory (*Koschmieder*, 1924), visibility is determined by

$$VIS = \frac{\ln 0.02}{\sigma_{ext}} = \frac{3.912}{\sigma_{ext}}. \quad (1)$$

In the formula, the constant of 3.912 represents the 2% contrast threshold of daylight visual detection of objects against the sky horizon, and σ_{ext} is the total extinction of solar radiation at 550 nm wavelength.

The scattering and absorption efficiencies of particles are functions of aerosol chemical composition and particle size. Sulfates, nitrates, and organics generally contribute to scattering, while elemental and organic carbon compounds are mainly responsible for absorption (e.g., *Malm et al.,* 1994; *Tao et al.,* 2012). Particles participate most in light extinction when their size is in the optically active size range (0.1–1.0 μm). On the other hand, the water vapor content of air (specifically relative humidity) has a significant influence on ambient light extinction as a consequence of water soluble and hygroscopic compounds in the aerosol. According to previous studies, hygroscopic growth can cause the scattering coefficient of dry particles to be doubled or greater as a result of increases in relative humidity (e.g., *Horvath,* 1992; *Seinfeld* and *Pandis,* 1998). Consequently, variations in aerosol concentration (through their size and chemical composition) control changes in dry extinction/visibility; however, in ambient air, water content can also play a major role in light attenuation and visibility impairment (e.g., *Jung et al.,* 2009; *Cheng et al.*, 2011).

High concentrations of air pollutants are a prevalent cause of air quality impairment in both cities and remote areas. Visibility can vary within a wide range, from a few meters to a few hundred kilometers (*Horvath,* 1995; *Singh* and *Dey*, 2012), and can easily become a critically important parameter in the everyday functioning of cities, because low visibility can obstruct surface and aerial traffic, and thereby, unfavorably impact businesses, public safety, and even tourism.

Despite the significant influence of water vapor, visibility (extinction) data provide an efficient and inexpensive tool for the study of long-term variations in air quality and may be utilized as a proxy for the concentration of aerosols and trace gases (*Singh* and *Dey*, 2012). For several decades, an empirical formula for calculating the light extinction coefficient as a function of chemical species in the $PM_{2.5}$ particulate matter has been used by the Interagency Monitoring of Protected Visual Environments (IMPROVE) network (*Hand et al.*, 2011; *Malm et al*, 2013). The IMPROVE program is a cooperative measurement effort among the U.S. Environmental Protection Agency (EPA), federal land management agencies, and state agencies (*Hand et al.*, 2011). The IMPROVE network has collected air quality data since 1988. The main goals of this program are to monitor real-time visibility and aerosol conditions in 156 mandatory Class I areas throughout the United States to identify aerosol species and their emission sources that are responsible for anthropogenic visibility impairment and to study and document long-term trends in air quality and visibility.

The empirical formula used by the IMPROVE network is based on the relationship between light extinction and aerosol chemical composition. The light extinction coefficients of an external mixture of aerosols can be estimated by assuming a linear combination of mass concentrations (M_j) and the corresponding extinction efficiencies (α_j) of different aerosol species (*Hand et al.*, 2011):

$$\sigma_{ext} = \sum \alpha_j \cdot M_j. \tag{2}$$

To account for the hygroscopic effect, extinction efficiencies are multiplied by a humidification factor that is computed by assuming a size distribution and a composition-dependent hygroscopic growth factor. The IMPROVE formula (see later Eq. (7)) is used to reconstruct σ_{ext} (corresponding to 550 nm wavelength) based on measurements of aerosol composition (ammonium sulfate, ammonium nitrate, particulate organic matter, light absorbing carbon, soil, and coarse mass) and a Rayleigh scattering term (*Hand* and *Malm*, 2007). The units of aerosol extinction coefficient and Rayleigh scattering are Mm^{-1}, mass concentrations are given in $\mu g\ m^{-3}$, and mass extinction (scattering and absorption) efficiencies have units of $m^2\ g^{-1}$.

The empirical IMPROVE formula has been applied extensively for different environments, from regional background to urban areas. An important issue is whether this algorithm, which is designed for background air, can be applied in cities. *Cabada et al.* (2004) found that by applying this formula during the Pittsburgh Air Quality Study, the scattering coefficient could be reproduced based on bulk $PM_{2.5}$ composition with relative success. Furthermore, in a number of studies, the extinction coefficient or visibility of megacities in China was reconstructed based on this formula. *Cao et al.* (2012) found that in

Xi'an, China, the model underestimated the measured extinction coefficient and that ammonium sulfate was the largest contributor. *Cheng et al.* (2011) in Jinan, *Pan et al.,* (2009) at a rural site near Beijing and *Tao et al.* (2012) in the Guangzhou urban area all concluded that the IMPROVE formula can provide realistic estimates of the real atmospheric extinction in cases where the relative humidity (RH) was less than 70% (*Tao et al.,* 2012). Under high RH, due to the hygroscopicity of the particles, the absorbed water plays a much greater role in limiting visibility. The study by *Singh* and *Day* (2012), conducted in the megacity of Delhi, India, resulted in similar conclusions. They found that below 80% RH, aerosols contribute ~90% to the observed visibility degradation, but that above 80% RH, the aerosol relative contribution decreases rapidly due to the strong impact of hygroscopicity. Visibility is most sensitive to water-soluble particles and soot in all seasons.

In this work, we studied and discussed the following issues:

a. How the extinction coefficient derived from visibility data can be estimated using the PM_{10} mass and chemical composition;

b. How PM_{10} can be reconstructed from the chemical composition of PM_{10};

c. How PM_{10} can be modelled from visibility observations. This information can result in a retrospective estimation of PM_{10} for periods when PM_{10} data are not available;

d. How the derived extinction coefficient (from VIS) corresponds to the reconstructed data;

e. Similar to other studies, we applied the IMPROVE formula in Budapest. We aimed to clarify how it can be applied in a Central European city and how the parameters in the formula should be changed to better reproduce the measured extinction coefficient;

f. How the hygroscopic effect should be considered to obtain a viable ambient extinction coefficient.

2. Experimental

2.1. Sampling

In this study, data from two sampling campaigns representing winter (February 2 – March 2, 2009) and summer (July 20 – August 20, 2009), aerosols are presented. In both cases, the sampling was conducted at the Marczell György Observatory of the Hungarian Meteorological Service. This site is located in the south-eastern part of Budapest, Hungary. Here, at a standard synoptic weather station, meteorological parameters, including visibility, temperature, and dew point temperature, are measured on an hourly basis. Visibility is also determined

by visual observation. In the observatory, there is also an urban background air pollution monitoring site operated by the Hungarian Air Quality Network (www.levegominoseg.hu), which provides PM_{10} mass concentration. PM_{10} is monitored using the β-gauge method (*Chueinta* and *Hopke*, 2001).

In addition to these routine measurements, aerosol samples were collected daily to determine their chemical composition. A two-stage multi-jet impactor was applied at a sampling rate of 20 $Lmin^{-1}$. The PM_1 fraction was collected on quartz filters, and PM_{1-10} was sampled on Al-foils. From these samples, the inorganic ion (sulfate, nitrate, chloride, ammonium, sodium, potassium, and magnesium) and total carbon contents were measured. Inorganic ion content was determined by ion chromatography (Dionex, 2120) with a detection limit below 10 ppb. The total carbon concentrations of the aerosol samples were measured using an Astro Model 2100 TOC analyzer. This method is based on NDIR absorption. The detection limit of these measurements was 2 μg C.

In the winter campaign, the scattering coefficient of aerosol at 550 nm was also monitored using an M903 integrating nephelometer calibrated with carbon dioxide. These data were used to reconstruct the scattering coefficient (see in Section 3.3). Unfortunately, in the summer campaign, this measurement was not available due to instrument failure. In both campaigns, the daily average absorption coefficients of the aerosol samples were determined indirectly. We supposed that the majority of absorbing components (soot) can be found in the PM_1 aerosol. Using the PM_1 quartz filters, the absorbance of the samples was determined (Eq. (3)). The light transmittance of blank and exposed filters was measured by PSAP (particle soot absorption photometer) at 550 nm. Their ratio gave transmittance (T), and absorbance (A) was derived by

$$A = \log\left(\frac{1}{T}\right). \tag{3}$$

Considering the air volume (V) and surface (S) of the filter, the average absorption coefficient was estimated:

$$\sigma_a = \frac{A \times S}{V}. \tag{4}$$

This method was checked with parallel measurements. During the summer campaign, a PSAP was operated to directly monitor the absorption coefficient. Using the same PSAP, the absorption coefficient was measured both directly and indirectly. From the direct measurements, the daily average absorption coefficients are calculated and compared to the absorption coefficients resulted from the indirect method. The results of this comparison are shown in *Fig. 1*. One can conclude that the absorption coefficients determined in both ways are

linearly related, as the average difference between them was 2.16 ± 2.39 Mm^{-1}. This means that the absorption coefficient was slightly overestimated (less than 10%) when it was calculated using the transmittance of the aerosol filter.

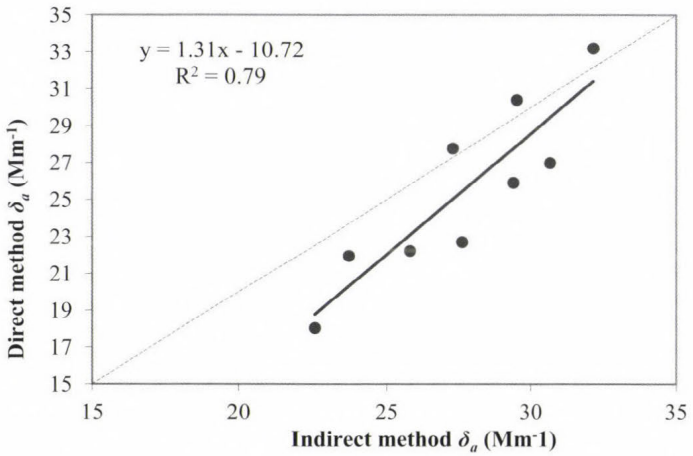

Fig. 1. Comparison of directly and indirectly measured absorption coefficients.

Finally, the organic and elemental (light absorbing) carbon contents of the samples were differentiated. We assumed that the total carbon content of the aerosol would be composed of organic and elemental fractions and that the inorganic carbon would be negligible (see in detail in Section 3.1). The elemental fraction was estimated from the absorption coefficient, considering a mass absorption coefficient of 10 m^{2}g^{-1}. Additionally, organic carbon was calculated as the difference between the total carbon (TC) and elemental carbon concentrations.

2.2. Extinction coefficient and the effect of hygroscopicity

Visibility (VIS) is generally determined by the light extinction of aerosol particles and air molecules. The extinction coefficient (σ_{ext}) can be estimated by means of Koschmieder theory (see Eq. (1)) which refers to 550 nm wavelength.

As previously mentioned, due to the hygroscopicity of the particles, relative humidity also plays an important role in determining visibility. The hygroscopic effect was excluded from the data sets by using the γ-approach as described by, e.g., *Zhou et al.* (2001):

$$\sigma_e = 10^c \times \left(1 - \frac{RH(\%)}{100}\right)^{-\gamma}, \tag{5}$$

$$f(RH) = \sigma_{RH}/\sigma_{40\%}. \tag{6}$$

We found that hygroscopic growth of the extinction coefficient (Eq. (6)) derived from VIS data was substantially different in winter and summer, as shown in *Table 1*. In winter, the aerosol was found to be much more hygroscopic than in summer, and the increase in the particle growth rate with rising RH was considerably greater than that in summer (e.g., at 80% RH, the growth rate was twice as much in winter than summer). As a result, considering the same PM_{10} concentrations, this difference yields a doubled extinction coefficient in winter compared with the summer values.

Table 1. Hygroscopic growth rate of extinction coefficients as a function of relative humidity

Relative humidity (%)	Winter	Summer	Winter/Summer
40	1.0	1.0	1.0
50	1.2	1.1	1.1
60	1.6	1.2	1.2
70	2.2	1.4	1.5
80	3.4	1.7	2.0
90	7.3	2.3	3.1

3. Results and discussion

3.1. Chemical composition and reconstruction of PM_{10}

The PM_{10} mass concentration was more variable during the winter campaign. In winter and summer, the average PM_{10} concentrations were 32 μgm^{-3} and 23 μgm^{-3}, respectively, with maximum concentrations of 107 μgm^{-3} and 54 μgm^{-3}. These average concentrations do not differ significantly from those obtained in three Austrian cities (*Gomišček et al.,* 2004), and Bologna, Italy (*Matta et al.,* 2003). In Vienna, Linz, Graz, and Bologna, the winter and summer PM_{10} concentrations varied in the ranges of 27–39 μgm^{-3} and 17–26 μgm^{-3}, respectively (*Gomišček et al.,* 2004; *Matta et al.,* 2003). In Lens, France (*Waked et al.,* 2014), the overall PM_{10} concentrations were lower, and in winter and summer, the values were 20 μgm^{-3} and 14 μgm^{-3}, respectively. Chemical analysis showed that in Budapest, carbonaceous compounds dominated the PM_{10} compositions, and the mass fractions of organic compounds in winter and summer were 35% and 27%, respectively. In Bologna and Lens, the mass fraction of organic carbon in PM_{10} was rather similar to that of Budapest (Bologna: winter 35% and summer 37% (*Matta et al.,* 2003); Lens: winter 34% and summer 27% (*Waked et al.,* 2014)). In contrast, in Budapest, elemental carbon represented 13% and 14% of PM_{10}, which was generally higher than the EC/BC data published for the other urban background sites around Europe. In

Barcelona, London North Kensington, Lugano (*Reche et al.,* 2011), Bologna (*Matta et al.,* 2003), and Lens (*Waked et al.,* 2014), the mass fractions of EC/BC in PM_{10} were in the range of 4%–10%.

In Budapest, the inorganic compounds were 16% (winter) and 18% (summer) of the total PM_{10} mass. These results are in accordance with earlier results obtained for PM_{10} in Budapest (*Maenhaut et al.,* 2005), but they are significantly lower than those found in other cities. It was found that in winter and summer in Bologna, inorganic species were 53% and 41% of PM_{10} (*Matta et al.,* 2003), while in Lens their contributions were 52% and 42% (*Waked et al.,* 2014).

During both campaigns in Budapest, all components analyzed from the filters were found dominantly in PM_1 as shown in *Table 2*. Among inorganic ions, nitrate was dominant in winter, whereas in summer, sulfate was found in highest concentrations, which is similar to results obtained in other cities. In Bologna, nitrate concentrations were almost 3 times higher than those of sulfate (*Matta et al.,* 2003), whereas in Lens, nitrate was twice as high as sulfate (*Waked et al.,* 2014). The lower nitrate concentrations in summer are the result of the temperature dependency of ammonium nitrate volatility, which was also indicated by lower nitrate fractions among the fine mode compared with the values obtained in winter. Yearly increases in sulfate concentrations during summer months are already known (e.g., *Hidy et al.,* 1978). Higher photochemical activities in summer result in higher rates of SO_2 conversion, which yield summertime maximums in sulfate concentrations. *Table 2* shows that the contributions of fine sulfate, ammonium, and total carbon to PM_{10} were significantly higher during summer than in winter. In contrast, the other components were less accumulated in PM_1 in summer than winter. Specifically, the fraction of fine nitrate concentration decreased from 80% (winter) to 70% (summer).

Table 2. PM_{10} aerosol composition and PM_1 mass fractions (%). The standard deviation is given in parentheses.

	Winter		Summer	
	Concentration (μgm^{-3})	**Fraction in PM_1 (%)**	**Concentration (μgm^{-3})**	**Fraction in PM_1 (%)**
chloride	2.4 (4.4)	85 (15)	1.1 (1.2)	77 (17)
nitrate	7.1 (3.6)	80 (12)	2.2 (0.9)	70 (8)
sulfate	4.2 (2.8)	80 (12)	6.2 (2.7)	93 (4)
sodium	2.0 (0.9)	95 (7)	1.4 (1.3)	65 (30)
ammonium	1.6 (1.6)	82 (17)	0.9 (0.5)	94 (13)
potassium	0.6 (0.3)	96 (5)	0.7 (0.5)	77 (18)
magnesium	0.1 (0.1)	85 (14)	0.2 (0.1)	71 (10)
calcium	1.3 (0.6)	81 (14)	1.7 (0.9)	69 (13)
total carbon	12.5 (6.6)	81 (4)	6.5 (1.2)	88 (7)

The total carbon concentration was twice as much in winter than in summer, and in both seasons more than 80% of the total carbon (TC) concentration was found in PM_1 (see *Table 1*). It is supposed that fine TC is composed primarily of organic and elemental carbon, and that the contribution of inorganic carbon (carbonate) can thus be neglected (e.g., *Karanasiou et al.,* 2011). Carbonate may be present in the coarse fraction; however, its presence has not been ubiquitously confirmed. According to a European survey (*Sillanpää et al.,* 2005), among six cities (Duisburg, Prague, Amsterdam, Helsinki, Barcelona, and Athens), carbonate was detected in the coarse mode in only the two Mediterranean cities. It should be mentioned that in Barcelona and Athens, the coarse fraction of the aerosol was greater than fine, whereas in Duisburg, Prague, and Amsterdam, similarly to Budapest, the fine mode dominated. Other results obtained for Chinese cities also showed the inorganic carbon (carbonate) content of the aerosol to be rather low (*Wang et al.,* 2010). Considering these results, we neglected the contribution of inorganic carbon in both the fine and coarse size ranges. Upon further evaluation, we supposed that the total carbon of PM_{10} was composed of organic and elemental (light absorbing) carbon and that this latter could be exclusively found in the fine fraction (PM_1).

The aerosol chemical composition was reconstructed on the basis of PM_{10}, and the inorganic and carbonaceous compounds were all considered. The chemical mass closure of the inorganic constituents was based on stoichiometry. In addition, based on the recommendations of *Stelson* and *Seinfeld* (1981), other alkaline (potassium) and alkaline earth metallic (calcium and magnesium) ions were included in the reconstruction of the PM_{10} mass. Excess nitrate was assumed to be organic nitrate (e.g., *Fry et al.,* 2014), and the organic and elemental carbon mass concentrations were estimated using conversion factors of 1.4 and 1, respectively. The average chemical composition of the reconstructed aerosol is shown in *Fig. 2*. It should be mentioned that in summer, the inorganic fraction of the aerosol was composed mainly of sulfate containing compounds. In contrast, during the winter season, nitrate compounds dominated the inorganic aerosol fraction, and sulfates (generally in the form of ammonium sulfate) gave a smaller contribution.

Finally, the reconstructed and the directly measured PM_{10} (by the β-gauge monitor described in Section 2.1) mass concentrations were compared. *Fig. 3* shows that these mass concentrations agreed relatively well in both sampling campaigns. In winter, PM_{10} is overestimated by 3.2 μgm^{-3}, whereas in summer, the directly measured PM_{10} is slightly lower than the reconstructed value.

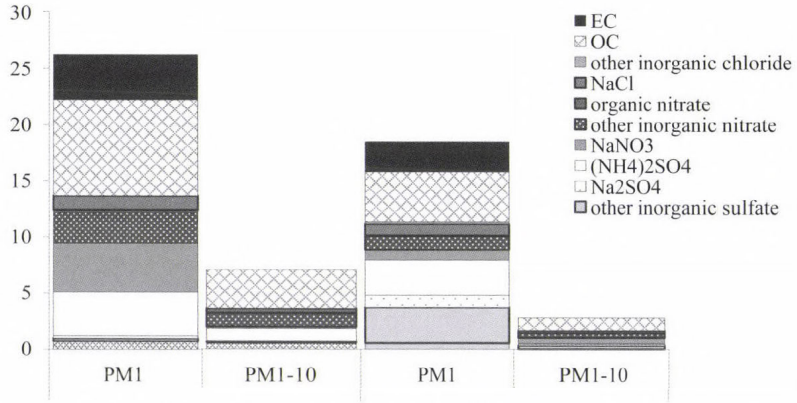

Fig. 2. Chemical mass closure of PM_1 and PM_{1-10} in Budapest.

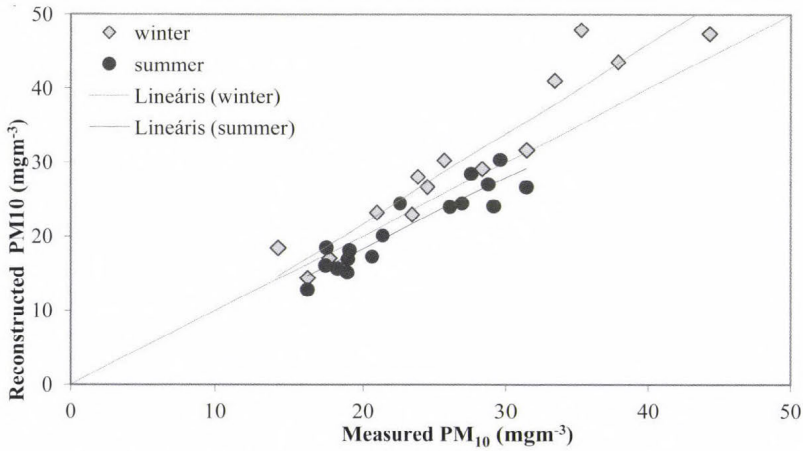

Fig. 3. Reconstructed vs. measured PM_{10} concentration.

3.2. Visibility and extinction coefficient (VIS, $\sigma_{e,VIS}$)

Temporal variations in PM_{10}, visibility, and RH are presented in *Figs. 4a* (winter) and *4b* (summer). The relationship among the parameters is clear. Low visibility coincides with high PM_{10} concentrations and/or high RH; conversely, high visibility occurs when PM_{10} and RH are low. As an example, in *Fig. 4a*, one can follow the development of a winter air pollution episode beginning on February 18 and finishing on February 25. Parallel to a general increase in PM_{10} (occasionally exceeding 100 μgm^{-3}), visibility decreased (average VIS = 7 km),

which was disrupted by a change in RH. In summer, aerosol aging processes also influence variations in visibility. *Bäumer et al.* (2008) demonstrated that when the prevailing air mass undergoes an aging process, and as a result, a significant decrease in VIS is observed, an increase in PM_{10} can be detected.

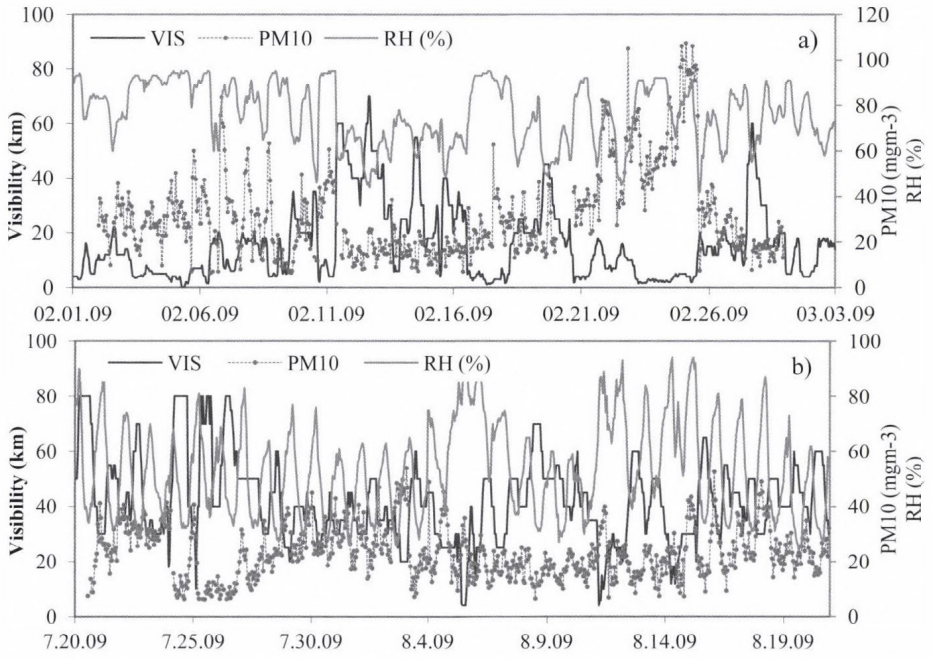

Fig. 4. Temporal variation in VIS, PM_{10} and RH during winter (a) and summer (b) campaigns.

In *Figs. 5a* and *5b*, temporal variations in the ambient and dry extinction coefficients are presented. The ambient extinction coefficients were derived from VIS (Eq. (1)), whereas the dry extinction data referring to 40% RH was obtained by means of the γ-approach (see Eqs. (5) and (6) in Section 2.2). In winter and summer, the average ambient extinction coefficients were 550 Mm^{-1} and 103 Mm^{-1}, and the dry average values were 126 Mm^{-1} and 87 Mm^{-1}, respectively. The difference between the ambient and dry extinction coefficients is attributed to the hygroscopic behavior of the aerosol. The effect of hygroscopicity on the aerosol extinction was particularly important in winter (see *Fig. 5a* and *Table 1*). The significant variation in hygroscopic growth rate is assumed to be the result of seasonal changes in PM_{10} chemical composition.

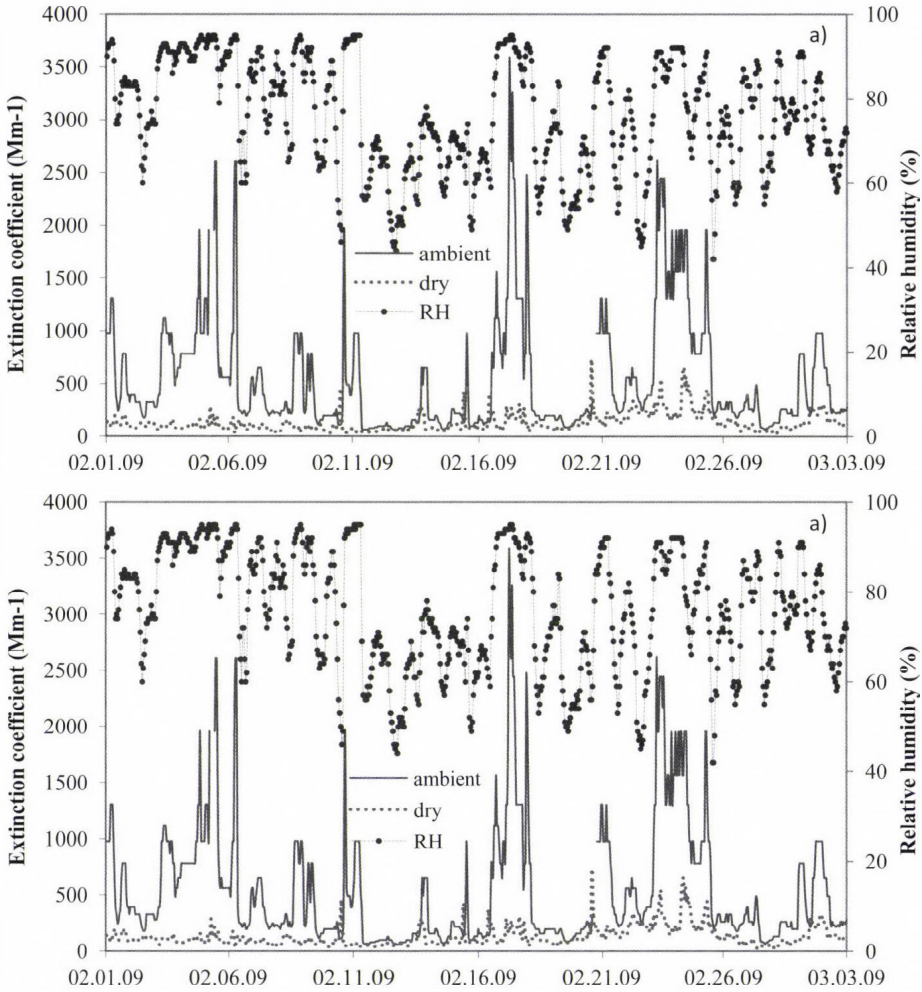

Fig. 5. Temporal variation in the ambient and dry extinction coefficients during winter (a) and summer (b) campaigns in 2009.

The relationship between PM_{10} and dry extinction coefficient is presented in *Fig. 6*. In both seasons, dry extinction coefficient varied similarly as a function of PM_{10}. Based on a linear regression analysis of the combined data sets, the dry mass extinction efficiency was 2.2 m^2g^{-1}, with a correlation coefficient of 0.52. This value is in accordance with the mass extinction efficiencies found in typical continental air. According to *Nemuc et al.* (2013), the mass extinction efficiencies of PM_{10} are typically in the range of 2.2 and 2.7 m^2g^{-1}, which was further confirmed by the value of 2.6 m^2g^{-1} that was obtained at the Hyytiälä Forestry Field Station in central Finland (*Virkkula et al.,* 2011).

Moreover, in urban air, the mass extinction coefficients of PM_{10} do not differ significantly from those obtained for background air. For reference, *Kim* (2015) and *Jung et al.* (2009) reported mass extinction efficiencies of 2.7 m^2g^{-1} and 2.5 m^2g^{-1} for Seoul, Korea, and Beijing, China, respectively.

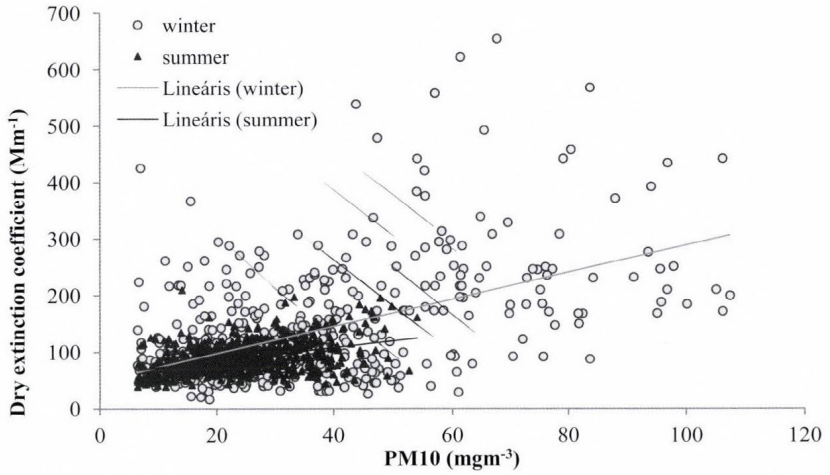

Fig. 6. PM_{10} vs. dry extinction coefficient during the winter and summer campaigns. The relationship between the parameters is statistically significant (at p=99.9%).

3.3. Reconstruction of extinction coefficient

The reconstruction of extinction coefficients is based on the well-known relationship between light extinction and aerosol composition. Sulfate, nitrate, and organic constituents have greater importance in scattering, whereas elemental carbon is more responsible for light absorption. Based on the concentration of different compounds and their mass extinction efficiencies, the extinction coefficient can be estimated (see Eq. (2)) (*Ouimette* and *Flagan*, 1982; *Mészáros*, 1999, *Seinfeld* and *Pandis*, 1998). This method has been well applied for a long time by the IMPROVE program (*DeBell et al.,* 2006) using the following equation:

$$\sigma_e \approx 3\times f\times\left[(NH_4)_2SO_4\right]+3\times f\times\left[NaNO_3\right]+4\times\left[OC\right]+10\times\left[EC\right]+1\times\left[groundbased\right]+0.6\times\left[coarse\right]+10\times(Rayleigh). \quad (7)$$

To reconstruct the ambient extinction coefficient, the dry extinction coefficient was first estimated. In the estimation, we used aerosol chemical composition and optical data, which were independently monitored from visibility. In winter, aerosol scattering and absorption coefficients were measured along with visibility by integrating a nephelometer and PSAP (see

details in Section 2.1). The dry aerosol scattering coefficient was measured by the nephelometer and calculated using the gamma approach (Eq. (5)) that is used when estimating visibility. To estimate dry aerosol scattering, the main aerosol components including ammonium sulfate, ammonium, sodium, and other nitrates as well as organic compounds were taken into account. Multiple regression analysis was applied to determine mass scattering efficiencies. In addition to scattering, aerosol absorption was considered, and EC was calculated from the absorption coefficients of the aerosol daily samples (see details in Section 2.1.). Finally, Rayleigh scattering, which is a function of air temperature and pressure, was determined. We found that the reconstructed dry extinction coefficient can be calculated with the following equation:

$$\sigma_{dry} \approx 2.3 \times \left[(NH_4)_2SO_4\right] + 1.7 \times \left[NaNO_3 + KNO_3 + Ca(NO_3)_2 + Mg(NO_3)_2\right] + 1.5 \times \left[OC\right] + 10 \times \left[EC\right] + 12\left(Rayleigh\right). \quad (8)$$

When comparing the mass scattering/absorption efficiencies used in the IMPROVE network to our results, some similarities and differences were noticed. Our equation refers to PM_{10}, whereas in the IMPROVE network, $PM_{2.5}$ and coarse particles are considered separately. The mass scattering efficiencies of ammonium sulfate and nitrate salts were rather similar (≈ 2 m^2g^{-1}) to those identified by the IMPROVE network (3 m^2g^{-1}), although our obtained value was 30% smaller. In contrast to the inorganic species, the difference in mass scattering efficiencies for the organics is quite high (this study: 1.5 m^2g^{-1}; IMPROVE: 4 m^2g^{-1}). One possible explanation for the smaller values could be the difference between PM_{10} and $PM_{2.5}$, not differentiated in this study.

In addition, for the sake of simplicity, we modeled the dry extinction coefficient on the basis of only sulfate and nitrate ion as well as, organic and elemental carbon concentrations. In this case, the reconstruction equation was

$$\sigma_{dry,anions} = 4.3 \times \left[SO_4^{2-}\right] + 1.3 \times \left[NO_3^-\right] + 1.5 \times \left[OC\right] + 10 \times \left[EC\right] + 12\left(Rayleigh\right). \quad (9)$$

Comparing our models (Eqs. (8) and (9)) to the IMPROVE model (Eq. (7)), we concluded that all three models gave similar results for the reconstruction of the dry extinction coefficient. In *Table 3* the relationships between reconstructed and "observed" (calculated from visibility) extinction coefficients are shown. These relationships are characterized by linear regression equations and correlation coefficients. On the basis of these parameters, one can conclude that dry extinction data can be almost equally reconstructed by all three models. In other words the IMPROVE model – which is constructed for background aerosol – also provides sufficiently good estimation of dry extinction coefficient even in urban air, in Budapest. This is in agreement with other studies which

indicated similar conclusions in megacities of Beijing and Delhi: in relatively dry atmosphere, this model provided realistic estimation of the ambient extinction coefficient (*Tao et al.*, 2012; *Sing* and *Day*, 2012). It has to note, that our models (mainly Eq. (9)) require less input data than the IMPROVE model; and for this reason they can be more easily applied for the available data sets.

Table 3. Relationship between reconstructed (three models) and "observed" extinction coefficients

	Linear regression equation	**Correlation coefficient**
Dry aerosol		
Eq. (8)	y = 0.65x+10.4	0.577
Eq. (9)	y = 0.64x+20.5	0.619
IMPROVE	y = 0.76x+11.0	0.562
Ambient aerosol		
Eq. (8)	y = 0.96x-27.9	0.926
Eq. (9)	y = 0.97x-16.7	0.935
IMPROVE	y = 0.24x+53.7	0.779

Note: x and y are the extinction coefficient from VIS and the reconstructed (by models) extinction coefficients, respectively.

To reconstruct the ambient extinction coefficient, the hygroscopic growth of the extinction coefficient obtained from visibility data was calculated as:

$$\sigma_{ambient} = f \cdot \sigma_{dry}. \tag{10}$$

Then, the inorganic (sulfate and nitrate salts (Eq.8) or ions (Eq.9)) and organic (OC) parts in our models were multiplied by these growth factors (*f*). The adequacy of the models for the reconstruction of ambient extinction coefficients is shown in *Table 3*. In each season, the adequate hygroscopic growth rates were considered. We can conclude that both approaches are suitable for the reconstruction of the extinction coefficient; however, they slightly underestimate the ambient extinction coefficient when compared to visibility data.

Figs. 7a and *7b* show the agreement of ambient extinction in more detail. We can conclude that the temporal variation in the ambient extinction coefficient is well represented by both models, but the actual extent of σ is generally underestimated by the model equations.

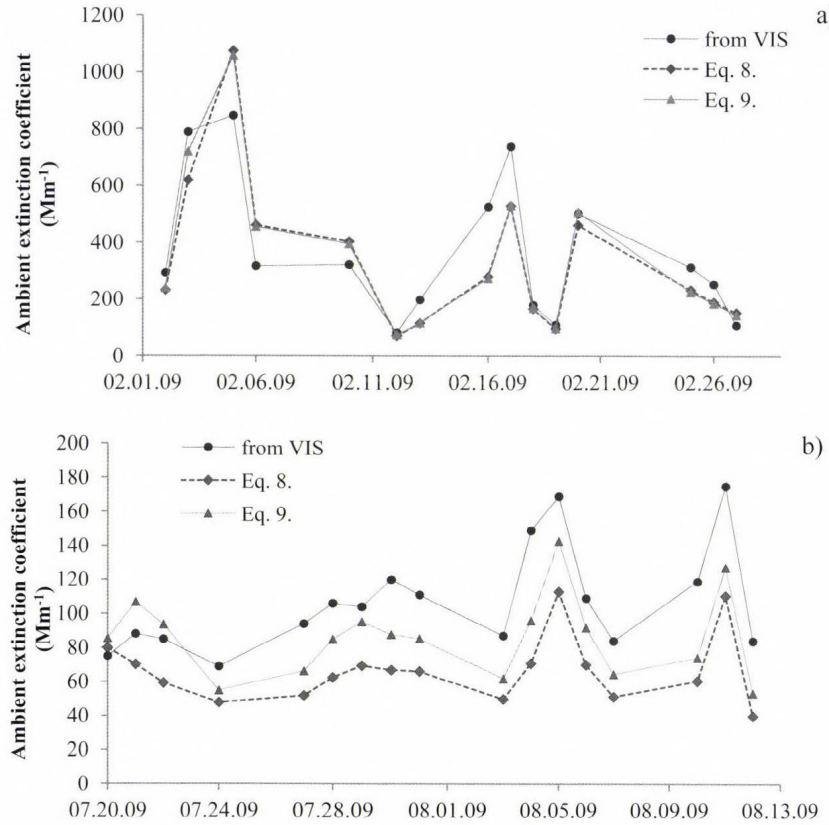

Fig. 7. Temporal variation in the ambient extinction coefficients.

Finally, we compared the three model results obtained for ambient air. We found that the results substantially differ if IMPROVE or our models are applied (see *Table 3*). The main reason for the discrepancy between modeled dry and ambient extinction coefficients can arise from the different consideration of aerosol hygroscopicity. In the case of IMPROVE, model hygroscopic growth is supposed only for ammonium sulfate and sodium nitrate content, while in our models the hygroscopicity of organic species is also involved. It supported by the well-known fact that an important part of organic compounds is hydrophilic, even water soluble. As a result, our models provide more realistic estimation of the ambient extinction coefficient compared to the IMPROVE model. This draws the attention to the significance of aerosol hygrosopicity, concerning both the inorganic and organic contents of the particles. The application of proper hygroscopic growth rate (which is a function of the chemical composition; and has significant seasonality) plays very important role in the reconstruction of ambient extinction coefficient.

4. Conclusions

Based on our results, we can conclude that visibility (extinction) data provide an efficient and inexpensive tool for the survey of long-term variations in air quality and may be utilized as a proxy for PM_{10} concentration. We have found that visibility data can generally be used to estimate atmospheric aerosol extinction coefficients, even in a retrospective manner. The closure experiment has shown that PM_{10} can be successfully estimated by chemical composition and that the PM_{10} concentration can be estimated from visibility/extinction coefficient data (using the Koschmieder theory). Our results indicate that the PM_{10} concentration (measured or modeled from the chemical composition) provides a good basis for the reconstruction of aerosol extinction coefficients. It is also shown that the derived (from VIS) and reconstructed (from PM_{10} or the aerosol chemical composition) aerosol extinction coefficients are in good accordance with each other, mainly in the case of dry aerosols. Ambient values can be estimated if the adequate hygroscopic growth rate for the aerosol extinction is considered. We have also found that a rather precise estimation of extinction coefficient can be reached if a modified version of the widely used IMPROVE formula is applied.

Acknowledgements: Authors are grateful for the support of Hungarian Scientific Research Fund (OTKA), project number K 113059.

References

Bäumer, D., Vogel, B., Versick, S., Rinke, R., Möhler, O., and *Schnaiter, M.,* 2008: Relationship of visibility, aerosol optical thickness and aerosol size distribution in an ageing air mass over South-West Germany. *Atmos. Environ. 42,* 989–998.

Cabada, J.C., Khlystov, A., Wittig, A.E., Pilinis, C. and *Pandis, S.N.,* 2004: Light scattering by fine particles during the Pittsburgh Air Quality Study: Measurements and modeling. *J. Geophys. Res. 109,* D16S03.

Cao, J.-J. Wang, Q.-Y, Chow, J.C., Watson, J.G., Tie, X.-X., Shen, Z.-X., Wang, P., and *An, Z.-S.,* 2012: Impacts of aerosol compositions on visibility impairment in Xi'an, China. *Atmos. Environ. 59,* 559–566.

Cheng, S.-H., Yang, L.-X., Zhou, X.-H., Xue, L.-K., Gao, X.-M., Zhou, Y. and Wang, W.-X., 2011: Size-fractionated water-soluble ions, situ pH and water content in aerosol on hazy days and the influences on visibility impairment in Jinan, China. *Atmos. Environ. 45,* 4631–4640

Chueinta, W. and *Hopke, P. K.*, 2001: Beta gauge for aerosol mass measurement. *Aerosol Sci. Technol. 35,* 840–843.

DeBell, L.J., Gebhart, K.A., Hand, J.L., Malm, W.C., Pitchford, M.L., Schichtel, B.A, and *White, W.H.,* 2006: IMPROVE (Interagency Monitoring of Protected Visual Environments): Spatial and Seasonal Patterns and Temporal Variability of Haze and its Constituents in the United States. Report IV CIRA Report ISSN: 0737-5352-74, Colorado State Univ., Fort Collins.

Fry, J.L., Draper, D.C., Barsanti, K.C., Smith, J.N., Ortega, J., Winkler, P.M., Lawler, M.J., Brown, S.S., Edwards, P.M., Cohen, R.C., and *Lee, L.,* 2014: Secondary organic aerosol formation and organic nitrate yield from NO_3 oxidation of biogenic hydrocarbons. *Environ. Sci. Technol. 48,* 11944–11953.

Gomišček, B., Hauck, H., Stopper, S., and *Preining, O.,* 2004: Spatial and temporal variations of PM1, PM2.5, PM10 and particle number concentration during the AUPHEP—project. *Atmos. Environ. 38,* 3917–3934

Hand, J. L., Malm, W. C., 2007: Review of aerosol mass scattering efficiencies from groundbased measurements since 1990, *J. Geophys. Res.-Atmospheres, 112,* (D18).

Hand, J.L., Copeland, S.A., Day, D.E., Dillner, A. M., Indresand, H., Malm, W.C., McDade, C.E., Moore, C.T.Jr., Pitchford, M., L., Schichtel, B.A., and *Watson, J.G.,* 2011: Spatial and Seasonal Patterns and Temporal Variability of Haze and its Constituents in the United States. Report V: June 2011. IMPROVE report, Cooperative Institute for Research in the Atmosphere, Colorado State University, Fort Collins, USA.

Hidy, G.M., Mueller, P.K., and *Tong, E.Y.,* 1978: Spatial and temporal distributions of airbone sulfate in parts of the United States, *Atmos. Environ. 12,* 735.

Horvath, H., 1992: Effect on visibility, weather and climate. In (Eds. *Radojevicc M.* and *Harrison R.M.*) Atmospheric Acidity: Sources, Consequences and abatement Elsevier Applied Science, London, 435-466.

Horvath, H., 1995: Estimation of the average visibility in central Europe, *Atmos. Environ., 29,* 241–246.

Jung, J., Lee, H., Kim, Y.J., Liu, X., Zhang, Y., Hu, M. and *Sugimoto, N.,* 2009: Optical Properties of Atmospheric Aerosols Obtained by in Situ and Remote Measurements during 2006 Campaign of Air Quality Research in Beijing (CAREBeijing-2006). *J. Geophys. Res. 114.*

Karanasiou, A., Diapouli, E., Cavalli, F., Eleftheriadis, K., Viana, M., Alastuey, A., Querol, X., Reche, C., 2011: On the quantification of atmospheric carbonate carbon by thermal/optical analysis protocols. *Atmos. Meas. Tech., 4,* 2409–2419.

Kim, K.W., 2015: Optical Properties of Size-Resolved Aerosol Chemistry and Visibility Variation Observed in the Urban Site of Seoul, Korea. *Aerosol Air Qual. Res. 15,* 271–283.

Koschmieder, H., 1924: Theorie der horizontalen sichtweite, Beitr. *Phys. frei. Atmos., 12,* 171–181.

Maenhaut, W., Raes, N., Chi, X., Cafmeyer, J., Wang, W., and *Salma, I., 2005:* Chemical composition and mass closure for fine and coarse aerosols at a kerbside in Budapest, Hungary, in spring 2002, *X Ray Spectrom., 34,* 290–296.

*Malm, W.C., Sisler, J. F., Huffman, D., Eldred, R. A.,*and *Cahill, T. A.,* 1994: Spatial and seasonal trends in particle concentration and optical extinction in the United States, *J Geophys Res. 99,* 1347–1370.

Malm, W.C., Schichtel, B.A., Barna, M.G., Gebhart, K.A., Rodriguez, M.A., Collett Jr., J.L., Carrico, C.M., Benedict, K.B., Prenni, A.J., and *Kreidenweis, S.M.,* 2013: Aerosol species concentrations and source apportionment of ammonia at Rocky Mountain National Park, *J. Air Waste Mgmt. Assn. 63,* 1245-1263.

Matta, E., Facchini, M.C., Decesari, S., Mircea, M., Cavalli, F., Fuzzi, S., Putaud, J.-P. and *Dell'Acqua, A.,* 2003: Mass closure on the chemical species in size-segregated atmospheric aerosol collected in an urban area of the Po Valley, Italy. *Atmos. Chem. Phys., 3,* 623–637.

Mészáros, E., 1999: Fundamentals of Atmospheric Aerosol Chemistry. Akadémiai Kiadó, Budapest.

Nemuc, A., Vasilescu, J., Talianu, C., Belegante, L., and *Nicolae, D.,* 2013: Assessment of aerosol's mass concentrations from measured linear particle depolarization ratio (vertically resolved) and simulations. *Atmos. Meas. Tech., 6,* 3243–3255.

Ouimette, J.R., and *Flagan R.C.,* 1982: The extinction coefficient of multicomponent aerosols. *Atmos. Environ. 16,* 2405–2419.

Pan, X.L., Yan, P., Tang, J., Ma, J.Z., Wang, Z.F., Gbaguidi, A., and *Sun, Y.L.,* 2009: Observational study of influence of aerosol hygroscopic growth on scattering coefficient over rural area near Beijing mega-city. *Atmos. Chem. Phys. 9,* 7519–7530.

Reche, C., Querol, X., Alastuey, A., Viana, M., Pey, J., Moreno, T., Rodríguez, S., Gonzalez, Y., Fernández-Camacho, R., de la Rosa, J., Dall'Osto, M., Prevôt, A.S.H., Hueglin, C., Harrison, R.M., and *Quincey, P.,* 2011: New considerations for PM, Black Carbon and particle number concentration for air quality monitoring across different European cities, *Atmos. Chem. Phys., 11,* 6207– 6227.

Seinfeld, J.H. and *Pandis, S.N.,* 1998: Atmospheric Chemistry and Physics. John Wiley & Sons.

Sillanpää, M., Frey, A., Hillamo, R., Pennanen, A.S. and *Salonen, R.O.*, 2005: Organic, elemental and inorganic carbon in particulate matter of six urban environments in Europe. *Atmos. Chem. Phys., 5*, 2869–2879.

Singh, A. and Dey, S., 2012: Influence of aerosol composition on visibility in megacity Delhi. *Atmos. Environ. 62*, 367–373.

Stelson, A.W. and *Seinfeld, J.H.*, 1981: Chemical mass accounting of urban aerosol. *Environ. Sci. Technol. 15*, 671–679.

Tao, J., Cao, J.-J., Zhang, R.-J, Zhu, L. H., Zhang T., Shi S., and *Chan, C.-Y.*, 2012: Reconstructed light extinction coefficients using chemical compositions of PM2.5 in winter in urban Guangzhou, China. *Adv. Atmos. Sci., 29*, 359–368.

Zhou, J., Swietlicki, E. and Berg, O.H., 2001: Hygroscopic properties of aerosol particles over the central Arctic Ocean during summer. J Geophys Res. 32, 32111-32123.

Virkkula, A., Backman, J., Aalto, P.P., Hulkkonen, M., Riuttanen, L., Nieminen, T., dal Maso, M., Sogacheva, L., de Leeuw, G., and Kulmala, M., 2011: Seasonal Cycle, Size Dependencies, and Source Analyses of Aerosol Optical Properties at the SMEAR II Measurement Station in Hyytiälä, Finland. *Atmos. Chem. Phys. 11*, 4445–4468.

Waked, A., Favez, O., Alleman, L. Y., Piot, C., Petit, J.-E., Delaunay, T., Verlinden, E., Golly, B., Besombes, J.-L., Jaffrezo, J.-L., and *Leoz-Garziandia, E.*, 2014: Source apportionment of PM_{10} in a north-western Europe regional urban background site (Lens, France) using positive matrix factorization and including primary biogenic emissions, *Atmos. Chem. Phys., 14*, 3325-3346.

Wang, G., Xie, M., Hu, S., Gao, S., Tachibana, E., and *Kawamura, K.*, 2010: Dicarboxylic acids, metals and isotopic compositions of C and N in atmospheric aerosols from inland China: implications for dust and coal burning emission and secondary aerosol formation, *Atmos. Chem. Phys.*, 10, 6087–6096.

IDŐJÁRÁS

Quarterly Journal of the Hungarian Meteorological Service
Vol. 120, No. 2, April – June, 2016, pp. 183–198

Analysis of annual and seasonal temperature trends using the Mann-Kendall test in Vojvodina, Serbia

Milivoj B. Gavrilov[1*], **Ivana Tošić**[2], **Slobodan B. Marković**[1], **Miroslava Unkašević**[2], and **Predrag Petrović**[3]

[1]*University of Novi Sad, Faculty of Sciences, Chair of Physical Geography, Trg Dositeja Obradovića 3, 21000 Novi Sad, Serbia*

[2]*University of Belgrade, Faculty of Physics, Institute of Meteorology, Dobračina 16, 11000 Belgrade, Serbia*

[3]*Republic Hydrometeorological Service of Serbia, Kneza Višeslava 66, 11000 Belgrade, Serbia*

[*]*Corresponding author E-mail*: gavrilov.milivoj@gmail.com

(Manuscript received in final form March 9, 2015)

Abstract—The annual and seasonal trends of mean, maximum, and minimum temperatures were analyzed on the territory of Vojvodina, north Serbia. We used observed, quality controlled, homogenized, and spatially averaged data from 9 meteorological stations during two periods: 1949–2013 and 1979–2013. Positive trends were found in 29 out of the 30 analyzed time series using a linear tendency (trend) equation, while negative trends were found in only 1 case. After the application of the classical Mann-Kendall (MK) test, statistically significant positive trends were confirmed in 15 series, while in remaining cases, statistically significant trends were not confirmed. After applying the modified MK test, positive trends were found in 26 series, and 4 cases were with no trend. We find that significant positive trends are dominated during the year, spring and summer; and they are most numerous in the time series of monthly mean temperatures. In accordance with the behavior of analyzed trends, the increase of temperatures is dominant in Vojvodina.

Key-words: annual and seasonal temperature trends, Mann-Kendall test, Vojvodina

1. Introduction

According to the *IPCC* (2007) report, the average global surface temperature of the world has increased by 0.74 °C in the past 100 years. This increase in the global temperature is not homogeneously distributed over the Earth's surface. It varies among regions and locations. The seasonal and annual Central European series of the mean temperature exhibited an increasing trend during the period 1951–1990 in most regions (*Brázdil et al.*, 1996). Using data recorded daily from 168 stations across Europe, *Klein Tank et al.* (2002) showed that trends in mean temperature have increased during the period from 1946 to 1999.

Analysis of the surface air temperature observed at stations located in all regions of the Mediterranean basin indicated a cooling during the period 1955–1975, and a strong warming during the 1980s and the first half of the 1990s (*Piervitali et al.*, 1997). Warming trends in the Mediterranean region (*Böhm et al.*, 2001; *Alcamo et al.*, 2007) occurred largely during the summer season, thereby intensifying summertime drought and irrigation problems. *Brunetti et al.* (2004) noted that the temperature trend in Italy was positive for each season in the south, and for autumn and winter in the north. *Feidas et al.* (2004) examined trends of annual and seasonal surface air temperature time series for 20 stations in Greece for the period 1955–2001. They found that Greece, in general, exhibits a cooling trend in winter, whereas in summer it exhibits an overall warming trend. The significant increase in average temperature over the Iberian Peninsula in recent decades was found by *Brunet et al.* (2007).

In Serbia, the mean summer temperature increased in Belgrade after 1975 (*Unkašević et al.*, 2005). Using the extreme temperatures at 15 meteorological stations during the period 1949–2009, an analysis of the extreme temperature indices suggested that the Serbian climate has become warmer over the last 61 years (*Unkašević* and *Tošić*, 2013). In addition to these results, the climate in Serbia was studied in other recent papers (*Đorđević*, 2008; *Unkašević* and *Tošić*, 2009a; *Gavrilov et al.*, 2010; *Pavlović Berdon*, 2012). Also, the weather and climate of Vojvodina were investigated in several papers (*Gavrilov et al.*, 2011; *Hrnjak et al.*, 2014; *Tošić et al.*, 2014; *Gavrilov et al.*, 2015).

In this study, we focus on analyzing the recent trends in the annual and seasonal temperatures over Vojvodina, Serbia. We find that the period from 1949 to 2013 contains more than two 30-year climatic cycles and, therefore, the results could be a good indicator for recent climate interpretations. Our paper is organized as following: Section 2 presents a description of the research region and data; methodology is described in detail in Section 3; the obtained results are presented in Section 4; and discussion and conclusions are given in Sections 5 and 6.

2. Data

2.1. Region

Vojvodina is a region in northern Serbia, located in the southeastern part of the Carpathian (Pannonian) Basin, encompassing the confluence area of the Danube, Sava, and Tisa rivers (*Fig. 1*). More than 60 % of this lowland area is covered by loess and loess-like sediments (*Marković et al.*, 2008). The most distinctive landforms of the Vojvodina region are two mountains: Fruška Gora Mountain, which is situated between the Danube and Sava rivers, and Vršac Mountain, which is located in the southeastern part of the region. In addition to these physical features of the region, there are sandy and lower areas-alluvial plains.

The climate of Vojvodina is moderate continental with cold winters and hot and humid summers, and with a large range of extreme temperatures featuring inconsistent amounts of rainfall over the course of months. The average annual air temperature was 11.1 °C and annual amount of precipitation (*Tošić et al.*, 2014) was 606 mm between 1949 and 2006.

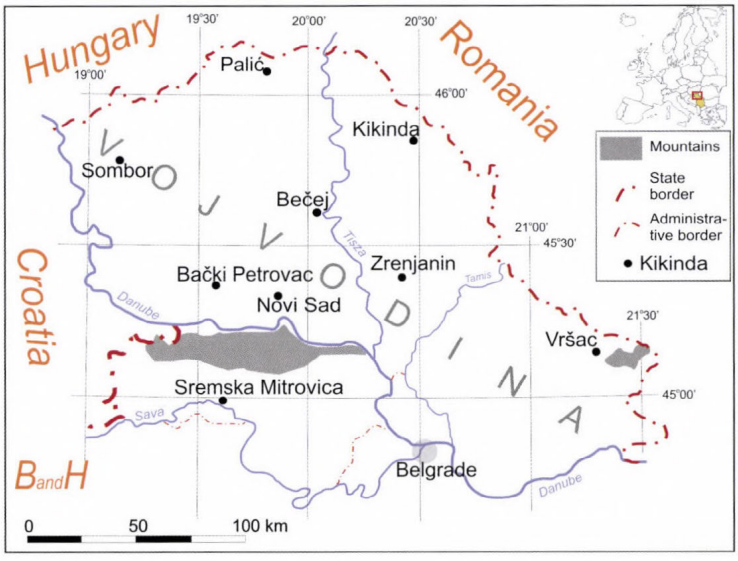

Fig. 1. The region of Vojvodina and position of meteorological stations.

2.2. Data used

In this work, an analysis of surface air temperature trends in Vojvodina from 9 meteorological stations was performed. The locations of stations are presented in *Fig. 1* and their geographical coordinates and altitudes are given in *Table 1* in accordance with the *Republic Hydrometeorological Service of Serbia* (2014). All stations have relatively similar altitudes, varying between 75 m and 102 m. Only stations that have almost continuous raw data sets of temperatures for the period between 1949 and 2013 were selected. The selected period is the longest of all observation periods in Vojvodina with standardized measurements and controlled data (*WMO*, 2012) on a large number of meteorological stations. Thus, it can be considered that these selected data and period are the most representative for the region of Vojvodina.

Table 1. List of meteorological stations, their geographical parameters and missing data for the period 1949–2013

Meteorological stations	Geographical parameters			Missing data (%)		
	Latitude (°)	Longitude (°)	Altitude (m)	T	T_x	T_n
Bački Petrovac	45.37	19.57	85	0.05	0.05	0.05
Bečej	45.63	20.03	75	0.54	1.57	1.54
Kikinda	45.85	20.47	81	0.0	0.0	0.0
Novi Sad	45.33	19.85	86	0.0	0.0	0.0
Palić	46.10	19.77	102	0.76	0.38	0.38
Sombor	45.77	19.15	87	1.54	1.54	1.54
Sremska Mitrovica	45.00	19.55	82	0.0	0.0	0.0
Vršac	45.15	21.32	83	0.0	0.0	0.0
Zrenjanin	45.37	20.42	80	0.0	0.0	0.0

Three used raw data sets of surface air temperatures are: monthly mean temperatures, T, monthly maximum temperatures, T_x, and monthly minimum temperatures, T_n. Monthly mean temperatures are obtained as the average of the daily mean temperatures, while monthly maximum/minimum temperatures are the maximum/minimum values of daily temperatures in corresponding month. As shown in *Table 1*, raw data were complete at five stations, while at four stations missing data were varied from 0.05 % to 1.57 %. We used the method/software MASH (*Szentimrey*, 1999) for data homogenization and filling in the missing raw data in accordance with the *CarpatClim project* (2014).

Of these three homogenized data sets, new data sets were created: average of stations over the territory of Vojvodina annual and seasonal mean, maximum, and minimum temperatures, T, T_x, T_n, respectively. The standard seasons definitions are used: winter (DJF), spring (MAM), summer (JJA), and autumn

(SON) during two periods: 1949–2013 (*P*1), and 1979–2013 (*P*2). We expect from the data processing in the first period to give the state of surface air temperature trends for longest continuous observation period (65 years) in Vojvodina. We also expect the second period to show the temperature trends during the last 35 years (5 years more than one 30-year climate standard), when global warming became the most intense (*Hardy*, 2006).

In the continuation of this research, the data base was formed by year (Y), four seasons (DJF, MAM, JJA, and SON), three types of temperatures (T, T_x, and T_n), and two periods (*P*1 and *P*2). The total number of series was 30 that were used for the trend calculation. Each of these 30 cases is marked with the acronym consisting of the abbreviation for the year/seasons, period, and type of temperature (*Table 2*).

Table 2. List of 30 time series to calculate surface air temperature trends in Vojvodina

	Year	**Winter**	**Spring**	**Summer**	**Autumn**
T	Y-T-*P*1	DJF-T-*P*1	MAM-T-*P*1	JJA-T-*P*1	SON-T-*P*1
	Y-T-*P*2	DJF-T-*P*2	MAM-T-*P*2	JJA-T-*P*2	SON-T-*P*2
T_x	Y-T_x-*P*1	DJF-T_x-*P*1	MAM-T_x-*P*1	JJA-T_x-*P*1	SON-T_x-*P*1
	Y-T_x-*P*2	DJF-T_x-*P*2	MAM-T_x-*P*2	JJA-T_x-*P*2	SON-T_x-*P*2
T_n	Y-T_n-*P*1	DJF-T_n-*P*1	MAM-T_n-*P*1	JJA-T_n-*P*1	SON-T_n-*P*1
	Y-T_n-*P*2	DJF-T_n-*P*2	MAM-T_n-*P*2	JJA-T_n-*P*2	SON-T_n-*P*2

3. Methodology

Three statistical approaches were used to analyze the temperature trends in 30 time series. First, the tendency (linear trend) equation (e.g., *Draper* and *Smith*, 1966) was calculated for each time series. Second, in all cases, the trend magnitude was calculated from the trend equation. Finally, in the third approach, all trends were assessed using the Mann-Kendall (MK) test, completely independent of the first approach (*Mann*, 1945; *Kendall*, 1975; *Gilbert*, 1987).

3.1. The trend equation

The first statistical approach was to calculate the trend equation of temperature using linear regression (e.g., *Draper and Smith*, 1966), as

$$y = ax + b, \tag{1}$$

where y is the temperature in °C, a is the slope, x is the time in years, and b is the temperature at the beginning of the period.

This approach has been long utilized in this type of research (e.g., *Wibig* and *Glowicki*, 2002; *Feidas et al.*, 2004), because it gives results which are simple to interpret; both graphically and analytically on the basis of the shape and parameters of the trend equation. For instance, the sign of the temperature trend depends on the value of the slope. In this kind of interpretation when the slope is greater than zero, less than zero, or equal to zero, the sign of the *trend is positive* (increase), *negative* (decrease), or *there is no trend* (no change), respectively.

3.2. The trend magnitude

In the second statistical approach, the trend magnitude was defined, as the difference in temperature between the beginning and the end of the period, which was obtained from the linear trend equation (*Gavrilov et al.*, 2015), or which is calculated as follows,

$$\Delta y = y(P_b) - y(P_e), \tag{2}$$

where Δy is the trend magnitude in °C. Values $y(P_b)$ and $y(P_e)$ represent temperatures from the trend equation in the beginning, P_b, and at the end period, P_e. Recall that two periods $P1$ and $P2$ have two beginning: $P_b = 1949, 1979$; and common end: $P_e = 2013$, with the exception of winter, where the periods were shorter for one year at the beginning and the end.

For a better understanding of the trend magnitude, we note the following. First, when Δy is greater than zero, less than zero, or equal to zero, the sign of the trend is *negative* (decrease), *positive* (increase), or *no trend* (no change), respectively. Second, when Δy is less than or equal to the standard error of the temperature measurement, certainly *there is no trend.*

The trend equation, trend magnitude, linear trend line, and annual course of temperature were computed and plotted for each time series using MATLAB scripts.

3.3. The Mann-Kendall test

In the third statistical approach, the MK test was applied to assess the significance of temperature trends. This test is widely used in the analysis of the climatological time series, for example: temperature and precipitation in earlier researches (e.g., *Gan*, 1995), as well as in recent researches (e.g., *Mavromatis* and *Stathis*, 2011; *Karmeshu*, 2012); extreme temperatures (e.g., *Serra et al.*, 2001; *Wibig* and *Glowicki*, 2002); hail (e.g., *Gavrilov et al.*, 2010, 2013); aridity

(e.g., *Hrnjak, et al.*, 2014); evapotranspiration (e.g., *Tabari et al.*, 2011); and atmospheric deposition (e.g., *Drapela* and *Drapelova,* 2011); then in the hydrological time series (e.g., *Yue* and *Wang*, 2004); and other geophysical time series, such as: freeze and thaw soil (e.g., *Sinha* and *Cherkauer*, 2008); because the MK test is simple and robust, it can cope with missing values and values below the detection limit.

According to the MK test, two hypotheses were tested: the null hypothesis, H0, that *there is no trend* in the time series; and the alternative hypothesis, Ha, that *there is a significant trend* in the series, for a given α significance level (e.g., *Onoz* and *Bayazit*, 2003). Probability, p, in percent was calculated (e.g., *Karmeshu*, 2012; *Gavrilov et al.*, 2017) to determine the level of confidence in the hypothesis. If the computed value p is lower than the chosen significance level α (e.g., α=5 %), the H0 (*there is no trend*) should be rejected, and the Ha (*there is a significant trend*) should be accepted. In case p is greater than the significance level α, the H0 (*there is no trend*) cannot be rejected. We used XLSTAT software (http://www.xlstat.com/en/) for calculating the probability, p, and hypothesis testing.

It is considered that accepting the Ha indicates that a trend is statistically significant. On the other hand, acceptance of the H0 implies that there is no trend (no change), while often in practice, the trend equation and the trend magnitude indicates that there is a trend. Therefore, to reduce the doubt in analyzing the temperature trends with two independent statistical approaches, trend equation and applying the previous or classical interpretation of the MK test, the modified interpretation of the MK test (*Gavrilov, et al.*, 2015; *Gavrilov, et al.*, 2017) will be used. The difference between these two MK tests is in the number of levels of confidence. The classic MK test has only two levels of confidence: (i) *there is a significant positive/negative trend* and (ii) *there is no trend.* The modified MK test declares four levels of confidence, when p is:

(1) less or equal than 5 %, *there is a significant positive/negative trend*;

(2) greater than 5 %, and less or equal than 30 %, *there is a moderately positive/negative trend*;

(3) greater than 30 %, and less or equal than 50 %, *there is a slightly positive/negative trend*; and

(4) greater than 50 %, *there is no trend.*

As it can be seen, in cases (1) and (4) both interpretations of the MK tests have the same meaning. Differences occur in cases (2) and (3), where the classical MK test claims *there is no trend*, and the modified MK test allows trend with reduced levels of confidence. It is clear that modified interpretation is more subtle, and it enables obtaining diverse assessments.

4. Results

4.1. Parameters of trend

Figs. 2–4 show annual and seasonal mean, maximum, and minimum temperatures during the period 1949–2013 with two trend equations (Eq. (1): above (1949–2013) and below (1979–2013); and two trend lines: for longer and shorter period, respectively. The trend magnitude, Δy, and the probability of the confidence, p, for each time series over the territory of Vojvodina are shown in *Table 3*, respectively.

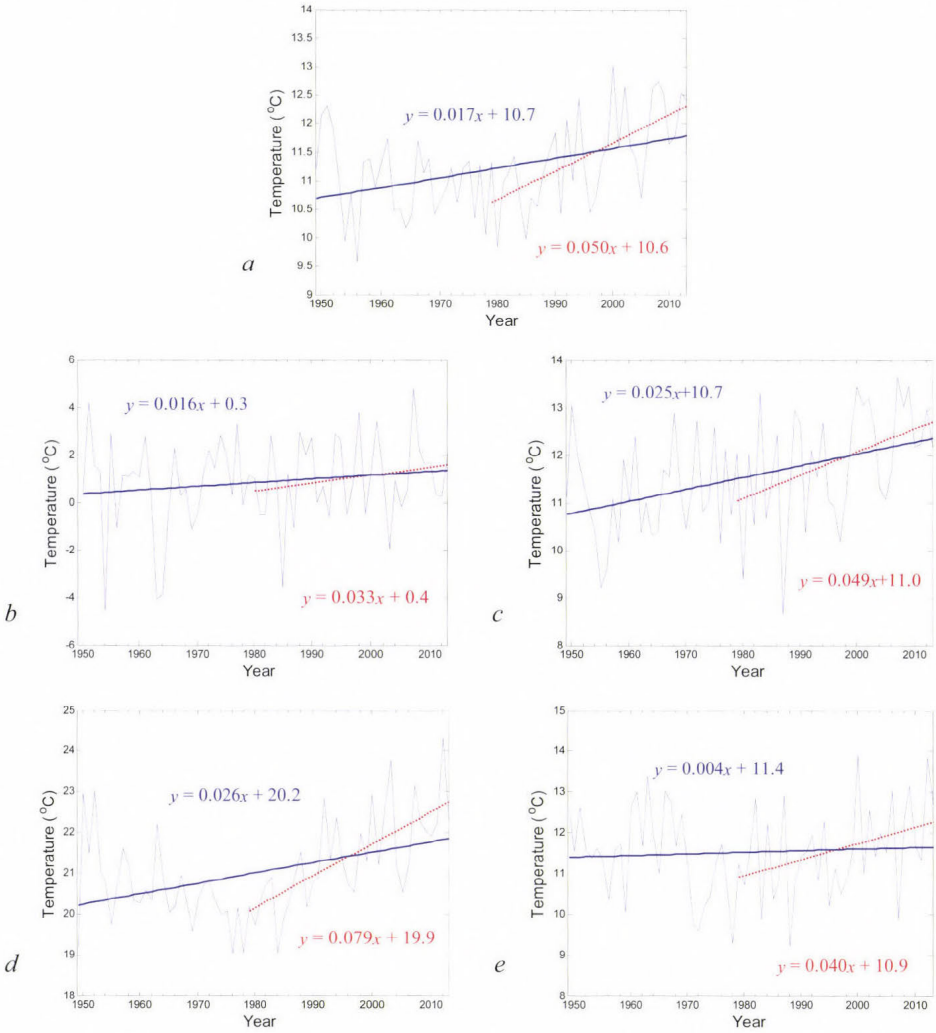

Fig. 2. Average annual and seasonal temperatures, trend equations, and trend lines for couples of time series: Y-*T*-*P*1 and Y-*T*-*P*2; DJF-*T*-*P*1 and DJF-*T*-*P*2; MAM-*T*-*P*1 and MAM-*T*-*P*2; JJA-*T*-*P*1 and JJA-*T*-*P*2; and SON-*T*-*P*1 and SON-*T*-*P*2 on panels a-e, respectively.

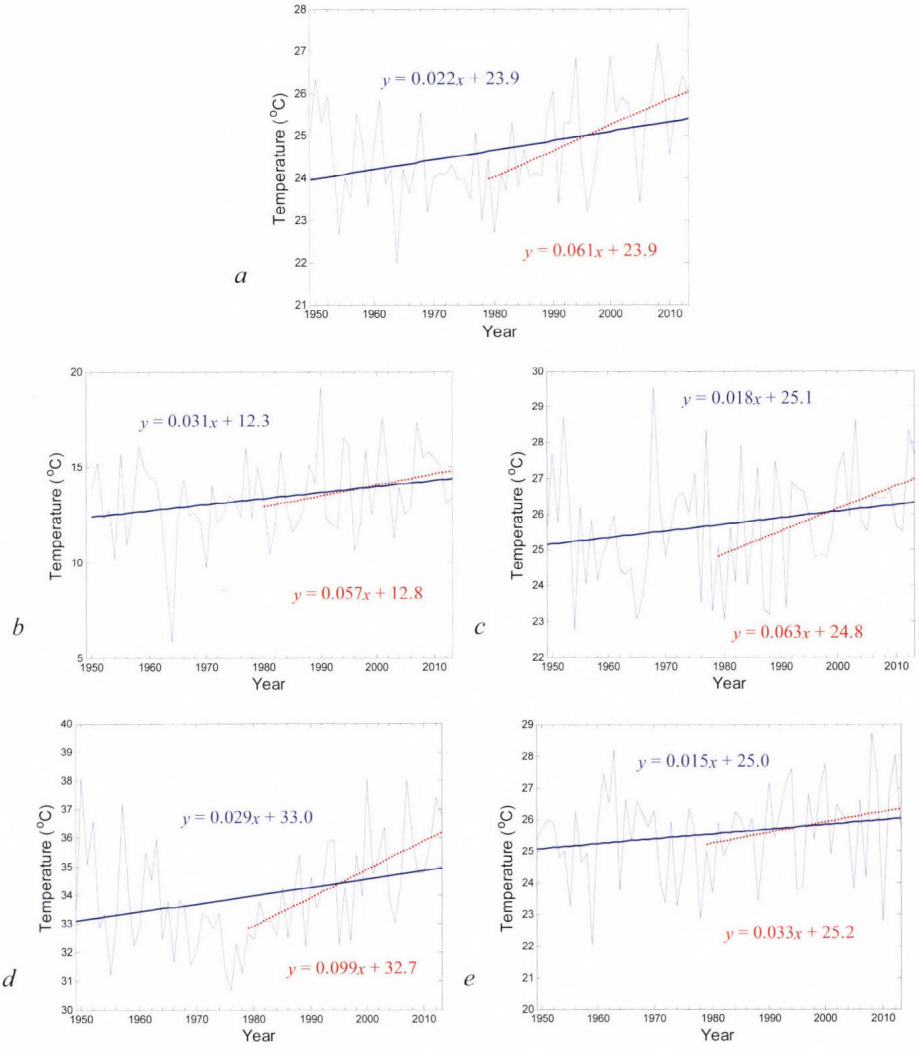

Fig. 3. As in *Fig. 2* but for T_x.

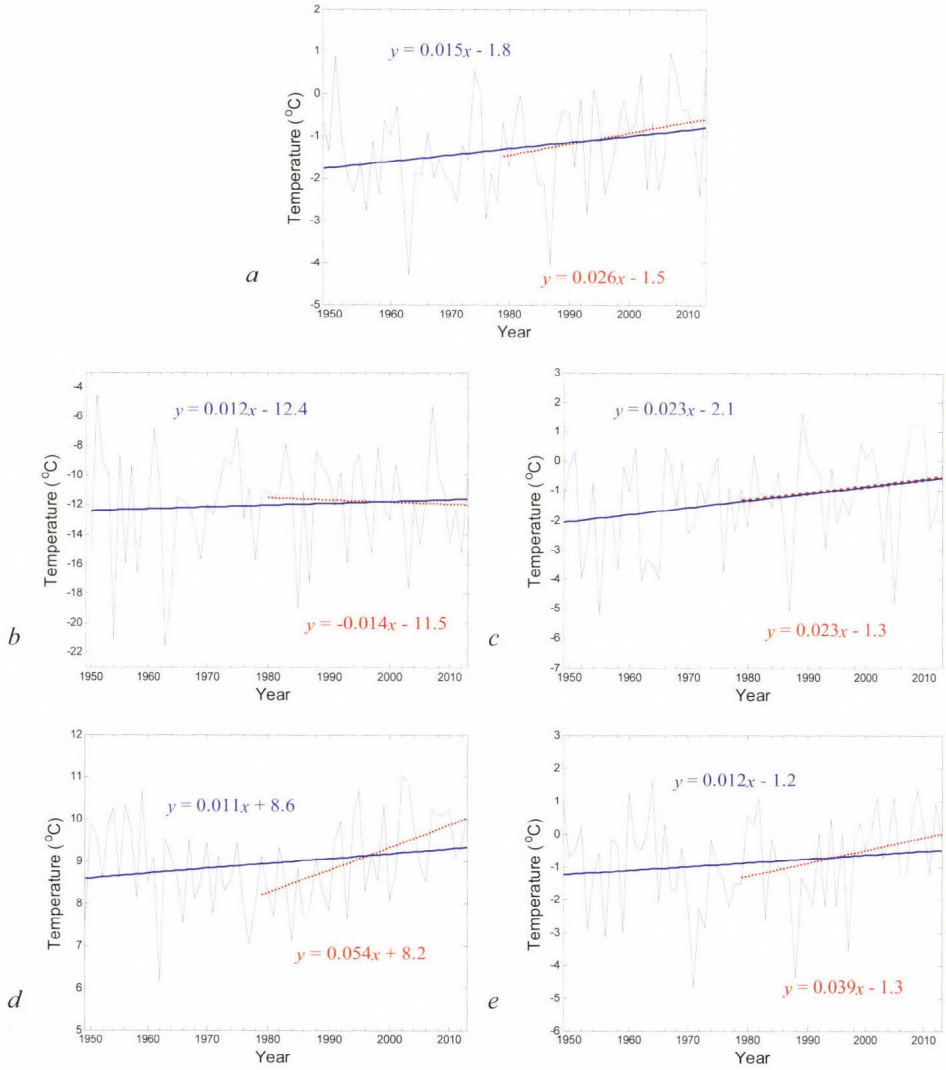

Fig. 4. As in *Fig. 2* but for T_n.

Table 3. The trend magnitude, Δy, and the probability of the confidences, p, for all time series

	T				T_x				T_n			
	*P*1		*P*2		*P*1		*P*2		*P*1		*P*2	
	Δy (°C)	p (%)	Δy (°C)	p (%)	Δy (°C)	p (%)	Δy (°C)	p (%)	Δy (°C)	p (%)	Δy (°C)	p (%)
Y	–1.1	0.13	–1.7	<0.01	–1.6	0.47	–2.1	0.04	–1.0	4.45	–0.9	24.65
DJF	–1.0	53.15	–1.1	36.11	–2.0	12.61	–1.9	11.00	–0.8	75.00	0.5	55.63
MAM	–1.6	0.07	–1.7	1.63	–1.2	5.86	–2.1	3.02	–1.5	3.24	–0.8	33.71
JJA	–1.6	0.10	–2.7	<0.01	–1.8	0.69	–3.4	0.01	–0.7	18.34	–1.8	0.27
SON	–0.2	60.64	–3.1	2.07	–1.0	8.84	–1.1	7.83	–0.7	12.92	–1.3	13.59

4.2. Evaluation of trends

In strictly formal terms, some trends can be observed in all cases (see *Figs. 2–4*). However, all trends do not have the same sign, magnitude, and probability. To obtain a final evaluation of the temperature trends in Vojvodina, all numerical parameters, the visual representation of trends and, most importantly, the results of both MK tests, were used.

Figs. 2–4 and *Table 3* show that the trend for 29 time series is *positive*, and it is *negative* only for the case DJF-T_n-*P*2. MK testing proves whether these statements are true.

As the computed probability values p for *P*1 cases: Y-*T*, MAM-*T*, JJA-*T*, Y-T_x, JJA-T_x, Y-T_n, and MAM-T_n; and for *P*2 cases: Y-*T*, MAM-*T*, JJA-*T*, SON-*T*, Y-T_x, MAM-T_x, JJA-T_x, and JJA-T_n, are lower than the significance level, α, the H0 should be rejected, and the Ha should be accepted for all of these cases. The risks to reject the H0 are lower than 4.45 %. The statement that *there is a significant trend* is correct in these cases with a probability greater than 95.55 % in both MK tests.

As values p for *P*1 seasons: DJF-*T*, SON-*T*, DJF-T_x, MAM-T_x, SON-T_x, DJF-T_n, JJA-T_n, and SON-T_n, and for *P*2 time series: DJF-*T*, DJF-T_x, SON-T_x, Y-T_n, DJF-T_n, MAM-T_n, and SON-T_n are greater than α, the H0 cannot be rejected. The risks to reject the H0 while it is true are between 5.86 % and 75.00 %. In accordance with the classical MK tests, all cases are declared as *there is no trend*; while the modified MK test declared the first, second, sixth, and thirteenth cases as *there is no trend*, the ninth and fourteenth cases as *there is a slightly positive trend*, and the remaining cases as *there is a moderately positive trend.*

In addition, *Figs. 2–4* show that in P2 the trend lines have greater slope in all time series for *T* and T_x, and in case T_n in 3 out of 5 time series. Only for the case DJF-T_n-*P*1 slope is greater than DJF-T_n-*P*2, while for the time series MAM-T_n-*P*1 and MAM-T_n-*P*2 slopes (a=0.023) are equal.

The main results of our analysis of temperature trends in Vojvodina are summarized in *Table 4*. The results are classified according to all time series, temperatures (T, T_x, T_n), and methods (the trend equation, the classical and the modified MK tests).

Table 4. The main results of the analysis of temperature trends in Vojvodina

Time series	The trend equation	The classical MK test	The modified MK test
T			
Y-*T*-*P*1	*positive trend*	*positive significant trend*	*positive significant trend*
Y-*T*-*P*2	*positive trend*	*positive significant trend*	*positive significant trend*
DJF-*T*-*P*1	*positive trend*	*no trend*	*no trend*
DJF-*T*-*P*2	*positive trend*	*no trend*	*positive slightly trend*
MAM-*T*-*P*1	*positive trend*	*positive significant trend*	*positive significant trend*
MAM-*T*-*P*2	*positive trend*	*positive significant trend*	*positive significant trend*
JJA-*T*-*P*1	*positive trend*	*positive significant trend*	*positive significant trend*
JJA-*T*-*P*2	*positive trend*	*positive significant trend*	*positive significant trend*
SON-*T*-*P*1	*positive trend*	*no trend*	*no trend*
SON-*T*-*P*2	*positive trend*	*positive significant trend*	*positive significant trend*
T_x			
Y-T_x-*P*1	*positive trend*	*positive significant trend*	*positive significant trend*
Y-T_x-*P*2	*positive trend*	*positive significant trend*	*positive significant trend*
DJF-T_x-*P*1	*positive trend*	*no trend*	*positive moderate trend*
DJF-T_x-*P*2	*positive trend*	*no trend*	*positive moderate trend*
MAM-T_x-*P*1	*positive trend*	*no trend*	*positive moderate trend*
MAM-T_x-*P*2	*positive trend*	*positive significant trend*	*positive significant trend*
JJA-T_x-*P*1	*positive trend*	*positive significant trend*	*positive significant trend*
JJA-T_x-*P*2	*positive trend*	*positive significant trend*	*positive significant trend*
SON-T_x-*P*1	*positive trend*	*no trend*	*positive moderate trend*
SON-T_x-*P*2	*positive trend*	*no trend*	*positive moderate trend*
T_n			
Y-T_n-*P*1	*positive trend*	*positive significant trend*	*positive significant trend*
Y-T_n-*P*2	*positive trend*	*no trend*	*positive moderate trend*
DJF-T_n-*P*1	*positive trend*	*no trend*	*no trend*
DJF-T_n-*P*2	*negative trend*	*no trend*	*no trend*
MAM-T_n-*P*1	*positive trend*	*positive significant trend*	*positive significant trend*
MAM-T_n-*P*2	*positive trend*	*no trend*	*positive slight trend*
JJA-T_n-*P*1	*positive trend*	*no trend*	*positive moderate trend*
JJA-T_n-*P*2	*positive trend*	*positive significant trend*	*positive significant trend*
SON-T_n-*P*1	*positive trend*	*no trend*	*positive moderate trend*
SON-T_n-*P*2	*positive trend*	*no trend*	*positive moderate trend*

5. Discussion

It is difficult to find identical results in neighboring areas, but there are similarities. For example, greater increase of the absolute maximum temperature (0.16 °C/year) than the absolute minimum temperature (0.12 °C/year) obtained *Unkašević et al.* (2005) for Belgrade during the period 1975–2003. Similarly to our results, *Brázdil et al.* (1996) concluded that in ten countries in Central and Southeast Europe between 1951 and 1990, there had been an increase in both annual maximum and minimum temperatures. *Brunetti et al.* (2004) found that trends in the annual temperature series ranged from 0.4 °C/(100 years) for the north to 0.7 °C/(100 years) for the south of Italy. These conclusions are in agreement with the *IPCC* report (2007), in which the increase in the global temperature is not homogeneously distributed on the Earth surface.

In *Fig. 2a* we show three characteristic time intervals in the behavior of the annual mean temperature. The higher temperatures are at the beginning and the end of the *P*1 period, and the lower temperatures are in the middle of the period from 1970s until the mid 1980s. Our results are in accordance with the results of *Unkašević* and *Tošić* (2009b). Analyzing the temperature data from 1949 to 2007, they found that the slow decrease of summer temperatures until 1975 was followed by a temperature increase that lasted until 2007 in Belgrade (Serbia). Obtained temperature changes in Vojvodina are very similar to the behavior of global temperature during the same period (*Hardy*, 2006), where the increase of the temperature was started in the mid-1980s. It seems that there is a coincidence of regional temperature changes in Vojvodina and global temperature change.

6. Conclusions

An analysis of annual and seasonal trends of mean, maximum, and minimum surface air temperatures in Vojvodina for two periods: 1949–2013 and 1979–2013 was performed. Temperature trends in 30 time series were analyzed using (i) the trend equation, (ii) the trend magnitude calculated from the trend equation, and (iii) the MK test in the classical and modified declaration. The main conclusion can be summarized as follows:

(a) In accordance with the trend equations, positive trends were found in 29 out of 30 time series, and negative trend was found in only one case.

(b) Using the classical MK test, significant positive trends were found in 15 series; 8 in the shorter period, and 7 in the longer period; and no trend was found in 15 cases. The significant positive trends are dominated during the year, spring, and summer, where it was found in 14 out of 18 cases. From the three types of temperatures, T, T_x, and T_n, significant positive trends were found 7, 5, and 3 times, respectively.

(c) Based on the modified MK test, positive (significant, moderate, and slight) trends were confirmed in 26 (15, 9, and 2, respectively) series.

(d) The increase of the temperature was found in 29 time series in a wide range of values from 0.2 °C to 2.0 °C for the longer period and from 0.8 °C to 3.4 °C for the shorter period. The decrease of the temperature was found only for the minimum temperatures during the winter for the shorter period. The increase of temperatures was higher for the shorter period, than for the longer period.

As shown, the positive temperature trends and the increase of temperatures are dominant in Vojvodina. This behavior of the temperature resembles the warming in the Northern Hemisphere (e.g., *CRU*, 2003).

Acknowledgements: This study was supported by the Serbian Ministry of Science, Education and Technological Development, under Grants No. 176013 and 176020. The authors are grateful to Mr. Momčilo Gavrilov, who carefully read the manuscript. The authors sincerely appreciate the efforts of anonymous reviewer in improving this manuscript.

References

Alcamo, J., Moreno, J.M., Nováky, B., Bindi, M., Corobov, R., Devoy, R.J.N., Giannakopoulos, C., Martin, E., Olesen, J.E. and *Shvidenko, A.*, 2007: Europe. In (Eds.: *Parry, M.L., Canziani, O.F., Palutikof, J.P., van der Linden, P.J., Hanson, C.E.*), Climate Change 2007: Impacts, Adaptation and Vulnerability. Contribution of Working Group II to the Fourth Assessment Report of the Intergovernmental Panel on Climate Change. Cambridge University Press, Cambridge, UK, 541–580.

Böhm, R., Auer, I., Brunetti, M., Maugeri, M., Nanni, T. and *Schöner, W.*, 2001: Regional temperature variability in the European Alps: 1760-1998 from homogenized instrumental time series. *Int. J. Climatol. 21*, 1779–1801.

Brázdil, R., Budíková, M., Auer, I., Böhm, R., Cegnar, T., Faško, P., Lapin, M., Gajić-Čapka, M., Zaninović, K., Koleva, E., Niedźwiedź, T., Ustrnul, Z., Szalai, S. and *Weber, R.O.*, 1996: Trends of maximum and minimum daily temperatures in central and southeastern Europe. *Int. J. Climatol. 16*, 765–782.

Brunet, M., Jones, P.D., Sigro, J., Saladie, O., Aguilar, E., Moberg, A., Della-Marta, P.M., Lister, D., Walther, A. and *López, D.*, 2007: Temporal and spatial temperature variability and change over Spain during 1850-2005. *J. Geophys. Res.: Atmosph. 112*, 1984–2012.

Brunetti, M., Buffoni, L., Mangianti, F., Maugeri, M. and *Nanni, T.*, 2004: Temperature, precipitation and extreme events during the last century in Italy. *Glob. Planet. Change 40*, 141–149.

CarpatClim (Climate of the Carpathian Region) project, 2014: http://www.carpatclim-eu.org/pages/deliverables/ (accessed 29 December 2014).

CRU (Climate Research Unit), 2003: Global average temperature change 1856–2003. http://www.cru.uea.ac.uk/cru/data/temperature/ (accessed 21 July 2014).

Feidas, H., Makrogiannis, T. and *Bora-Senta, E.*, 2004: Trend analysis of air temperature time series in Greece and their relationship with circulation using surface and satellite data: 1955-2001. *Theor. Appl. Climatol. 79*, 185–208.

Drapela, K. and *Drapelova, I.*, 2011: Application of Mann-Kendall test and the Sen's slope estimates for trend detection in deposition data from Bílý Kříž (Beskydy Mts., the Czech Republic) 1997–2010. *Beskydy 4*, 133–146.

Draper, N.R. and *Smith, H.*, 1966: Applied Regression Analysis. Wiley, New York.

Đorđević, S.V., 2008: Temperature and precipitation trends in Belgrade and indicators of changing extremes for Serbia. *Geographica Pannonica 12*, 62–68.

Gan, T.Y., 1995: Trends in air temperature and precipitation for Canada and north-eastern USA. *Int. J. Climatol. 15*, 1115–1134.

Gavrilov, M.B., Lazić, L., Pešić, A., Milutinović, M., Marković, D., Stanković, A. and *Gavrilov, M.M.*, 2010: Influence of Hail Suppression on the Hail Trend in Serbia. *Phys. Geography 31*, 441–454.

Gavrilov, M.B., Lazić, L., Milutinović, A., and *Gavrilov, M.M.*, 2011: Influence of Hail Suppression on the Hail Trend in Vojvodina, Serbia. *Geographica Pannonica 15*, 36–41.

Gavrilov, M.B., Marković, S.B., Zorn, M., Komac, B., Lukić, T., Milošević, M. and *Janićević, S.*, 2013: Is hail suppression useful in Serbia? - General review and new results. *Acta Geographica Slovenica 53*, 165–179.

Gavrilov, M.B., Marković, S.B., Jarad, A. and *Korać, V.M.*, 2015: The analysis temperature trends in Vojvodina (Serbia) from 1949 to 2006. *THERMAL SCIENCE 19*, 339–350.

Gavrilov, M.B., Marković, S.B., Janc, N., Nikolić, M., Valjarević, A., *Zorn, M., Komac, B., Punišić*, M. and *Bačević*, N., 2017: The assessment of average annual temperature trends using the Mann-Kendall test in the territory of Kosovo. *Acta Geographica Slovenica* (in press).

Gilbert, R.O., 1987: Statistical Methods for Environmental Pollution Monitoring. Wiley, New York.

Hardy, J.T., 2006: Climate Change - Causes, Effects and Solutions. Wiley. Chichester.

Hrnjak, I., Lukić, T., Gavrilov, M.B., Marković, S.B., Unkašević, M. and *Tošić*, I., 2014: Aridity in Vojvodina, Serbia. *Theor. Appl. Climatol. 115*, 323–332.

IPCC, 2007: *Climate Change*. The physical science basis. In (Eds.: *Solomon, S., Qin, D., Manning, M., Chen, Z., Marquis, M., Averyt, K.B., Tignor, M., Miller, H.L.*), Contribution of Working Group I to the Fourth Assessment Report of the Intergovernmental Panel on Climate Change. Cambridge University Press, Cambridge and New York.

Karmeshu, N., 2012: Trend Detection in Annual Temperature & Precipitation using the Mann Kendall Test - A Case Study to Assess Climate Change on Select States in the Northeastern United States. Master's thesis, University of Pennsylvania.

Kendall, M.G., 1975: Rank correlation methods. Charles Griffin, London.

Klein Tank, A.M.G., Wijngaard, J.B., Können, G.P., Böhm, R., Demarée, G., Gocheva, A., Mileta, M., Pashiardis, S., Hejkrlik, L., Kern-Hansen, C., Heino, R., Bessemoulin, P., Müller-Westermeier, G., Tzanakou, M., Szalai, S., Pálsdóttir, T., Fitzgerald, D., Rubin, S., Capaldo, M., Maugeri, M., Leitass, A., Bukantis, A., Aberfeld, R., Van Engelen, A.F.V., Forland, E., Mietus, M., Coelho, F., Mares, C., Razuvaev, V., Nieplova, E., Cegnar, T., Antonio López, J., Dahlström, B., Moberg, A., Kirchhofer, W., Ceylan, A., Pachaliuk, O., Alexander, L.V. and *Petrovic, P.*, 2002: Daily dataset of 20th-century surface air temperature and precipitation series for the European Climate Assessment. *Int. J. Climatol. 22*, 1441–1453.

Mann, H.B., 1945: Nonparametric tests against trend. *Econometrica 13*, 245–259.

Marković, S.B., Bokhorst, M., Vandenberghe, J., Oches, E.A., Zöller, L., McCoy, W.D., Gaudenyi, T., Jovanović, M., Hambach, U. and *Machalett, B.*, 2008: Late Pleistocene loess-paleosol sequences in the Vojvodina region, North Serbia. *J. Quaternary Sci. 23*, 73–84.

Mavromatis, T. and *Stathis, D.*, 2011: Response of the Water Balance in Greece to Temperature and Precipitation Trends. *Theor. Appl. Climatol. 104*, 13–24.

Onoz, B. and *Bayazit, M.*, 2003: The Power of Statistical Tests for Trend Detection. *Turkish J. Engineer. Environ. Sci. 27*, 247–251.

Pavlović Berdon, N., 2012: The Impact of Arctic and North Atlantic Oscillation on Temperature and Precipitation Anomalies in Serbia. *Geographica Pannonica 16*, 44–55.

Piervitali, E., Colasino, M. and *Conte, M.*, 1997: Signals of climatic change in the Central-Western Mediterranean basin. *Theor. Appl. Climatol. 58*, 211–219.

Republic Hydrometeorological Service of Serbia (*RHSS*), 2014: Website of the RHSS, http://www.hidmet.gov.rs/ (accessed 21 July 2014).

Serra, C., Burgueño, A. and *Lana, X.*, 2001: Analysis of maximum and minimum daily temperatures recorded at Fabra Observatory (Barcelona, NE Spain) in the period 1917–1998. *Int. J. Climatol. 21*, 617–636.

Sinha, T. and *Cherkauer, K.A.*, 2008: Time Series Analysis of Soil Freeze and Thaw Processes in Indiana. *J. Hydrometeorol. 9*, 936–950.

Szentimrey, T., 1999: Multiple Analysis of Series for Homogenization (MASH). Proceedings of the Second Seminar for Homogenization of Surface Climatological Data, Budapest, Hungary; WMO, WCDMP-No. 41, 27–46.

Tabari, H., Marofi, S., Aeini, A., Talaee, P.H. and *Mohammadi, K.*, 2011: Trend Analysis of Reference Evapotranspiration in the Western half of Iran. *Agricult. Forest Meteorol. 151*, 128–136.

Tošić, I., Hrnjak, I., Gavrilov, M.B., Unkašević, M., Marković, S.B. and *Lukić, T.*, 2014: Annual and seasonal variability of precipitation in Vojvodina, Serbia. *Theor. Appl. Climatol. 117*, 331–341.

Unkašević, M., Vujović, D. and *Tošić, I.*, 2005: Trends in extreme summer temperatures at Belgrade. *Theor. Appl. Climatol. 82*, 99–205.

Unkašević, M. and *Tošić, I.*, 2009a: Changes in the extreme daily winter and summer temperatures at Belgrade. *Theor. Appl. Climatol. 89*, 239–244.

Unkašević, M. and *Tošić, I.*, 2009b: An analysis of heat waves in Serbia. *Glob. Planetary Change 65*, 17–26.

Unkašević, M. and *Tošić, I.*, 2013: Trends in temperature indices over Serbia: relationships to large-scale circulation patterns. *Int. J. Climatol. 33*, 3152–3161.

Wibig, J. and *Glowicki, B.*, 2002: Trends of minimum and maximum temperature in Poland. *Climate Res. 20*, 123–133.

WMO (*World Meteorological Organization*), 2012: Technical Regulations, Volume I: General Meteorological Standards and Recommended Practices. Documents No. 2. Geneva, World Meteorological Organization, Switzerland.

Yue, S. and *Wang, C.*, 2004: The Mann-Kendall Test Modified by Effective Sample Size to Detect Trend in Serially Correlated Hydrological Series. *Water Resour. Manage. 18*, 201–218.

IDŐJÁRÁS

Quarterly Journal of the Hungarian Meteorological Service
Vol. 120, No. 2, April – June, 2016, pp. 199–229

Wind tunnel and computational fluid dynamics study of wind conditions in an urban square

Márton Balczó* and **András Tomor**

Theodore von Kármán Wind Tunnel Laboratory
Department of Fluid Mechanics, Faculty of Mechanical Engineering,
Budapest University of Technology and Economics
Bertalan L. u. 4-6, H-1111 Budapest, Hungary

Authors E-mail: balczo@ara.bme.hu; tomor@ara.bme.hu

**Corresponding author*

(Manuscript received in final form March 23, 2015)

Abstract—Recognizing the role of urban squares in city life, the paper focuses on wind conditions at squares, with the objective to understand the building-scale flow phenomena influencing the wind comfort of pedestrians and the dispersion of pollutants. Wind tunnel testing of a selected square has been carried out at two wind directions, as well as accompanying computational fluid dynamics (CFD) simulations were performed using the MISKAM microscale model. The high spatial resolution experimental and CFD data allowed the identification of flow structures, like separation bubbles, vortices, high-speed zones in and around the square. Based on the analysis of numerical and experimental data obtained, the MISKAM model is able to resolve the flow field in a complex urban setting with some limitations. In a second step, the model was then used to run further numerical simulations, to compare fully built-up areas to an area with a square, and to assess the influence of tree plantings on the square. Results regarding the latter indicate that below tree crown height, flow velocity and turbulent kinetic energy are both decreased by about one fourth due to the vegetation. It is also shown that the presence of the square increases wind speed in connecting streets and induces longitudinal flows even in streets perpendicular to the approaching wind direction. The time-resolved wind tunnel measurements also allowed presenting the local velocity statistics as wind roses. Using these, we identified locations with non-isotropic turbulence and alternating wind directions.

Key-words: urban square, flow field, velocity fluctuation, urban vegetation, wind tunnel

1. Introduction

Urban flow and dispersion has been the subject of hundreds of research papers in the past, though only review articles (*Britter* and *Hanna,* 2003; *Ahmad et al.,* 2005; *Belcher et al.,* 2013; *Blocken,* 2014) may be cited here. While there is a huge selection of studies on ventilation and pollutant dispersion in urban street canyons, street intersections and regular arrangements of building blocks, there are few detailed analyses of the flow and dispersion phenomena specifically at urban squares. A square is defined as an open, typically four-sided area surrounded by buildings, with length to width ratio not necessarily equaling one. Squares fulfil important functions in urban life: they facilitate playing and sporting grounds, dining opportunities, markets, and open-air events. The creation of squares from the demolition of defunct residential or industrial buildings is an option in urban redevelopment programs. The longer residence time of pedestrians on squares explains why wind conditions and pollutant dispersion are of interest.

Only a few papers dealt with air pollution and flow phenomena specifically in urban squares. *Gadilhe et al.,(*1993) studied a semi-circular square and found recirculation zones behind the upstream located buildings of the square. *Parra et al.* (2010) showed using CFD simulations that depending on wind direction, locally released pollutants can be trapped in the separation vortices behind those buildings, and concentration distribution on the square is quite inhomogeneous. Obstacle resolving test cases of whole districts like the 'Michel-Stadt' semi-idealized urban dataset of *Bastigkeit* (2011) also include squares, among other features of an urban geometry, so there is experimental and numerical data available (*Hertwig et al.,* 2012; *Rákai* and *Kristóf,* 2013). However, the specialities of the flow in the squares were not separately addressed in these studies. Also, measurement data with higher spatial resolution would allow a more detailed analysis of the flow in the squares.

In the present paper, a typical urban square, József Nádor Square (coordinates 47.498 N, 19.050 E) in downtown Budapest will be investigated. It measures approximately 150×60 m, and is surrounded from all sides by building blocks of 28 m average height. The connecting streets are relatively narrow; their width to height (w/h) ratio is about 0.5. The square has unfavorable ventilation. Moreover, on its northern side it is bordered by the extremely busy József Attila Street with approx. 2000 vehicles/hour in rush hours, emitting a considerable amount of pollutants.

The area is heavily polluted with concentration levels well above the limit, as it was proven in an earlier paper (*Balczó* and *Lajos,* 2012), in which we investigated the site by using CFD simulations of the surroundings. The annual averages of NO_x concentrations at ground level in the north of the square showed values about twice as high as the annual limit. Also, the data of the on-site air quality monitoring station was analyzed and compared to the CFD

results. CFD predictions of annual NO_x averages deviated just 16% or less from the measured concentration values.

In the present study, wind tunnel measurements of a 1:350 scale model and computational fluid dynamics (CFD) simulations were carried out to understand the flow phenomena in the square and its surroundings. The flow field measurements were performed in a Göttingen-type wind tunnel by using laser-doppler velocimetry (LDV). In order to achieve proper flow field results, an urban-type atmospheric boundary layer was modeled in the wind tunnel and checked by vertical profile measurements.

The flow around exactly the same model geometry was simulated using the MISKAM flow and dispersion model, developed by *Eichhorn et al.*(1988). This CFD model solves the Reynolds-averaged Navier-Stokes (RANS) equations on a Cartesian non-equidistant grid and applies a modified K-ε closure adapted to urban flows. In the next step, the dispersion of pollutants can be calculated by solving the Reynolds-averaged advective diffusion equation. For detailed description of the current version 6, see *Eichhorn* (2011). The model underwent detailed evaluation in the past decade both according to the evaluation guideline VDI 3783/9 (*VDI,* 2005) performed by *Eichhorn* and *Kniffka* (2010) and it also took part in the model evaluation study of the European research Action COST 732 (*Schatzmann et al.,* 2010). Evaluation using the more complex MUST data set was published by *Balczó* and *Eichhorn* (2009) and *Goricsán et al.* (2011), testing with other data sets by *Olesen et al.* (2009).

The MISKAM model is able to run on standard personal computers, and its applicability to problems in urban environment has been shown in several publications (*Benson et al.,* 2007; *Balczó et al.,* 2009; *Donnelly et al.,* 2009; *Belalcazar et al.,* 2010; *Flassak et al.,* 2010; *Balczó et al.,* 2011). MISKAM was used as wind field and turbulence input for other dispersion models (*Leuzzi et al.,* 2010; *Letzel et al.,* 2012).

Due its simple setup and handling, the code is not only used by experts with deep knowledge of fluid dynamics, but also by many environmental agencies, authorities, and consulting engineers. While the application of high-end CFD models (e.g., LES) is not realistic in the regulatory / air quality assessment field at the present, MISKAM and other purpose-built RANS models form a significant step forward from earlier non-CFD (Gaussian, empirical, etc.) models applied in this area, when more accuracy in urban micro scale investigations is needed. Thus, the secondary objective of this work is to assess the capabilities of a CFD RANS model intended for regulatory use on complex real-world geometry.

2. Experimental setup

2.1. Wind tunnel and measurement setup

Experiments were carried out in the 3.8 m long and 2.6 m wide open test section of the large horizontal wind tunnel of the Budapest University of Technology and Economics. Model and boundary layer generation devices are mounted on a horizontal plate of 2.5 m width. *Fig. 1* shows the measurement layout. During the measurements, the fibre-optic laser doppler velocimetry (LDV) probe accessed the flow from below through a glass plate; therefore, the flow was not disturbed by the probe. A two-component LDV system was applied; hence, the horizontal velocity components u and v could be determined using the mentioned arrangement. The system consists of an air-cooled 300 mW Argon-Ion laser, generating a multiple frequency beam which goes through beam splitter and a Bragg cell to generate shifted and unshifted 488 and 514.5 nm (blue and green) beams. The four beams then pass through a fibre optic cable towards the LDV optics with 363 mm focal length and 61 mm clear aperture. Measurement volume has a diameter of 90 μm and 1.3 mm length. Laser light from the olive oil seeding particles passing the measurement volume is reflected back into the optics leading to photomultipliers and then digitized and analyzed by FSA3500 DSP-based signal processing unit. Burst frequencies are determined by autocorrelation. Burst velocities are weighted with gate time to get average velocities.

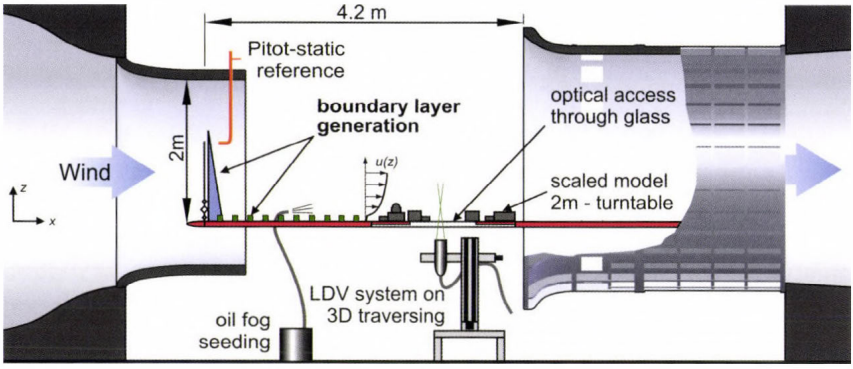

Fig. 1. The measurement layout including spikes, crossbars, and roughness elements in the preparatory section of the wind tunnel, the model arranged in the test section of the wind tunnel, and the LDV probe below the test section.

During the test campaign, different averaging times were used. At the incoming boundary layer measurement (Subsection 2.2), 200.000 velocity samples (bursts) were collected in up to 5 min, and during the flow field measurement of the square (Subsection 2.3), about 5000 samples were collected during the selected 50 s averaging time. The representativeness of measured velocity averages and standard deviations was checked during a few measurements of longer duration.

2.2. Atmospheric boundary layer generation

Following the well-established procedure of boundary layer generation in wind tunnels (see, e.g., *Gromke* and *Ruck,* 2005) and *Kozmar* (2011), an urban-type atmospheric boundary layer was generated in the wind tunnel modeling the natural ABL described in ESDU 72026 (*ESDU,* 1972), ESDU 85020 (*ESDU,* 2001), and VDI 3783/12 (*VDI,* 2004) by placing vortex generators, crossbars, and roughness elements into the preparatory section of the wind tunnel. The mentioned arrangement can be seen in *Fig. 1*. Vertical profiles of the developed boundary layer were measured using the LDV system at the centre of the turntable without the city model. Boundary layer parameters were determined from the mean velocities $\overline{u}(z)$ and $\overline{v}(z)$ in streamwise and lateral direction; as well as from their respective standard deviations $\sigma_u(z)$ and $\sigma_v(z)$. Turbulence intensity in the x- and y-direction (I_u and I_v) are defined as $\sigma_u(z)/\overline{u}(z)$ and $\sigma_v(z)/\overline{v}(z)$. Longitudinal integral length scale of turbulence using autocorrelation is given by:

$$L_{u,x} = \int_0^\infty R_{uu}(\Delta x)d\Delta x, \tag{1}$$

with R_{uu} – autocorrelation coefficient of the of the $u(z,t)$ – velocity time-series in x-direction.

Fig. 2 shows the profile of the dimensionless mean velocity into the main flow direction (a) and the turbulence intensity profiles I_u and I_v (b and c). Mean velocity u was approximated with the power law in the form

$$\frac{u(z)}{u_{ref}} = \left(\frac{z - d_0}{z_{ref} - d_0}\right)^{\alpha}, \tag{2}$$

where α is the exponent, z is the height, z_{ref} is the reference height (height of the modeled boundary layer), u_{ref} is the mean velocity at the reference height and d_0 is the displacement height. In order to obtain dimensionless mean velocities,

local velocities $u(z)$, were divided by the reference velocity u_{ref} = 4.60 m/s, which was measured at the reference height z_{ref} = 309.50 mm (108 m full scale).

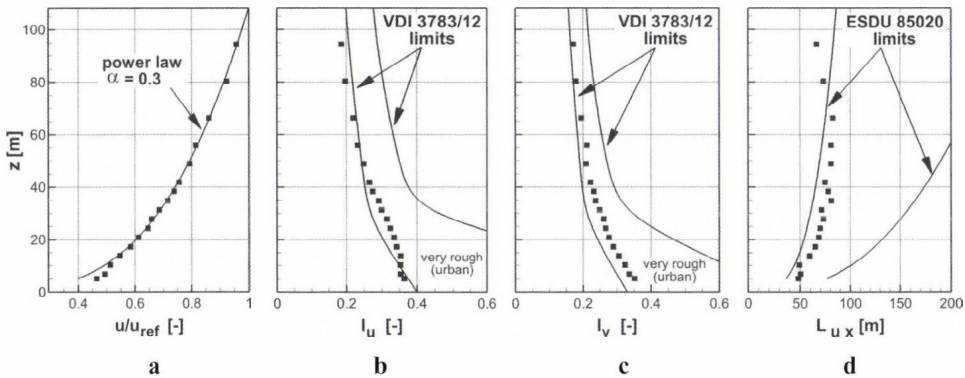

Fig. 2. Approach flow variables as a function of full scale height: (a) dimensionless mean velocity u/u_{ref}; (b) streamwise turbulence intensity I_u compared with urban type ABL turbulence given in VDI 3783/12; (c) lateral turbulence intensity I_v; (d) streamwise integral length scale of turbulence $L_{u,x}$ compared with ESDU 85020 data.

Displacement height was considered to be zero at the boundary layer measurement without the city model. (In measurements with the model on the turntable, the first few rows of buildings will elevate the boundary layer to the displacement height of ~ 0.75 h, as it can be seen later in the profiles of *Figs. 7–9.*)

The above parameters of an urban-type atmospheric boundary layer are specified by several guidelines and standards. According to ESDU (1972), the power law exponent α = 0.3 can be accepted for the representation of the urban atmospheric boundary layer. Turbulence intensity I_u profile shows some differences compared with VDI (2004) data; however, below the full scale height of 60 m, the agreement between the standard and measured data is perfect.

The integral length scale profile $L_{u,x}$ is shown in *Fig. 2 (d)*. The $L_{u,x}$ values – scaled up using the scale factor 1:350 – were compared with ESDU (2001) data. The integral length scale profile $L_{u,x}$ agrees well with the suggestions of the standard except above 80 m full scale height.

Based on the profile measurements, the generated atmospheric boundary layer was considered to be an accurate model of the ABL approaching the investigated square.

2.3. Model construction and the final measurement layout

The 1:350 scale model of the quarter around József Nádor Square was modeled with buildings prepared using waterjet-cut plywood and hotwire-cut rigid foam, and the whole model was placed on a wooden circular plate with a diameter of 2 m. An 800 × 800 mm opening in the middle of the plate covered by a pane of glass provided optical access to the flow from beneath the model. Although roof shape has certain effects on the flow, these effects were neglected in order to simplify the CFD model and mesh generation. According to this, the buildings of the experimental model were also modeled as blocks with flat rooftops and classified heights in 1.5 m steps. József Nádor Square and the surrounding quarter can be seen in *Fig. 3*, the model is shown in *Fig. 4*, left.

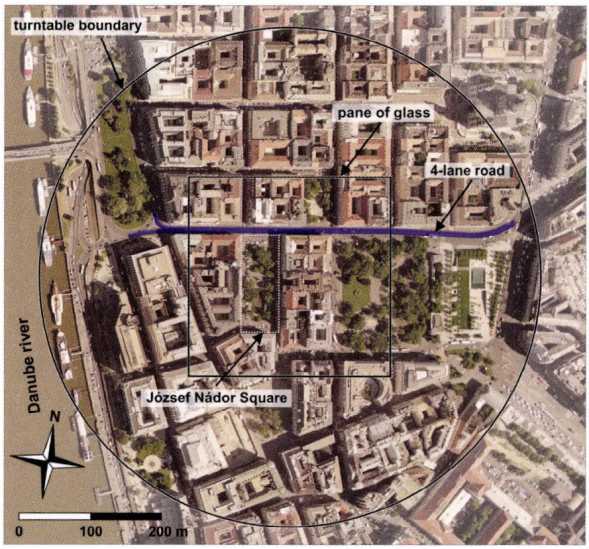

Fig. 3. Aerial photograph of József Nádor Square and the surrounding quarter; the edge of the wooden turntable and the pane of glass are also marked.

Flow velocities were measured along 23 vertical profiles and three horizontal planes (see later in *Fig. 5*). Local mean velocities, $\bar{u}$ and $\bar{v}$, were normalized to the reference velocity u_{ref} = 3.02 m/s, which was measured at the building mean height h = 80 mm during the boundary layer measurements; h is the mean building height in model scale. The mean building height in full scale is h = 28 m.

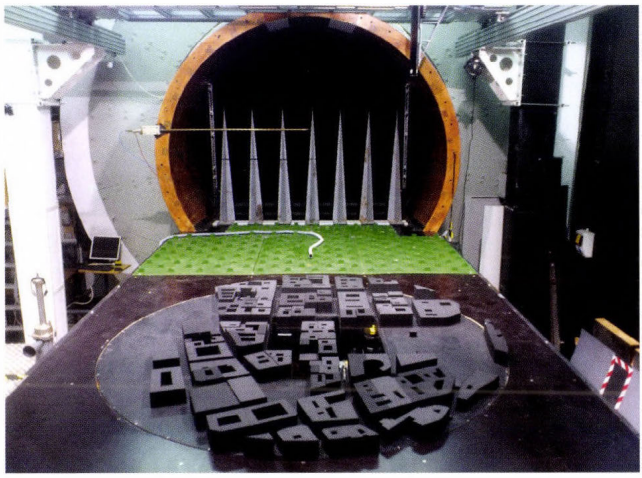

Fig. 4. The model in wind tunnel. Buildings are painted black to reduce laser reflections.

The parameters discussed herein can be calculated with the following formulas. Dimensionless mean velocity u_d and v_d in the x- and y-direction is calculated as $u_d = u/u_{ref}$ and $v_d = v/u_{ref}$, respectively. Dimensionless velocity fluctuations σ_{ud} and σ_{vd} are defined as $\sigma_{ud} = \sigma_u/u_{ref}$ and $\sigma_{vd} = \sigma_v/u_{ref}$ with velocity standard deviations σ_u and σ_v.
Dimensionless horizontal mean velocity magnitude v_{md} :

$$v_{md} = \sqrt{u_d^2 + v_d^2}. \tag{3}$$

Dimensionless turbulent kinetic energy K_d :

$$K_d = \frac{1}{2} \cdot \left(\sigma_{ud}^2 + \sigma_{vd}^2\right). \tag{4}$$

It must be noted that the calculated turbulent kinetic energy calculated from Eq. (4) differs from the real one, because the vertical velocity component w and its standard deviation σ_w could not be measured using the applied arrangement. Thus, K_d is the contribution of horizontal velocity components to turbulent kinetic energy.

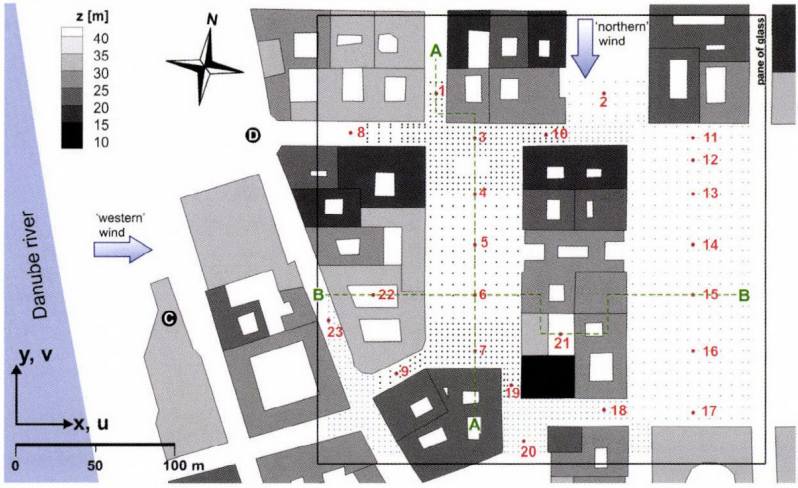

Fig. 5. Wind directions and measurement locations on the wind tunnel model. Buildings are colored by their full scale height. Red circles: vertical profile (VP) measurements; black dots: horizontal plane measurements at 0.25 *h*, 0.5 *h*, and *h* heights; blue dots: additional horizontal plane measurements at 0.5 *h* height.

2.4. Wind directions

During the flow field measurements in the model of József Nádor Square, two wind directions were investigated: approximately northern wind direction, 351.7 degree to north, and 261.7 degree to north, approximately western wind direction. The selected two wind directions mean that wind blows at 'northern' wind exactly along the long axis of the square, at which its length to height ratio *l/h* of the square is 5.3, and at 'western wind' exactly along the short axis of the square with *l/h* equaling 2.1. Wind statistics were available from three neighboring meteorological stations, which are in 2.5–10 km distance. Their averaged wind rose shows north and west-northwest as the prevailing wind directions, thus the selected wind directions are close to the prevailing ones.

3. Numerical setup

Setup of the CFD simulation carried out at 'northern' (351.7 deg) wind direction followed the best practice guideline given by *Franke et al.* (2007). The computational domain included the buildings modeled in the wind tunnel in full scale inside a 700 m diameter circle around József Nádor Square corresponding to the 2 m diameter turntable, with proper inlet, outlet, and side distances to the domain boundary. Domain size was thus 1000 × 1100 × 500 m. Grid resolution of the non-equidistant Cartesian grid applied by MISKAM varied from 4–6 m

horizontally and 1 m vertically between buildings down to 1.5 m horizontally and 0.6 m vertically around József Nádor Square near the ground, up to a total of approximately 5 million grid cells.

Regarding grid independency of the computational mesh, earlier MISKAM simulations of a simplified symmetrical street canyon geometry by *Balczó et al.* (2009) showed that it can be reached at an average of 0.5 m cell size (with refinements of 0.1 m at building leading edges). However, this resolution could not be replicated in the current complex, large-domain case with hundreds of buildings due to memory limitations of the 32 bit code. The current resolution can be seen as typical for the MISKAM model when applied in environmental impact assessment studies by agencies on a daily basis.

The predefined boundary condition types of MISKAM (see *Eichhorn,* 2011) were used: buildings represented as block outs from the Cartesian grid, on the surfaces no-slip conditions applied using wall functions, the roughness length on the surfaces set to 0.01 m. At the inlet boundaries an equilibrium logarithmic profile was generated by MISKAM automatically with initial roughness length z_0 of 0.2 m. The reference velocity was set to 3.02 m/s at h=28 m, as measured in wind tunnel.

The comparison of the CFD approaching flow profile to the profile measured in the empty wind tunnel shows certain disagreement in terms of both mean velocity and turbulence (*Fig. 6*).Turbulence underestimation in boundary layer profiles over flat terrain is a common error of K-ε turbulence closures as shown, e.g., by *Olesen et al.* (2008). It is expected, however, that the first few rows of buildings will act as boundary condition generators, and the profiles will be assimilated to each other. This will be checked later comparing CFD and wind tunnel vertical velocity profiles at locations near the square.

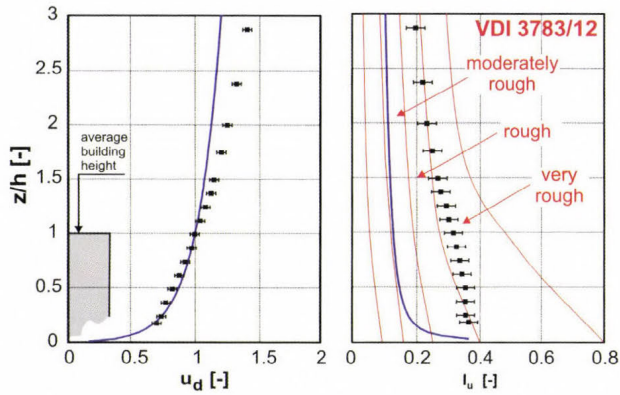

Fig. 6. Streamwise u_d dimensionless velocity and I_u turbulence intensity profiles. Simulation: continuous blue line, wind tunnel measurement: dots with error bars. h: average building height. Red lines: VDI 3783/12 limits.

4. Results and discussion

In the course of the analysis of results, first we will identify the major flow structures using vertical profile diagrams, and velocity and turbulence plots in horizontal planes in Sections 4.1 and 4.2. Although the vertical velocity component was not directly measured, some of the data allow us to draw conclusions about the vertical velocities and the three dimensional flow structures in Section 4.3. Section 4.4 shows time-resolved wind tunnel data in order to analyze unsteady phenomena in the square. In Section 4.5, the flow in the square is compared statistically with the flow in neighboring streets and to a case in which the square is replaced by a block of buildings. Additionally, we assess the influence of street vegetation in Section 4.6, and then discuss the performance of the CFD model in Section 4.7.

In the following comparison plots, turbulent kinetic energy K_d determined in simulations was always multiplied by 2/3, in order to approximate the contribution of horizontal velocity fluctuations to the turbulent kinetic energy, which was actually measured in the wind tunnel.

4.1. Analysis of vertical profiles

The 23 dimensionless vertical velocity profiles give a first insight into the flow field at the square. Our expectation is that the streamwise velocity component (v in case of northern wind direction) will follow the approaching wind profile (*Fig. 6*) above rooftop level, but around and below rooftop level it will deviate significantly.

Fig. 7 shows vertical profiles of mean velocity from both the wind tunnel and CFD simulation, streamlines from CFD and turbulent kinetic energy from the wind tunnel in the mid-plane of the square (cross section A-A in *Fig. 5*). The building located at the northern end of the square generates backflow (marked with A in *Fig. 7*). The presence of this recirculation zone is visible on profiles VP3 and VP4. The streamlines originating from one source point indicate that there is significant inflow from x direction (from the connecting street) into the core of the separation zone.

From the middle of the square (approximately 2.5 h distance, B in *Fig. 7*)), streamlines reach the bottom on the square and stagnation point develops in front of the downstream building block. Close to the ground (marked with C in *Fig. 7*), again backflow can be observed in the wind tunnel measurements, showing the presence of a *horseshoe vortex*, which is unfortunately not resolved by the CFD. Otherwise, CFD follows the measurements quite well, especially above rooftop level, proving the assumption made earlier, that the slight differences in incoming boundary conditions are assimilated, as the flow reaches the square. Near the ground, the streamwise flow velocities are overestimated by CFD.

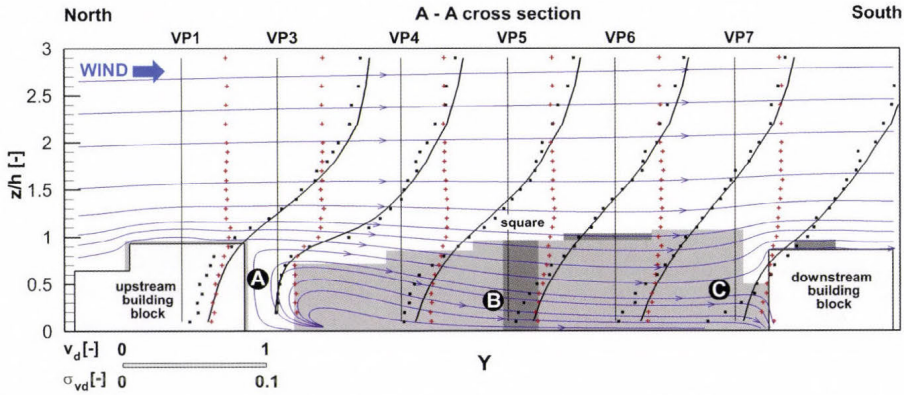

Fig. 7. Flow field at northern wind direction along the square (A –A cross section of *Fig. 5*). Black squares and continuous lines: normalized streamwise mean velocity component v_d from measurement and simulation, crosses: normalized velocity standard deviation σ_{vd} from wind tunnel measurement. Streamlines in blue are from the simulation. Note that VP1 lies in a connecting street, not on the square itself.

The flow field in a cross-section of the square at western wind is depicted in *Fig. 8* (cross section B - B of *Fig. 5*). In this direction, the square is only 2 *h* wide.

- Measurement shows strong backflow on the square up to rooftop level (VP6). Streamlines indicate a vortex with horizontal axis dominating the whole square. Similar backflow can be seen behind the downstream building block.

- Despite their small size, building inner yards have street-canyon-like horizontal vortices (VP22, VP21).

At both wind directions, turbulent kinetic energy K_d is almost constant above rooftop level (with an occasional, slight maximum at 1.2–1.7 h height), and decreases underneath rooftop level towards the ground by about one third. In building inner yards, its value goes down to less than one half.

For the generalized, quantitative description of the flow in urban squares, we compare the averaged vertical velocity profiles in the square (VP 3–7) at the two wind directions in *Fig. 9*. While above 1.5 *h*, all profiles run close together, there are differences below that level. Most remarkably, at western wind, speeds are higher than at northern wind. Nevertheless, in none of the cases it is higher than 0.5. Also, compared to the averaged profiles measured in the connecting streets (VP 1, 8, 9, 10, 18, 23), wind speed in the square is approximately the same.

CFD results, available at northern wind direction, overlap almost perfectly the wind tunnel measurement data.

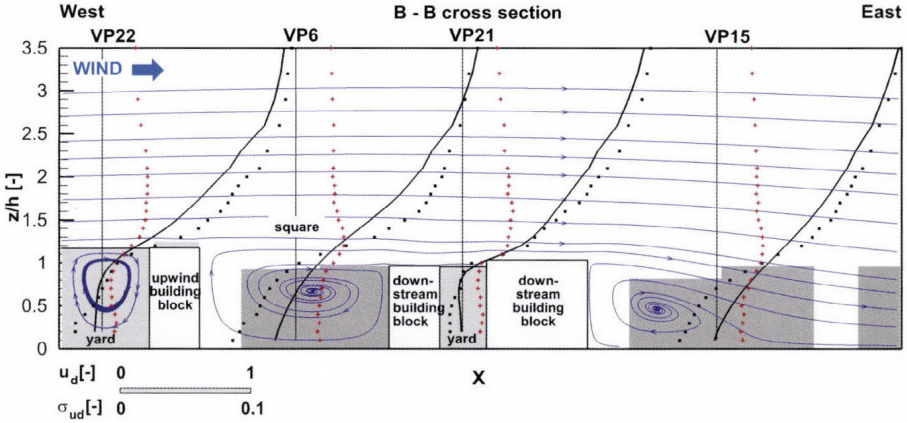

Fig. 8. Flow field at western wind direction along the square (B – B cross section of *Fig. 5*). Black squares: normalized streamwise mean velocity u_d from measurement, crosses: normalized velocity standard deviations σ_u from wind tunnel measurement. Streamlines are from simulation. Please note that profile VP21 is about 30 m off-plane towards south.

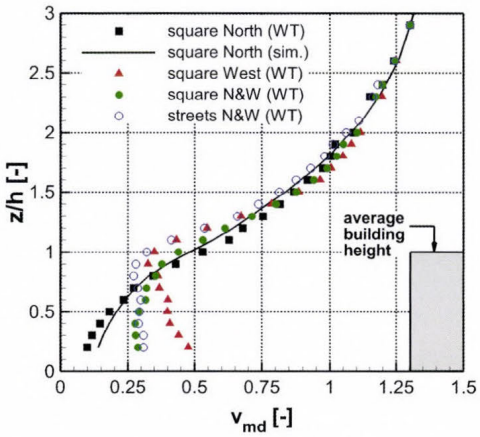

Fig. 9. Averaged vertical profiles of velocity magnitude v_{md} in the square (VP 3-7). Black: at northern, red: at western wind direction. For comparison, an overall average of vertical profiles in the connecting streets (VP 1, 8, 9, 10, 18, 23) is shown with blue.

4.2. Flow field in horizontal planes

Flow velocities were measured along three horizontal planes at 0.25 *h*, 0.5 *h,* and *h*, corresponding to 7, 14, and 28 m in full scale (20, 40, 80 mm in model scale).

Planes 1 and 3 included 568 measurement points; plane 2 consists of 1287 points (see *Fig. 5*). The positioning accuracy was less than 0.5 mm. The normalized horizontal velocity magnitude v_{md} at northern wind direction on the three horizontal planes can be seen in *Fig. 10*, with wind tunnel data in the left and CFD data in the right column. *Fig. 11* shows the normalized turbulent kinetic energy distributions in the same wind direction. *Fig. 12* shows the same variables but in western wind direction. Scalar variables are interpolated from the measurement points onto the planes using inverse-distance interpolation, and streamlines are integrated from the velocity vectors.

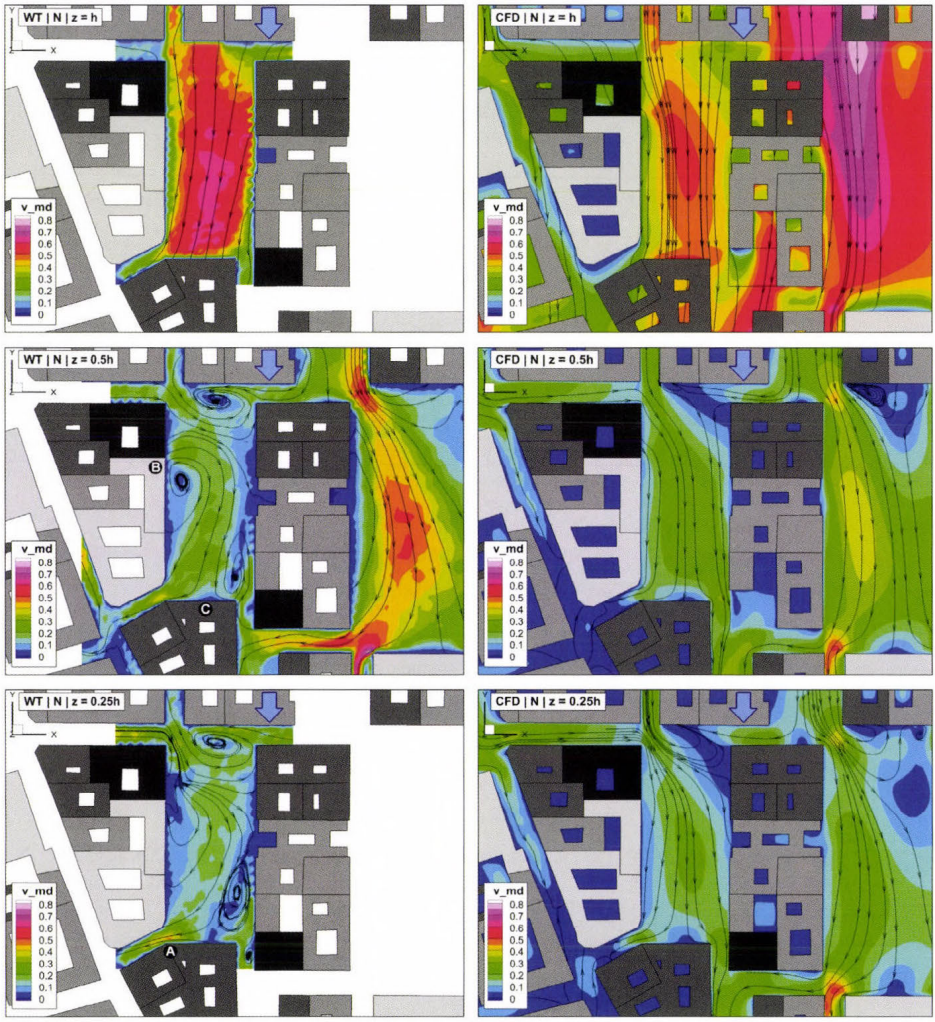

Fig. 10. Normalized horizontal velocity magnitude v_{md} distributions on three horizontal planes at northern wind direction. Left column: wind tunnel measurement; right column: CFD simulation.

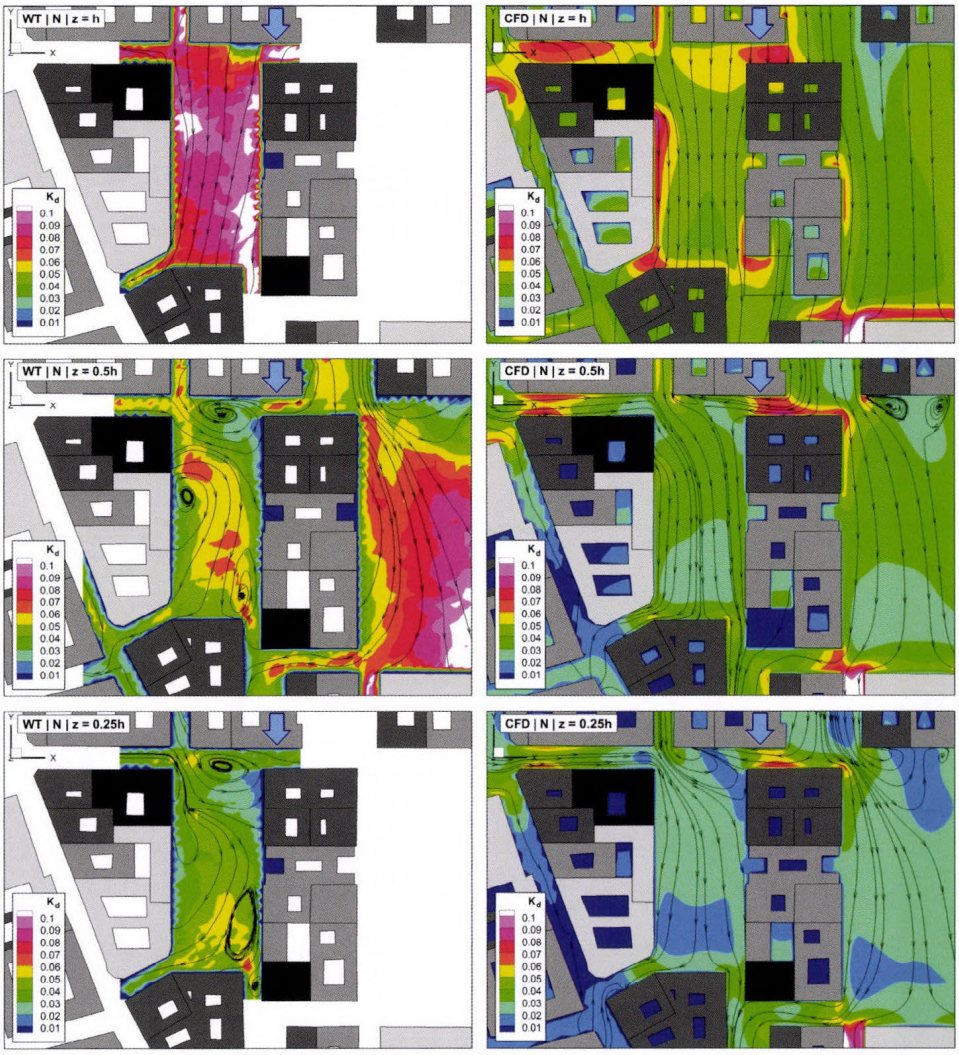

Fig. 11. Normalized turbulent kinetic energy K_d distributions on three horizontal planes at northern wind direction. Left column: wind tunnel measurement; right column: CFD simulation.

As regards the velocity fields in northern wind direction, the highest velocity values were measured at $z = h$. No backflow is observable at this height. At lower heights, mean velocity values are also lower, at 0.25 h less than 5–25% of the reference wind speed in the square itself. Top wind speed in the square is at the corner of the downstream (southern) building block, marked with A in *Fig. 10*. Outside the square, velocity magnitude of up to 0.8 can be seen at corners southward the open space in the eastern part of the measurement area.

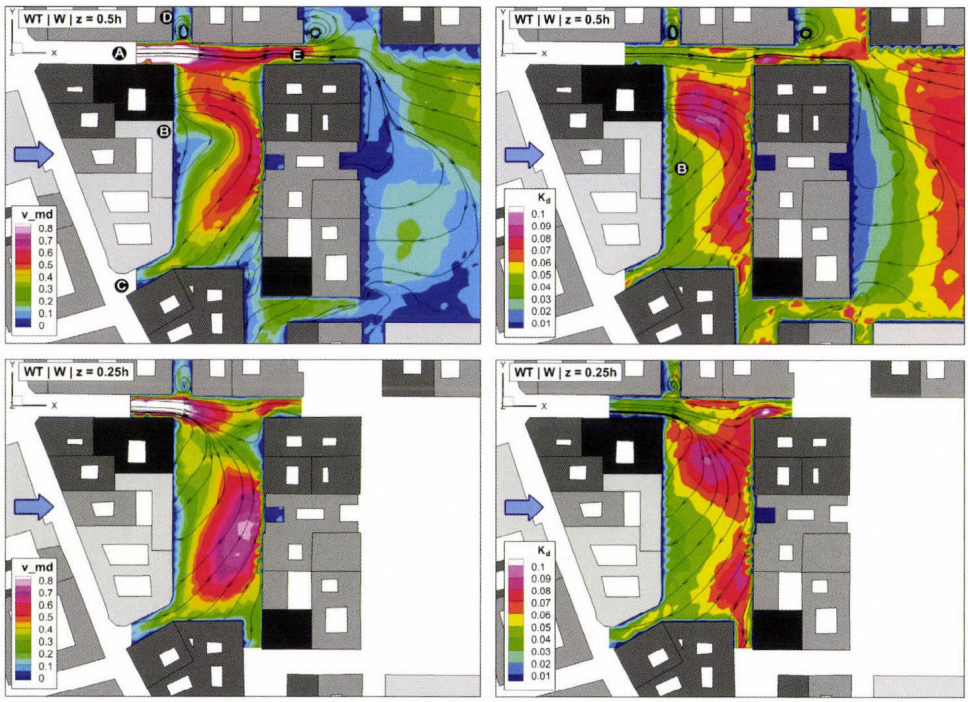

Fig. 12. Normalized horizontal velocity magnitude v_{md} (left column) and normalized turbulent kinetic energy K_d (right column) on two horizontal planes at western wind direction.

Analyzing the streamlines, it can be stated that the flow forms three major vortices in this wind direction. Their vertical extension does not reach the reference height h but is clearly present at $z = 0.25\ h$ and $z = 0.5\ h$. The northern vortex is in the separation zone of the northern block, and the middle one is obviously caused by the second, taller building of the western building block, marked with B in *Fig. 10*.

Air enters the square from the northern streets and leaves it by passing through the south-western connecting street. Interestingly, backflow is detected in the south-eastern connecting street, so the outflow is blocked here. A stagnation point can be found in the front of the southern building (marked with C in *Fig. 10*), where vertical profile VP7 suggests the presence of a horizontal vortex (B in *Fig. 7*). A significant proportion of the air, which arrives from northern connecting streets, is trapped in the first (north-eastern) vortex of the square.

CFD simulations only resolve the vortex in the north-eastern corner of the square, although in smaller size, and only visibly at 0.25 h height. While the

other vortices are suppressed, which gives a velocity field much more in line with the incident wind direction, the magnitude of velocity is about the same as in the measurement.

The average level of turbulent kinetic energy K_d (*Fig. 11*) is the simulated about 2/3 of that measured in the wind tunnel. It increases with the height and has a maximum at the average building height h. Values of the turbulent kinetic energy are usually smaller in the vicinity of the walls. This agrees well with the expectations, because both the mean velocity and the standard deviation values are lower near the walls.

Due to the stagnation point anomaly (*Kato* and *Launder,* 1993), CFD results for K_d predict peaks near building leading edges, which are not present in the measurement.

In western wind direction, flow velocities were measured along two horizontal planes at 0.25 h and 0.5 h corresponding to 7 and 14 m in full scale (20 and 40 mm in model scale). Plane 1 covers just the square and connecting streets; plane 2 covers the whole area. The velocity and turbulent kinetic energy distributions on the two horizontal planes can be seen in *Fig. 12*.

In terms of the velocity fields on the horizontal planes, it can be stated that the measured velocity values at 0.5 h are not significantly larger than the values at 0.25 h. Moreover, in the middle and eastern part of the square velocity values at 0.25 h are larger than the values at 0.5 h. The highest velocities were measured in the connecting street at the NW corner of the square at both heights; mean velocity values approximate the reference wind speed in the western part of the investigated section of the street, indicated by A in *Fig. 12*. The streamlines show that:

- The street marked by D is blocked entirely by a corner vortex.
- Most of the air passes through the square flowing from the street marked by A towards the street marked by E in *Fig. 12*.
- A smaller portion of it enters the separation bubble which is formed behind the western building block (marked by B in *Fig. 12*). However, this is modified by the high velocity inflow at the NW corner to a helical vortex, which moves air towards the southern part of the square, and pushes air through the southern connecting streets even opposite to the incident wind direction. The high velocity inflow is caused by the direct, unobstructed inflow from the river Danube (mark D in *Fig. 5*).

Thus, despite the wind coming from the west, there is a significant north to south convection in the square. It is remarkable that the flow field is very similar to that in a street canyon at slanted wind direction (*Czáder et al.,* 2009) with a huge street canyon vortex superposed to a velocity component along the street canyon.

4.3. Three-dimensionality of the flow

Because of the vertical arrangement of the LDV probe under floor, we were not able to measure the vertical velocity component w directly. However, the measured mean horizontal flow field ($v_{hor\,d}$) let us calculate the vertical velocity gradient based on the continuity equation:

$$-\frac{\partial w_d}{\partial z} = \left(\frac{\partial u_d}{\partial x} + \frac{\partial v_d}{\partial y}\right) = div(\underline{v}_{hor\,d}). \tag{5}$$

On the horizontal ground surface, obviously w must be 0. At a small height, slightly above the ground surface, vertical velocity, if there is any, must decrease towards the surface. Thus, we can distinguish three cases for the w velocity component in horizontal planes near the ground:

a. the flow is horizontal ($w = 0$), thus $\partial w/\partial z = 0$ and $\mathrm{div}(v_{\mathrm{hor\,d}}) = 0$,

b. vertical inflow occurs ($w < 0$), flow towards the ground must be decelerated ($\partial w/\partial z < 0$), thus the flow field in horizontal plane will diverge ($\mathrm{div}(v_{\mathrm{hor\,d}}) > 0$),

c. vertical outflow occurs ($w > 0$), flow accelerates upwards ($\partial w/\partial z > 0$), and the horizontal flow field will converge ($\mathrm{div}(v_{\mathrm{hor\,d}}) < 0$).

In conclusion, positive values of the horizontal divergence near the ground are related to updrafts, while negative values indicate downdrafts. The relationship is demonstrated at 0.25 h height in plot a and b of *Fig. 13* using CFD results at northern wind direction. Divergence calculated from wind tunnel data in northern and western wind direction is shown in plot c and d of *Fig. 13*. The results are obviously subject of considerable noise; however, the major spots of vertical air movements are clearly recognizable.

- In case of northern wind direction, *updrafts in the wake* of the northern (upstream) building block and at building walls of the north-eastern corner can be seen, as well as a downdraft in the northern centre of the square caused by the inflow at the northeast corner.
- In case of western wind direction, the magnitude of divergence is significantly larger and shows a *single, massive helical vortex* with horizontal axis dominating the square, causing updrafts on the western and downdrafts on the eastern side.
- Up- and downdrafts can be seen in many of the connecting streets in both wind directions. Considering the direction of streamlines in the streets, these indicate *weak helical vortices* (street canyon vortices with some advection along the street axis).

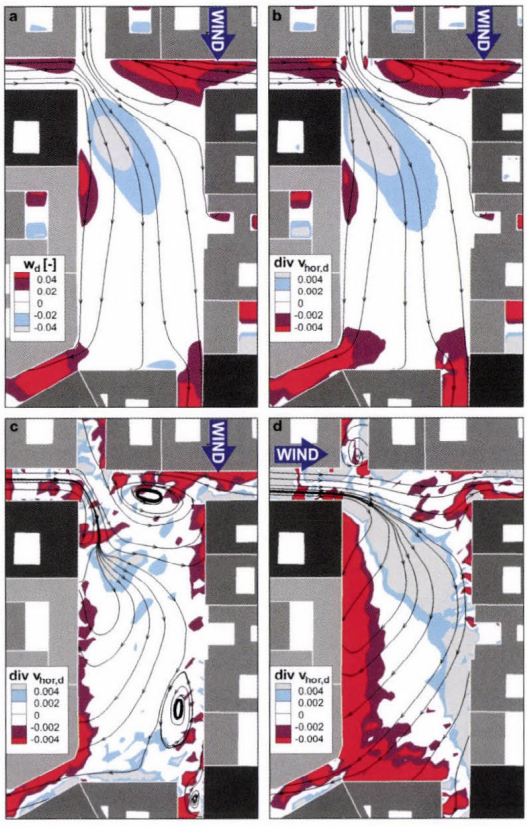

Fig. 13. Vertical air velocity and horizontal divergence in the square at 0.25 h height. Reddish colors: updraft, light colors: downdrafts. Values close to 0 are blanked. From left to right: (a) CFD simulation: normalized vertical velocity in northern wind direction; (b) CFD simulation: div($v_{hor\ d}$) in northern wind direction; (c) wind tunnel measurement: div($v_{hor\ d}$) in northern wind direction, (d) wind tunnel measurement: div($v_{hor\ d}$) in western wind direction.

4.4. Analysis wind speed and direction fluctuations

The time-resolved LDV data captured simultaneously for both horizontal wind directions contain information about turbulence anisotropy and spectral properties. Up to this point, from the turbulent quantities, only turbulent kinetic energy was analyzed.

For a more detailed analysis, simultaneous u and v time series were captured at a horizontal plane at 0.5 h height at several measurement locations, and the occurrence frequency of the instantaneous horizontal wind vector $\underline{v}_{i,d}$ at a certain location was visualized by wind roses (polar area diagrams). Thirty one selected wind roses are shown in *Fig. 14*, colored by

the instantaneous velocity magnitude. Also, streamlines colored by the average horizontal velocity magnitude v_{md} are shown.

- Each illustrated wind rose is placed at the location of the given measurement point.
- The roses are divided into 10-degree spokes representing the probability of 10-degree wind direction sectors.
- Each spoke is subdivided into color-coded bands that show velocity ranges.

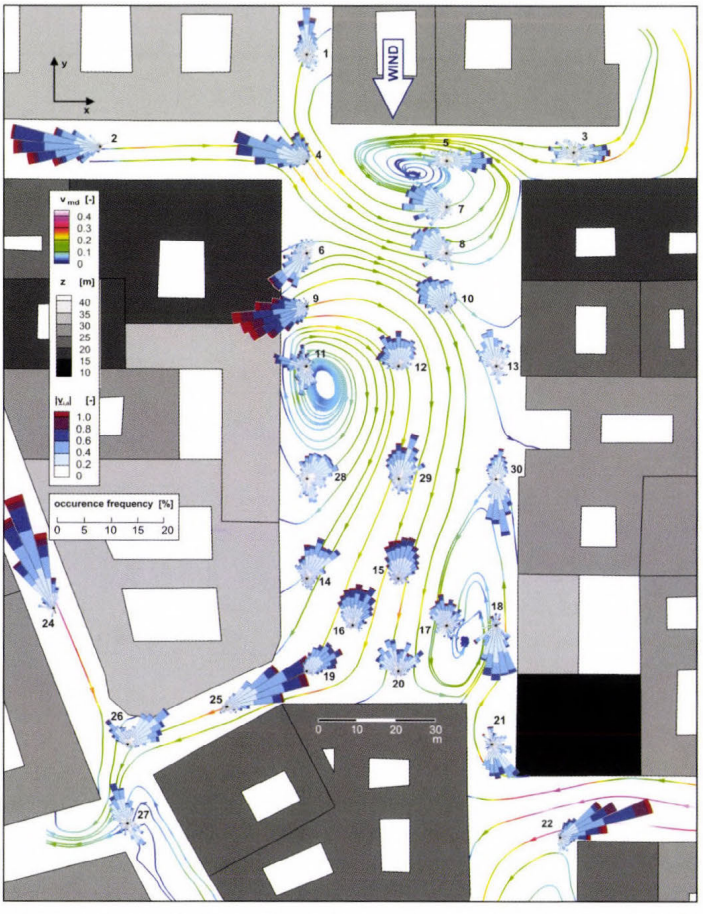

Fig. 14. Flow field and wind roses in the investigated area in northern wind direction at 0.5 h height. Streamlines are colored by normalized average velocity magnitude v_{md}, buildings by their full scale height, and wind roses by the magnitude of the instantaneous normalized wind vectors $\underline{v}_{i,d}$. Note that the two velocity scales are different. The wind roses show the occurrence frequency of 10-deg wind direction sectors.

It is important to point out that as opposed to the usual application of wind roses – representing annual wind statistics –, the current wind roses show the statistics of wind speed and direction at a single incident wind direction. The wind roses presented in *Fig. 14* can be organized into different groups based on their shape:

1. Wind roses with a single dominant wind direction and small deviations can be found in streets with one-directional flow (WR2, 24) channeled along the streets' main axis. Backflow (90–270 degree to the main wind direction) is negligible. While the average velocity magnitude is 0.3–0.4, wind velocities of larger than 1 (wind gusts) have also a significant probability.
2. Fan-tail shaped wind roses appear in several locations on the square, but not in the connecting streets (WR 7, 8, 10, 12, 14–16, 19, 20, 31). Obviously, far from walls which restrict perpendicular movements, velocities can fluctuate in all directions. Deviations of up to +/–90 degree from the main wind direction can occur; also, a low percentage of backflow can be seen.
3. Wind roses with more than one peak can be observed in streets (WR 3, 21, 26, 27). The double peaks mean that at a given wind direction, flow is coming once from one end of the street, once from the other end. WR 26, located in an intersection, shows peaks 90 degree to each other, which can be explained by the angle of the connecting streets.
4. Wind roses with more than one peak can be seen also near the core of vortices of the mean wind field (WR 5, 11, 21). This can be explained by the slight movement of the vortex core, meaning that the measurement location is once on one side, and once on the other side of the vortex core, thus flow direction is reversed.
5. Finally, points on the boundary of a vortex of the mean flow can have multiple peaks, again explained by the slight movement of the cores as in WR 30. Here, instantaneous velocity magnitude reaches 0.6, while average velocity is just 0.05.

Regarding the temporal sequence of velocity fluctuations, double peaks in the histogram of velocity time series recorded in location types 4 and 5 prove the periodic switching between wind directions. *Fig. 15* shows the continuous velocity histograms of the v_d stream-wise velocity component, as captured by the LDV system. The wind rose WR 15, classified as type 2 shows a more Gaussian-like distribution; in contrast to this, the type 5 wind rose WR 30 shows double peaks indicating periodic or mode-locking flow switching between a northern (positive v_d) and a southern (negative v_d) flow state. The consequences of such flow switching on pollutant dispersion are significant, see, e.g., the

observations of *Klein et al.* (2011) made at smoke plume dispersion visualisations in urban environment.

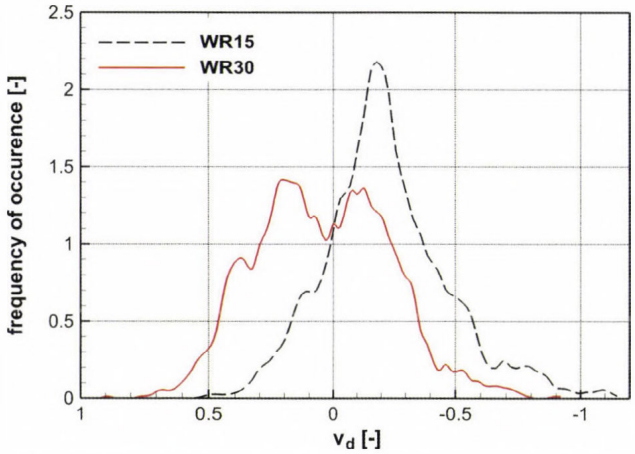

Fig. 15. Comparison of type 2 (WR 15) and type 5 (WR 30) wind velocity distributions (northern wind direction).

4.5. CFD results and their validation with the experimental data

The secondary objective of this paper is to show the applicability of a CFD RANS model, predominantly used in the regulatory and consulting field, in a complex urban environment. The model was able to resolve some, but not all of the flow structures dominating the square in question. The surface flow direction in the streets connected to the square is well predicted in four from five cases (see *Fig. 10*). Velocity magnitudes are qualitatively well predicted. More problems were experienced with turbulence: the prediction of K_d is often wrong, and does not give the model any information on the anisotropic and occasionally mode switching behavior of the flow discovered in Section 4.4, which has obvious consequences for dispersion phenomena, too.

In *Table 1,* hit rates of the CFD simulation are summarized. Hit rate q is defined as the percentage of those simulation data (prediction) which are inside an allowed range of the measurement (observation):

$$q = \frac{N}{n} = \frac{1}{n}\sum_{i=1}^{n} N_i \quad with \quad N_i = \begin{cases} 1 \;\; for \left|\frac{P_i - O_i}{O_i}\right| \le D \; or \; |P_i - O_i| \le W \\ 0 \;\; else \end{cases}, \tag{7}$$

where P_i are the prediction (simulation) data, O_i are the observation (measurement) data, D is the allowed relative deviation, e.g. 25%, W – allowed absolute deviation or threshold, usually the measurement uncertainty of the observation.

Table 1. Hit rates calculated for the MISKAM simulations. Note that the velocity component parallel to the approach flow is v in northern wind and u in western wind direction

	Number of points	**Hit rate [%] for variable:**			
		u_d	v_d	v_{md}	K_d
Allowed relative dev. D [-]		0.25			
Allowed absolute dev. W [-]		0.026	0.026	0.03	0.006
Vertical profiles	601	36	76	74	9
Horizontal planes	1855	28	29	33	32

Hit rate calculations were performed for all vertical profiles and all horizontal planes separately, all together for 2456 measurement points, and for different variables. As it could be seen earlier in Section 4.1, vertical profiles of streamwise flow velocity above rooftop level agreed the best with the measurement (*Figs. 7* and *8*). Thus, their hit rates are accordingly high. Flow in horizontal planes is much more difficult to predict, and hit rates are generally lower on horizontal planes. Lateral flow velocity and turbulent kinetic energy were less well predicted than the streamwise velocity, and have consequently worse hit rates.

It must be noted that hit rates for calculations made by the same model, but for different test cases, might be significantly different: hit rate is also a measure for the difficulty of the test case, and not only for the performance of the model.

4.6. Comparison with fully built-up area

In the following, the CFD model is applied to answer questions regarding different urban planning scenarios. As mentioned already in the introduction, creating new urban squares by removal of defunct building blocks is often part of urban redevelopment programmes. The question is what the consequences of such a transformation on the ventilation of the whole area are. To create a reference case representing the situation before such a transformation, a numerical model was set up, in which the square was replaced by a building block consisting of four buildings of various height (23, 32, 26, and 29 m) as shown in *Fig. 16b*. CFD simulation results obtained with this geometry of a fully built-up area can then be compared with the ones with the existing square that represents the situation after the hypothetical redevelopment. Comparison is limited to the prevailing northern wind direction.

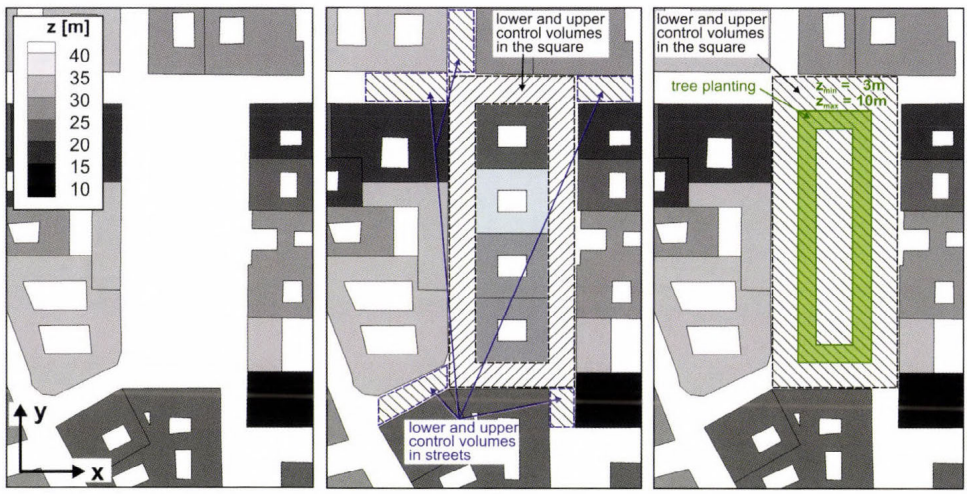

Fig. 16. (a) actual geometry of the square, (b) built-up area instead of the square representing a reference case *before* a hypothetical urban redevelopment programme; right: square with tree planting. Hatched areas with dashed borders show the control volumes used for averaging.

To perform a statistical analysis of the simulation results obtained, v_{md} and K_d are averaged for the control volume depicted in *Fig 16b* (hatched areas). The control volume consists of four parts: lower volumes from 0 to 0.5 *h* and upper volumes from 0.5 *h* to *h* height on the square itself and in the connecting streets, respectively.

In *Table 2,* the averaged variables are shown for the two cases and then the percent change Δv_{md} *[%]=* $[v_{md}$ *(with square) -* v_{md} *(built-up area)]* / v_{md} *(built-up area)* is listed. Percent change of turbulent kinetic energy ΔK_d [%] is similarly defined.

The data in *Table 2* suggest that average wind speed on the square itself is overall increasing, but only by 2% when establishing a square compared with a fully built-in area. Such slight change consists of a significant increase of v_{md} above 0.5 *h* and a decrease of less extent below it. The average wind speed in the connecting streets increases dramatically upon removal of the central building block. At low level, below 0.5 *h*, the change is more than 50%. The comparison of turbulence from CFD results is in light of the discrepancies observed previously and is not fully to be trusted, nevertheless K_d in connecting streets is increasing, and on the square itself decreasing.

Table 2. Changes of average velocity magnitude and turbulent kinetic energy in the square and in connecting streets when comparing a built-up area and area with square. Δv_{md} [%]= [v_{md} (with square) – v_{md} (built-up area)] / v_{md} (built-up area), ΔK_d [%] similarly defined

	v_{md} **built-up area**	v_{md} **area with square**	Δv_{md} **[%]**	K_d **built-up area**	**area with square**	ΔK_d **[%]**
in the square						
below 0.5*h*	0.164	0.138	**–16%**	0.049	0.032	–35%
above 0.5*h*	0.251	0.285	**14%**	0.084	0.063	–25%
average from 0 to *h*	0.207	0.211	**2%**	0.066	0.047	–29%
in connecting streets						
below 0.5*h*	0.108	0.166	**54%**	0.036	0.047	30%
above 0.5*h*	0.145	0.184	**27%**	0.065	0.076	17%
average from 0 to *h*	0.126	0.175	**39%**	0.051	0.062	21%

4.7. Influence of vegetation

The increase of urban vegetation is seen undoubtedly as a positive measure to improve sustainability and human comfort in today's urban architecture. As in an urban square the flow is much less obstructed by buildings than in street canyons, thus we expect a remarkable influence of vegetation on flow velocities.

In the simplified model investigated in wind tunnel, the influence of vegetation has been neglected, although a proper method to model vegetation in wind tunnel tests has already been developed by *Gromke* (2011).

The CFD model MISKAM allows the modeling of vegetation using a porosity approach, as described by *Eichhorn* (2011) and validated by wind tunnel experiments by *Balczó et al.* (2009) and *Czáder et al.* (2009). The vegetation defined as a porous medium exerts an influence on the fluid flow by its viscous and form drag (*Gross,* 1993). The total drag force, e.g., in x coordinate direction, is described by the following formula:

$$F_{veg,x} = \rho c_{d0} b u |\underline{v}| \ , \tag{6}$$

where ρ is the fluid density [kg/m^3]; c_{d0} is the leaf drag coefficient [-]; b is the leaf area density (LAD), the projected leaf surface area per unit volume [m^2/m^3]. The obtained drag force is embedded in the RANS equation as a negative

source. Furthermore, the effects of vegetation on the turbulence are also taken into account by extending the K-ε equations with new terms.

The tree planting's shape at the square (*Fig. 16*, right) is simplified: we study a homogeneous tree crown region of rectangular shape from 3 m to 10 m height and 8 m width. The centre of the region is empty, imitating a usual urban park with grass area in the middle. Leaf area density (LAD) throughout the crown region is assumed 1 m^2/m^3 based on the data of *Larcher* (2001), which is a typical value for urban tree plantings.

Table 3 summarizes the obtained results with tree planting and the comparison with the treeless case. Similarly to Section 4.6, v_{md} and K_d are averaged for two control volumes below and above 0.5 h. However, in this case the whole square is covered by the control volume (hatched area in *Fig. 16*, right). Decrease of velocity magnitude v_{md} by 21% below 0.5 h can be observed. Above 0.5 h the influence is negligible. The same can be said as regards turbulent kinetic energy, the value in the square is decreased by 27% below 0.5 h height. The change of K_d is also detectable above 0.5 h (–5%).

Table 3. Influence of tree plantings as determined by CFD simulations

	v_{md} **without trees**	v_{md} **with trees**	Δv_{md} [%]	K_d **without trees**	**with trees**	ΔK [%]
below 0.5 h	0.138	0.108	–21%	0.032	0.023	–27%
above 0.5 h	0.285	0.281	–1%	0.063	0.059	–5%
average from 0 to h	0.211	0.195	–8%	0.047	0.041	–13%

Looking at flow field plots of the CFD simulation with tree planting (not shown here), some further observations could be made: velocity decreases up to 30% inside the tree crowns. In some locations outside the crown region, the flow accelerated slightly, due to displacement effect of the trees. K_d is decreasing not only in the control volume, but also in the connecting streets, up to 30 m distance from the square. These preliminary findings fit well the observations made by *Gromke* and *Ruck* (2009) and *Balczó et al.* (2009) about the influence of vegetation in a street canyon, although a more detailed analysis might reveal further details.

5. Conclusions

The urban square investigated, although slightly simplified in geometry, can be seen as a test case of high complexity level, similarly to real urban areas. Despite this fact, the results allow more generalized conclusions to be made, which can be valid for squares of similar size:

- Average pedestrian level wind speed on the square, while significantly smaller than the above rooftop wind speed, is varying with wind direction strongly between normalized values of 0.1 and 0.5. Wind gusts can be higher than the average wind speed at rooftop level on a few locations.
- The exact location of high-speed spots in the square near the ground depends on wind direction, but is usually near building corners and at the mouth of connecting streets.
- The square influences flow in the connecting streets as well. Flow is induced in these by the developing flow structures in the square even in perpendicular or opposite direction to the approach wind. CFD results suggest that wind speed can increase up to 50% in the connecting street compared to a case in which no square is present.
- In both investigated wind directions, distinct and complex flow fields were observed, as a result of superposition of flow advection, corner vortices, separation bubbles, street canyon, and horseshoe vortices. These average flow fields are supposed to have major influence on wind comfort of pedestrians and the dispersion of pollutants, the latter of which is an objective of future studies on the square.
- For the study of flow unsteadiness, the representation of two-dimensional time-resolved data in the form of wind roses (polar area diagrams) placed over the average flow field proved to be a useful tool. Wind roses could be classified according to their shape to identify the spots, where turbulence is non-isotropic and/or flow direction is alternating.
- Tree plantings in the square are decreasing wind velocity and turbulence in the square affecting mainly the lower half of the square, where the tree crowns are located. However, turbulence changes have further reaching influence in the upper half of the square and in connecting streets, too.

We applied the MISKAM microscale flow model to the case geometry. The estimation of the measured flow field is reasonable, when average velocity magnitude comes into question. Despite the large difference in the incoming turbulence, K_d is only underpredicted by about one third on average.
However, there are certain non-negligible flaws of the simulation, like smaller or fully suppressed vortices in the mean flow field on the square. These errors can

be traced back to the commonly known turbulent kinetic energy overprediction of K-ε type closures in stagnation points.
The flow intermittency effects not resolved by MISKAM are originated from the steady RANS approach used by this class of models. As, e.g., *Letzel et al.* (2008), *Nakayama et al.* (2014) have shown, large eddy simulation (LES) applied in an urban environment can give superior results in this regard, although at the cost of much higher computational time and power requirements, which are mostly unavailable at the moment among the users of CFD models in the regulatory / urban planning field.

Recommendations for urban planning

The implications of our observations on urban planning are manifold. The flow structures in an urban square result from incoming and outgoing flow through the connecting streets. As observed, even a single gap in a building block or a lower building can modify the flow field significantly in the square. Thus, measures of local governments like permission to raise buildings to uniform height around the square will influence the flow field in the vicinity.

When establishing a new urban square in a fully built-up area, an overall increase of wind speed in neighboring streets can be expected, which will increase ventilation of the area. While this is an advantage, the high speed spots observed near the corners of connecting streets in the square might be less welcome and can cause human discomfort. However, as vegetation can decrease wind speeds locally, planting of trees on proper locations can help avoiding too high local wind speeds.

An urban (re)development project, such as establishing a new square, or the building or replacement of buildings in an urban neighborhood can be optimized using CFD tools like the MISKAM model used in this paper. One can find the optimal building configuration or the best tree planting patterns, hence the outcome of such a project can be improved in respect of quality of living.

Acknowledgements: The scientific work presented in this article was supported by the projects K108936 "Flow and dispersion phenomena in urban environment" of the Hungarian Scientific Research Fund and the New Széchenyi Plan project TÁMOP-4.2.1/B-09/1/KMR-2010-0002 "Development of quality-oriented and harmonized R+D+I strategy and functional model at BME".

LIST OF SYMBOLS

Name	unit	definition
b	m^2/m^3	leaf area density (LAD): projected leaf surface area per unit volume
c_{d0}	-	leaf drag coefficient
d_0	m	displacement height
$F_{veg,x}$	N/m^3	drag force from vegetation in x coordinate direction
h	m	average building height
I_u , I_v , I_w	-	turbulence intensity in x, y, and z direction
K	m^2/s^2	turbulent kinetic energy
K_d	-	dimensionless turbulent kinetic energy
$L_{u,x}$	m	integral length scale of turbulence in x direction
q	%	hit rate
u, v, w	m/s	velocity components in x, y, and z direction
$\bar{u}$, $\bar{v}$, $\bar{w}$	m/s	averaged velocity components in x, y, and z direction
u_{ref}	m/s	reference wind speed
u_d, v_d, w_d	-	dimensionless wind velocity x, y, and z direction
$\underline{v}$	m/s	flow velocity vector
$v_{hor\,d}$	-	dimensionless velocity vector in horizontal (xy) plane
v_{md}	-	dimensionless velocity magnitude in horizontal direction
z_{ref}	m	reference height (height of the modelled boundary layer)
Δv_{md}	-	difference of dimensionless velocity magnitude between two cases
Δv_{md} [%]	-	percent difference of dimensionless velocity magnitude between two cases
ρ	kg/m^3	fluid density
σ_u, σ_v, σ_w	m/s	standard deviation of velocity in x, y, and z direction
σ_{ud}, σ_{vd}, σ_{wd}	-	dimensionless standard deviation of velocity in x, y, and z direction

References

Ahmad, K., Khare, M., and *Chaudhry, K.,* 2005: Wind tunnel simulation studies on dispersion at urban street canyons and intersections - a review. *J. Wind Engin. Indust. Aerodynam. 93*, 697–717.

Balczó, M., Balogh, M., Goricsán, I., Nagel, T., Suda, J. M., and *Lajos, T.,* 2011: Air quality around motorway tunnels in complex terrain – Computational Fluid Dynamics modeling and comparison to wind tunnel data. *Időjárás 115,* 179–204.

Balczó, M. and *Eichhorn, J.,* 2009: Refined MISKAM simulations of the Mock Urban Setting Test. Proceedings of the XXIII. MicroCAD International Scientific Conference, Miskolc, Hungary, 19–20 March 2009, 7–12.

Balczó, M., Gromke, C., and *Ruck, B.*, 2009: Numerical modeling of flow and pollutant dispersion in street canyons with tree planting. *Meteorol. Z.18,* 197–206.

Balczó, M. and *Lajos, T.,* 2012: Active reduction of air pollutant concentrations at an urban square. Proceedings of the 8th International Conference on Urban Climate (ICUC 8), Dublin, Ireland, August 6-10, 2012.

Bastigkeit, I., 2011: Erzeugung von Validierungsdaten für wirbelauflösende mikroskalige Strömungs- und Ausbreitungsmodelle. PhD thesis, University of Hamburg.

Belalcazar, L.C., Clappier, A., Blond, N., Flassak, T., and *Eichhorn, J.,* 2010: An evaluation to the estimation of road traffic emission factors from tracer studies. *Atmos. Environ. 44,* 3814–3822

Belcher, S.E., Coceal, O., Hunt, J.C.R., Carruthers, D.J., and *Robins, A.G.,* 2013: Atmospheric Dispersion Modelling Liaison Committee Report: ADMLC-R7 Annex B: A review of urban dispersion modelling

Benson, J., Ziehn, T., Dixon, N.S., and *Tomlin, A.S.,* 2007: Global sensitivity analysis of a 3D street canyon model - Part II: Application and physical insight using sensitivity analysis, *Atmos.Environ.42,* 1874–1891.

Blocken B. ,2014: 50 years of computational wind engineering: past, present and future. *Journal of Wind Engin. Indust. Aerodynam. 129,* 69–102.

Britter, R.E. and *Hanna, S.R.,* 2003: Flow and dispersion in urban areas. *Ann. Rev. Fluid Mechanics 35,* 469–496.

Czáder, K., Balczó, M., and *Eichhorn, J.,* 2009: Modelling of flow and dispersion in a street canyon with vegetation by means of numerical simulation. Proceedings of the XXIII. MicroCAD International Scientific Conference, Miskolc, Hungary, 19-20 March 2009, 47–52.

Donnelly, R.P., Lyons, T.J., and *Flassak, T.,* 2009: Evaluation of results of a numerical simulation of dispersion in an idealised urban area for emergency response modelling. *Atmos. Environ.43,* 4416–4423.

Eichhorn, J., 2011: MISKAM - Manual for version 6, Giese-Eichorn, Wackernheim, Germany

Eichhorn, J. and *Kniffka, A.,* 2010: The numerical flow model MISKAM: State of development and evaluation of the basic version. *Meteorol. Z. 19,* 81–90.

Eichhorn, J., Schrodin, R., and *Zdunkowski, W.,* 1988: Three-dimensional numerical simulations of the urban climate. *Beit. Physik Atmosphäre 61,* 187–203.

ESDU, 1972: Characteristics of wind speed in the lower layers of the atmosphere near the ground: strong winds (neutral atmosphere). Engineering Sciences Data Unit 72026

ESDU, 2001: Characteristics of atmospheric turbulence near the ground Part II: single point data for strong winds (neutral atmosphere). Engineering Sciences Data Unit 85020

Flassak, T., Janicke, U., and *Ketzel, M.,* 2010: Comparison of ground-level centreline concentrations calculated with the models OML, AERMOD/PRIME, MISKAM and AUSTAL2000 against the Thompson wind tunnel data set for simple stack-building configurations. 13th International Conference on Harmonisation within Atmospheric Dispersion Modelling for Regulatory Purposes, Paris, 1.-4. June 2010. Paper No. 163.

Franke, J., Hellsten, A., Schlünzen, H., and *Carissimo, B.,* 2007: Best practice guideline for the CFD simulation of flows in the urban environment. COST Office, Brussel

Gadilhe, A., Janvier, L., and *Barnaud, G.,* 1993: Numerical and experimental modelling of the three-dimensional turbulent wind flow through an urban square. *J. Wind Engin. Industrial Aerodynam. 46–47,* 755–763.

Goricsán, I., Balczó, M., Balogh, M., Czáder, K., Rákai, A., and *Tonkó, Cs.,* 2011: Simulation of flow in an idealised city using various CFD codes. *Int. J. Environ. Poll. 44,* 359–367.

Gromke, C. and *Ruck, B.,* 2005: Die Simulation atmosphärischer Grenzschichten in Windkanälen. Proc. 13. GALA Fachtagung: "Lasermethoden in der Strömungsmesstechnik", 6 – 8 September 2005, BTU Cottbus.

Gromke, C. and *Ruck, B.,* 2009: On the impact of trees on dispersion processes of traffic emissions in street canyons. *Bound-Lay. Meteorol. 131,* 19–34.

Gromke, C., 2011: A vegetation modeling concept for Building and Environmental Aerodynamics wind tunnel tests and its application in pollutant dispersion studies, *Environ. Pollut. 159,* 2094–2099.

Gross, G., 1993: Numerical Simulation of Canopy Flows. Springer Verlag.

Hertwig, D., Efthimiou, G.C., Bartzis, J.G., and *Leitl, B.,* 2012: CFD-RANS model validation of turbulent flow in a semi-idealized urban canopy. *J.Wind Engin. Indust. Aerodynam. 111,* 61–72.

Kato, M. and *Launder, B.,* 1993: The modelling of turbulent flow around stationary and vibrating square cylinders. Ninth Symposium on Turbulent Shear Flows, Kyoto, Japan, August 1993, 10.4.1–10.4.6.

Klein, P., Leitl, B., and *Schatzmann, M.,* 2011: Concentration fluctuations in a downtown urban area. Part II: analysis of Joint Urban 2003 wind-tunnel measurements. *Environ. Fluid Mech. 11,* 43–60.

Kozmar, H., 2011: Wind-tunnel simulations of the suburban ABL and comparison with international standards. *Wind Structures 14,* 15–34

Larcher, W., 2001: Ökophysiologie der Pflanzen. Stuttgart, Verlag Eugen Ulmer.

Letzel, M.O., Krane, M., and *Raasch, S.,* 2008: High resolution urban large-eddy simulation studies from street canyon to neighbourhood scale. *Atmos. Environ. 42,* 8770–8784.

Letzel, M.O., Flassak, T., and *Angel D.,* 2012: Verbesserung der AUSTAL2000-Ergebnisse durch Strömungs- und Turbulenzübernahme aus MISKAM. Gefahrstoffe Reinhaltung der Luft 72, Juli/August 2012, 329–333.

Leuzzi, G., Balczó, M., Amicarelli, A., Monti, P., Eichhorn, J., and *Thomson, D.J.,* 2010: Street canyon concentration estimation coupling the RANS model MISKAM and the micromixing Lagrangian model LAGFLUM. Proceedings of the 13th International Conference on Harmonization within Atmospheric Dispersion Modelling for Regulatory Purposes (HARMO13), Paris, France, June 1-4, 2010. 821–825.

Nakayama, H., Leitl, B., Harms, F., and *Nagai, H.,* 2014: Development of local-scale high-resolution atmospheric dispersion model using large-eddy simulation. Part 4: turbulent flows and plume dispersion in an actual urban area. *J. Nuclear Sci. Technol. 51,* 626–638

Olesen, H., Baklanov, A., Bartzis, J., Barmpas, F., Berkowicz, R., Brzozowski, R., Buccolieri, R., Carissimo, B., Costa, A., Di Sabatino, S., Efthimiou, G., Franke, J., Goricsán, I., Hellsten, A., Ketzel, M., Leitl, B., Nuterman, R., Polreich, E., and *Tavares, R.,* 2008: The MUST model evaluation exercise: Patterns in model performance. *Croatian Meteorolog. J. 43,* 403–408.

Olesen, H.R., Berkowicz, R.L, Ketzel, M., and *Løfstrøm, P.,* 2009: Validation of OML, AERMOD/PRIME and MISKAM using the Thompson wind tunnel data set for simple stack-building configurations. *Bound-Lay. Meteorol. 131,* 73–83.

Parra, M., Santiago, J., Martín, F., Martilli, A., and *Santamaría, J.,* 2010: A methodology to urban air quality assessment during large time periods of winter using computational fluid dynamic models. *Atmos. Environ. 44,* 2089–2097.

Rákai, A., and *Kristóf, G.,* 2013: Microscale Obstacle Resolving Air Quality model evaluation with the Michelstadt case. *The Scientific World Journal 2013,* Article ID 78174

Schatzmann, M., Olesen, H.R., and *Franke, J.,* 2010: COST 732 Model Evaluation Case Studies: Approach and Results. Brussels, COST Office.

VDI, 2004: VDI 3738 Part 12. Environmental meteorology - Physical modelling of flow and dispersion processes in the atmospheric boundary layer. Application of wind tunnels. VDI Commission for Air Quality Management, Düsseldorf.

VDI, 2005: *VDI 3783, Blatt 9: Environmental meteorology - Prognostic microscale windfield models - Evaluation for flow around buildings and obstacles.* VDI Commission for Air Quality Management, Düsseldorf.

IDŐJÁRÁS

Quarterly Journal of the Hungarian Meteorological Service
Vol. 120, No. 2, April – June, 2016, pp. 231–254

Implementation and validation of a bulk microphysical model of moisture transport in a pressure based CFD solver

Norbert Rácz* and **Gergely Kristóf**

Department of Fluid Mechanics,
Budapest University of Technology and Economics (BME),
Bertalan L. u. 4-6, H-1111 Budapest, Hungary
E-mails: racz@ara.bme.hu; kristof@ara.bme.hu

**Corresponding author*

(Manuscript received in final form Auguszt 6, 2015)

Abstract—We study wet cooling tower plume formation involving mesoscale meteorological effects (such as stratification or compressibility). This was achieved by incorporating transformations and volume source terms into a pressure based computational fluid dynamics (CFD) solver (ANSYS-FLUENT). Moisture dynamics is taken into account with a bulk microphysical model that was recently implemented into the solver.

This model has been validated against known numerical solutions of idealized two-dimensional dry and wet thermals. In particular, the overall thermal profile and the liquid water concentration field indicated good model performance. Model performance has also been compared with measurements for the formation of a large wet cooling tower plume. Simulations are encouraging with regard to the predictability of cumulus like plume structures with complex thermal stratification, the overall liquid water content along the plume axis, and also the turbulent fluctuations caused by the vertical movements in the plume.

The advantage of this approach is that a uniform physical description can be used for close- and far-field flow by using a single unstructured mesh with local refinements. This allows for investigating the finely structured microscale flow phenomena around complex orographic features in a single framework.

Key-words: humidity transport, wet adiabatic processes, phase change, rising thermal, wet cooling tower plume

1. Introduction

A clear trend can be seen in the development of mesoscale meteorological codes towards the usage of higher resolution numerical models incorporating multiple physical effects in order to better describe the atmosphere, give higher resolution models for urban environments, or give higher fidelity forecasting. This is well reflected in the "urbanization" of mesoscale meteorological models (*Yamada*, 2003; *Otte et al.*, 2004; *Ooka et al.*, 2010), where microscale physical effects are introduced.

Another approach for multi-scale modeling is when computational fluid dynamical (CFD) solvers are adapted to handle mesoscale effects. The purpose of this paper is to enhance the latter approach.

General purpose CFD solvers are already widely used in modeling the ventilation of urban areas (*Mochida et al.*, 1997; *Balczó et al.*, 2011; *Kristóf* and *Balogh*, 2010). These solvers are capable of handling complex topography, buildings and have a wide variety of turbulence and physical models, effective numerical techniques, and parallelization.

In order to handle mesoscale effects in a general purpose CFD solver, we have recently developed a method (*Kristóf et al.*, 2009). The atmospheric stratification, the Coriolis force, and baroclinicity are taken into account by using simple (scale and shift) transformations of state variables (pressure, density, temperature), vertical velocity, and altitude, and including additional source terms in the conservation equations. The model was successfully validated (*Kristóf et al.*, 2009). Further simulations by *Rácz et al.* (2013) were performed around more complex geometrical features, idealized barriers, and real terrain, demonstrating the capabilities of this CFD based approach.

The contribution of this paper is to extend our original 2009 model with a proper moisture (humidity transport and phase change) model. We validate this extended model with numerical solutions of idealized two-dimensional dry and wet thermals and experimental data for a full-scale three-dimensional wet cooling tower plume formation with different environmental stratifications.

Several researchers investigated the behavior of cooling tower plumes from different aspects in the past decades. Wet cooling towers are widely used in the power generation industry, since it is relative easy to build and cheap to operate especially in regions where limited water resources are available for cooling purposes (*Al-Waked* and *Behnia*, 2006).

Most of the earlier studies are from the early 1970s related to the design, construction, and operation of nuclear and coal fired power plants. The performance of cooling towers is an important topic as the energy demand is growing. Few percent increase in overall efficiency in power generation could lead to high amount of total energy savings. Therefore, number of researches investigated the effect of changes in environmental conditions to the tower performance. *Al-Waked* and *Behnia* (2006) and *Lohasz* and *Csaba* (2012)

studied the effects of crosswind, *Kloppers* and *Kröger* (2005), *Overcamp* and *Hoult* (1971), *Barber et al.* (1974) studied temperature and humidity inversion and other parameters with CFD methods under different operating conditions. These effects are important since they could lower the efficiency of cooling towers (*Wei et al.*, 1995).

The visibility was not a great concern at that time, instead the plume rise of dry and wet plumes were investigated (*Hanna*, 1972; *Weil*, 1974). Wet cooling towers, however, do not have much control over the visible plume. (*Tyagi et al.*, 2012) The exhaust of the tower is generally saturated, and during certain weather conditions, it cannot be absorbed completely by the surrounding air. As a result, it will appear as fog and visible to human eye.

Another important aspect regarding wet cooling tower operation is the prevention of the growth of legionella bacteria in the cooling water. The various legionella species are the cause of Legionnaires' disease in humans, and the transmission is via the exposure to aerosols. The bacteria could live and travel hundreds of meters or even kilometers from the source (*Greig et al.*, 2004) .

Nowadays, environmental impacts are becoming more and more important concentrating not only on toxic materials but also on the visibility of water vapor plumes. The reduction of visibility conditions, the local reduction of solar radiation, and the interaction with low level clouds, in particular the fog, are in concern nowadays. The latest literature review about cooling towers shows different options for reducing and manipulating the visible plume using hybrid cooling towers, wet–dry cooling towers, dry cooling towers, and so on, depending on the need and demand. The formation of a visible water vapor plume is directly related to the water mass fraction, temperature, exhaust velocity of the tower, and also ambient meteorological conditions. In more recent studies, *Wang et al.* (2007), *Xu et al.* (2008) and *Wang et al.* (2009) investigated the control and abatement of plumes emitted by large commercial buildings by reheating the exhaust with heat pumps or solar collectors. *Sturman* and *Zawar-Reza* (2011) predicted the yearly visibility of a stack plume of a planned industrial site with an atmospheric mesoscale pollution model (TAPM) by providing boundary conditions from the meteorological code. *Presotto et al.* (2005) investigated the possibility of reducing the plume visibility by lowering the exit temperature of a petrochemical refinery.

There is usually no contaminant involved, but there is a risk of the plume's material returning to the ground level causing local fogging, ice formation, or entrainment of saturated air into other adjacent towers. *Mokhtarzadeh-Dehghan et al.* (2006) and *Spillane* and *Elsum* (1983) investigated the occurrence of rain and fog and the possibility of plum blow-out by strong winds. Their investigation showed that the fog can extend to the ground in cases, where the plume interacts with the wake of the tower and the ambient temperature is very low.

Number of researchers worked on the effect of drift deposition as it could be objectionable due to human health hazards. Their purpose was to investigate

the effects of ambient conditions and absolute humidity, droplet output temperature, and the affected area (*Lucas et al.*, 2010). Drift of small water droplets from mechanical and natural draft cooling towers can contain salt particles, water treatment chemicals, and bacteria. *Meroney* (2006) recommends a CFD protocol to correct drift and deposition predictions provided by current analytic models to take into account building effects.

Wet cooling tower plumes can also play a role in the formation of different kinds of hydrometeors. *Campistron* (1987) and *Huff* (1972) studied snowfalls caused by cooling towers and they found that the rate of precipitation can even be enhanced by a factor of two.

The increasing computational power makes the CFD based approach more and more affordable. Several investigations showed that CFD models are valid in predicting the flow field, performance, or drift deposition predictions of micro scale flow around cooling towers (*Balczó et al.*, 2011; *Kristóf and Balogh*, 2010; *Meroney*, 2006). We have successfully extended the capabilities of CFD solvers (*Kristóf et al.*, 2009; *Rácz et al.*, 2013) in order to simulate atmospheric scale flows. In this paper, a further enhanced model version will be shown that is capable of predicting moist dynamics through the implementation of condensation and phase change models.

In the next chapter, an overview will be given about the existing tools for modeling plume dispersion and about their advantages and limitations, a short description of the mesoscale model extension that we have recently validated, and more details on the further developed model version that also takes into account moist dynamics. In the third and fourth chapters, the model validation will be shown against calculations with meteorological codes and field measurements followed by the conclusions.

2. Mathematical model

Theories for describing the heat, mass, and momentum transfer inside natural draft cooling towers have long been established by authors in the early 1900s. These works (*Lewis*, 1922; *Robinson*, 1923) include also heat transfer due to vaporization, and therefore, they are applicable to the prediction of wet tower performance. These analysis and simplifications are still in use today, and several numerical models have been developed based on this study in order to describe transfer processes inside cooling towers (*Al-Waked and Behnia*, 2006).

Wide range of model complexity can be found in the literature regarding the modeling of plume formation outside of the tower. These models include simpler algebraic models towards more complex integral models, atmospheric dispersion models, or CFD based approaches. Commonly used plume models are based on conservation equations describing the entrainment processes of ambient air along the plume axis.

Several authors (*Hanna*, 1976; *Hanna et al.*, 1982) studied the dynamics of plume motion and developed numerical models. *Slawson and Csanady* (1967), *Wigley and Slawson* (1971), and *Csanady* (1973) identified three phases, the initial, intermediate, and final phases of plume rise. They developed a rise model for jets that is also applicable to ambient conditions with stable stratification.

Widely used models, e.g., the analytical models of *Briggs* (1975, 1984) and *Weil* (1974) describe reasonably well the first phase of plume rise near the source, however, they are valid only for constant density gradient and wind speed (*Briggs*, 1984). With the detrainment concept of *Netterville* (1990), the transitional region and the leveling can also be described. *Davidson* (1989, 1994) developed a formulation that is able to predict both plume rise and dilution.

The entrainment is often modeled by using different empirical coefficients (*Schatzmann and Policastro*, 1984). One reason of difference between model results of different formulations is due to the differences in empirical coefficients applied to obtain the analytic solution.

Early models did not account for phase change of water during the plume development and neglect the effect of turbulence to the entrainment. *Gangoiti et al.* (1997) and *Janicke and Janicke* (2001) have developed Gaussian dispersion type models that included prediction of condensation and are also applicable to complex wind fields. Condensation and evaporation of droplets is important, since it changes buoyancy by introducing and removing latent heat during the rise and leveling. The lack of plume condensation causes the underestimation of plume rise in simpler models.

Another usual limitation is the improper handling of the complex atmospheric stratification and wind fields. Simplifications often assume winds depending only on the height above the ground, or constant wind speed and direction along the plume axis. In the case of complex input meteorological conditions data are often extrapolated from nearby meteorological stations to represent ambient conditions at the source. However, this causes accuracy problems (*Presotto et al.*, 2005). Simpler models could give good results in certain conditions when the lower few 100 meters of the atmosphere is linearly stratified. However, in the cases of high exhaust temperatures, the plume can penetrate deeply into the atmosphere crossing different layers with different lapse rates. This is typical for stack plumes of wet scrubbers with high exhaust temperatures.

The proper estimation of plume rise height is especially important when the deposition of plume particles or ground level concentration is to be calculated. *Policastro et al.* (1978) compared drift deposition models to experimental data and found that the existing models did not perform well.

The formulation of *Briggs* (1984) extended with empirical coefficients for plume trajectory are in use in environmental protection regulatory models (*Gangoiti et al.*, 1997). For short-range transport, the modifications to the EPA

Point, Area Line Source Algorithm (PAL2.1), the EPA Industrial Source 5 Complex Short Distance 3 (ISCST3) model, and the Argonne National Laboratory Seasonal/Annual Cooling Tower Impact (SACTI) model ((*Carhart and Policastro*, 1991; *Policastro et al.*, 1994) are used. Some of the limitations described above were addressed later in the development of ISC-PRIME and AERMOD-PRIME models in order to replace ISC3 series models ((*Schulman et al.*, 1997; *Petersen*, 2004)). The current trend in modeling for urban air pollution is focused on the improvement of advection in atmospheric dispersion models (atmospheric dispersion models TAPM, Ausplume, and CALPUFF (*Brown and Fletcher*, 2005)) and integrating them with local scale models (see, e.g., the EUROTRAC-2 subproject SATURN; (*Moussiopoulos*, 2010)). These models are currently accepted by regulatory authorities.

In the last decade, new generation of Gaussian dispersion models were introduced with a better description of real physical processes in the atmospheric boundary layer. Examples are the Danish OML model (*Olesen et al.*, 2007), or the British UK-ADMS model (*Carruthers* and *McHugh*, 2009). These often contain integrated systems for different purposes: street canyon models, Gaussian plume models, Eulerian grid models and dispersion model. These model families could give reasonable results in the far field, however, it could give under or overestimation by a factor of two when complex topography and buildings are considered and near filed concentration is a concern (*Mcalpine* and *Ruby*, 2004; *Olesen et al.*, 2007).

CFD based tools have also been used recently to assess plume visibility (*Brown* and *Fletcher*, 2005). Current CFD models however have limited capabilities. They were mostly used to investigate the wind field under steady state conditions, not representing the spatial and temporal variability of the meteorological fields especially around complex terrain (as recognized by *Brown and Fletcher* (2005). They often include assumptions for the vertical atmospheric profiles that do not reflect real conditions (as cautioned by *Presotto et al.* (2005)), and frequently exclude effects of surface vegetation and soil. These issues have been addressed by introducing the transformation method described in (*Kristóf et al.*, 2009; *Rácz et al.*, 2013) and (*Kristóf* and *Balogh*, 2010).

Using the commercial CFD tool ANSYS-FLUENT, continuity, momentum and energy equations are solved based on the finite volume method in an unsteady conservative form. Through user defined functions (UDF), the user can modify the governing equations of the CFD code by adding appropriate source/sink terms to the governing equations (Eqs. (1)–(6)). The current adaptation method can also be implemented in other CFD solvers having UDF capabilities such as ANSYS-CFX, StarCD, or the open source solver Openfoam.

$$\nabla \cdot \tilde{v} = 0, \tag{1}$$

$$\frac{\partial}{\partial t}(\rho_0 \tilde{\mathbf{v}}) + \nabla \cdot (\rho_0 \tilde{\mathbf{v}} \otimes \tilde{\mathbf{v}}) = -\nabla \tilde{p} + \nabla \cdot \boldsymbol{\tau} + (\tilde{\rho} - \rho_0)\mathbf{g} + \mathbf{F}, \tag{2}$$

$$\frac{\partial}{\partial t}\left(\rho_0 c_p \tilde{T}\right) + \nabla \cdot \left(\tilde{v}\ \rho_0\ c_p \tilde{T}\right) = \nabla \cdot \left(K_t \nabla \tilde{T}\right) + S_T, \tag{3}$$

$$\frac{\partial}{\partial t}(\rho_0\ k) + \nabla \cdot (\rho_0\ \tilde{v}\ k) = \nabla \cdot \left(\frac{\mu_t}{\sigma_k} \nabla k\right) + G_k + G_b - \rho_0\ \varepsilon + S_k, \tag{4}$$

$$\frac{\partial}{\partial t}(\rho_0\ \varepsilon) + \nabla \cdot (\rho_0\ \tilde{v}\ \varepsilon) = \nabla \cdot \left(\frac{\mu_t}{\sigma_\varepsilon} \nabla \varepsilon\right) + \rho_0\ C_1\ S\ \varepsilon - \rho_0\ C_{2\varepsilon} \frac{\varepsilon^2}{k + \sqrt{\nu\ \varepsilon}} + C_{1\varepsilon} \frac{\varepsilon}{k} C_{3\varepsilon} G_b + S_\varepsilon, \tag{5}$$

$$\tilde{\rho} = \rho_0 - \rho_0\ \beta\left(\tilde{T} - T_0\right). \tag{6}$$

In the equation system $\tilde{v}, \tilde{p}, \tilde{\rho}, \tilde{T}$ are the transformed field variables of velocity, pressure, density, and temperature. c_p and β are the specific heat capacity of dry air at constant pressure and the thermal expansion coefficient. From the velocity vector ($\tilde{v} = u\,i + v\,j + \tilde{w}\,k$) only the vertical component was affected by the transformation. τ contains the viscous and turbulent stresses, $g = -g\,k$ is the gravitational force per unit, mass and $g = 9.81[\mathrm{N\ kg^{-1}}]$. Turbulent transport is modeled by the realizable k–ε turbulence model with full buoyancy effects (Eqs. (4)–(5)) developed by *Shih et al.* (1994), where σ_k and σ_ε are the turbulent Prandtl numbers for k and ε, respectively. The turbulent viscosity μ_t and the turbulent heat conduction coefficient K_t are evaluated on the basis of turbulence kinetic energy (k) and dissipation rate (ε) fields. The constant values of $C_{1\varepsilon}$, $C_{2\varepsilon}$, the expressions of C_1 and $C_{3\varepsilon}$, the turbulence production and buoyancy terms G_k and G_b, and the modulus of mean rate-of-strain tensor (S) can be referred either from CFD literature (*Shih et al.*, 1994) or from software documentation (*ANSYS Inc.*, 2013). r_0 and T_0 are reference (sea level) values of density and temperature. Volume sources, responsible for the handling of mesoscale effects, S_T, S_k, and S_ε in Eqs. (3)–(5), as well as vector $F = S_u\,i + S_v\,j + S_w\,k$ in Eq. (2), are functions of local values of field variables. The components of the Coriolis force are included in **F** through S_u, S_v, *and* S_w.

The interested reader is referred to (*Kristóf et al.*, 2009) and (*Rácz et al.*, 2013) where a full description and validation cases of the transformation method can be found, therefore, further details regarding the basic equations are not given here.

Several authors treated moisture by means of various warm cloud microphysical models of different complexity. These approaches range from simple single-moment (*Kessler*, 1969) and two-moment (*Ziegler*, 1985; *Cohard* and *Pinty*, 2000; *Morrison et al.*, 2005) bulk parameterizations to more complex bin microphysics schemes (*Feingold et al.*, 1994; *Kogan*, 1991; *Ackerman et al.*, 2004). Typically in bulk microphysics, the liquid water is separated into two categories: non-precipitable cloud water and precipitable rain water (*Kessler*, 1969).

2.1. *Transport equations*

The extended commercial CFD solver we used is essentially closed source, but it is allowed to setup and use arbitrary number of passive scalar equations during the solution. Therefore, in order to describe the phase change, three additional scalar equations (Eqs. (7)–(9)) were considered for the number concentration of cloud condensation nuclei n_{CCN} (in order to track CCN depletion and entrainment effects, where subscript CCN refers to cloud condensation nuclei) and the number of condensed water droplets N_c together with total water content of air q_t. Rain water is currently neglected, since condensation will determine the growth of drops smaller than about 20 μm and no larger droplets are expected during the initial rise of a thermal or during the cooling tower plume rise.

$$\frac{\partial \rho n_{CCN}}{\partial t} + \frac{\partial}{\partial x_i}\left(\rho u_i n_{CCN} - \Gamma \frac{\partial n_{CCN}}{\partial x_i}\right) = \left(S_{n_{CCN}}\right)_{act} + \left(S_{n_{CCN}}\right)_{evap} + \left(S_{n_{CCN}}\right)_{sed}, \tag{7}$$

$$\frac{\partial \rho q_t}{\partial t} + \frac{\partial}{\partial x_i}\left(\rho u_i q_t - \Gamma \frac{\partial q_t}{\partial x_i}\right) = \left(S_{q_t}\right)_{act} + \left(S_{q_t}\right)_{cond/evap} + \left(S_{q_t}\right)_{sed}, \tag{8}$$

$$\frac{\partial \rho N_c}{\partial t} + \frac{\partial}{\partial x_i}\left(\rho u_i N_c - \Gamma \frac{\partial N_c}{\partial x_i}\right) = \left(S_{N_c}\right)_{act} + \left(S_{N_c}\right)_{cond/evap} + \left(S_{N_c}\right)_{sed}, \tag{9}$$

$$q_t = q_v + q_l, \tag{10}$$

where q_v and q_l are the specific humidity of water vapor and liquid water per unit mass. Γ is the diffusion coefficient of the given scalar.

In order to simulate mean sizes and concentrations of droplets in wet plumes, the scheme needs to represent processes that would affect the droplet spectra of the plume (right side of Eqs. (7)–(9)). These are the activation of droplets on condensation nuclei, condensation/evaporation of droplets, entrainment of ambient air (*Warner*, 1969; *Paluch* and *Knight*, 1984; *Brenguier* and *Grabowski*, 1993; *Su et al.*, 1998; *Lasher-trapp et al.*, 2005), and additional activation of droplets (*Warner*, 1969; *Pinsky* and *Khain*, 2002).

The relationship between droplet number (N_c) and liquid water content (q_l) is determined by using a log-normal droplet size distribution function (Eqs. (11)–(12)):

$$n_c(r) = \frac{N_c}{r\sigma_c\sqrt{2\pi}} \exp\left(-\frac{1}{2\sigma_c^2}\left(\ln\frac{r}{r_0}\right)^2\right), \tag{11}$$

$$\bar{r}_3 = r_0 \exp\left(\frac{3}{2}\sigma_c^2\right) \text{ and } \rho q_l = \frac{4}{3}\pi \bar{r}_3^3 \rho_w N_c, \tag{12}$$

where r is the droplet radius, r_0 is the distribution median value, σ_c is the logarithmic standard deviation, $\bar{r}_3$ is the mean mass radius, and ρ_w is the density of water.

Atmospheric aerosols and cloud condensation nuclei play an important role in the condensation of droplets and evolution of clouds. In this study, the method described by *Cohard et al.* (1998) was chosen to describe the relationship between supersaturation and the nucleated number of droplets (N_{CCN}), as it is computationally more efficient, gives more robust estimates (*Grabowski*, 2006), and requires less programming efforts.

$$N_{CCN} = Cs^k F\left(\mu, \frac{k}{2}; \frac{k}{2}+1; -\beta s^2\right), \tag{13}$$

where C = 3270 cm^{-3} is a parameter of the nucleation process, s is the supersaturation, F is the hyper-geometric function and μ = 0.7, β = 136, and k = 1.56 are parameters characterizing the aerosol distribution of a continental type of air mass. Eq. (13) is the extension of the simple and famous power law formula of *Twomey* (1959) but improved to give better results from weak to strong supersaturations.

Given the number of nucleated drops, the source term due to nucleation can be calculated assuming heterogeneous nucleation (*Pruppacher et al.*, 1998).

$$\left(S_{N_c}\right)_{act} = \frac{1}{\Delta t}\max\left(N_{CCN,\max} - N_c, 0\right), \tag{14}$$

where Δt is the numerical time step. It is assumed that condensation and evaporation proceed through changes of q_c without any effects on N_c (*Richard and Chaumerliac*, 1989) except during activation of CCN and total evaporation of smaller droplets.

2.2. Droplet growth by activation and diffusion

Once droplets are activated, the two primary components of their growth are the vapor diffusion and collision-coalescence. Since rain water is neglected, only growth by diffusion is considered. The critical radius of newly formed droplets can be calculated according to the Köhler theory (see, e.g., (*Pruppacher et al.*, 1998)).

$$\left(r_{crit}\right)_{act} = \frac{4}{3} M_w \sigma_w R \rho_w T (s/100), \tag{15}$$

where M_w and σ_w are the molecule mass and surface tension of the water substance, R and T are the universal gas constant and the physical temperature of ambient air.

The corresponding source term due to activation for the liquid water content is:

$$\left(S_{q_t}\right)_{act} = \frac{4\pi\rho_w}{3\rho} r_{crit}^3 \left(\frac{\partial N_c}{\partial t}\right)_{act}, \tag{16}$$

The condensation rate can be calculated based on (*Pruppacher et al.*, 1998):

$$\left(S_{q_t}\right)_{cond/evap} = \frac{4\pi r(s - A + B) f_v}{G(T, p)}, \tag{17}$$

where A, B, and f_v express curvature, solute, and ventilation effects and $G(T, p)$ is a term dependent on local thermodynamic variables.

$$A = \frac{2\sigma_w}{R_v T \rho_w r}, \quad B = \frac{\varepsilon \nu \Phi_s M_w m_a}{M_s (m - \rho_w m_a / \rho_s)}, \quad G(T, p) = \frac{L_v}{k_a T}\left(\frac{L_v}{R_v T} - 1\right) + \frac{R_v T}{p_{sat} D_v}, \tag{18}$$

where ε is the water-soluble fraction of the aerosol, the product $\upsilon\Phi_s$ is the van't Hoff factor, ρ_s and m_a are the aerosol density and mass, m is the droplet mass, M_w and M_s are the molecular mass of water and solute, L_v is the latent heat of evaporation, R_v is the specific gas constant of water vapor, k_a and D_v are the modified thermal conductivity and diffusivity of air and water vapor, p_{sat} is the saturated vapor pressure over flat water surface at environmental temperature.

2.3. Partial and total evaporation of droplets

Droplets evaporate once convected to unsaturated regions ($s < 0$). This process is described based on the work of *Chaumerliac et al.* (1987). Due to partial evaporation, drops with a size smaller than a certain threshold (r_{crit}) will be removed from the system, therefore resulting a decrease in N_c. The corresponding source term is:

$$\left(S_{N_c}\right)_{evap} = \frac{1}{\Delta t} \int_0^{r_{crit}} \frac{N_c}{r\sigma_c\sqrt{2\pi}} \exp\left(-\frac{1}{2\sigma_c^2}\left(\ln\frac{r}{r_0}\right)^2\right) dr, \tag{19}$$

where r_{crit} can be calculated as follows:

$$r_{crit} = \sqrt{(-2\ A3^{-1}\ s\ \Delta t)}, \tag{20}$$

$$A3 = \frac{\rho_w R_v T}{p_{sat} D_v} + \frac{L_v \rho_w}{k_a T}\left(\frac{L_v}{R_v T} - 1\right). \tag{21}$$

Total evaporation of droplets will occur when the calculated mass of evaporated drops is larger than the mass present in the given volume. In this case $Nc = 0$ and the local CCN number is regenerated. The sedimentation terms on the right side of Eqs. (7)–(9) can be used to describe the settling of droplets, however, the settling terms are not considered here, as they are expected to be small in certain plume dispersion cases (*Bouzereau et al.*, 2008).

The superstauration s is calculated based on the saturation pressure (Eq. (22)). It is calculated for flat water surfaces based on the formula of *Bolton* (1980). The expression is accurate to 0.3% for –35 °C < T < 35 °C temperature range.

$$p_{sat} = 6.112 \exp\left(\frac{17.67\, T}{243.5 + T}\right), \tag{22}$$

where T and p_{sat} are in °C and hPa.

The following expressions give the connection between water vapor mass fraction and vapor pressure:

$$p_v = \left(\frac{q_v}{0.622 + q_v}\right) p, \tag{23}$$

where p_v and p are the vapor partial pressure and the pressure of moist air.

Finally, the supersaturation is given by the following formula:

$$s = \frac{p_v}{p_{sat}} - 1, \tag{24}$$

In the following chapter, the transformation and the microphysics scheme will be validated against the simulation of an idealized two-dimensional rising thermal and three-dimensional full scale plume dispersion cases.

3. Results

3.1. Numerical experiments with two-dimensional rising thermals

It is common in the development of microphysical schemes, that researchers test their models' behavior with idealized two-dimensional simulations. A frequently used generic test case is a rising thermal simulation in a stably stratified environment. Two types are common in the literature, one where the development of the thermal is initiated by surface heating (see, e.g., (*Klaassen* and *Clark*, 1985)) and another type when an initial perturbation (potential temperature, vapor content, etc.) is placed in the domain at a certain height. The latter one, described by *Grabowski* and *Clark* (1991), will be used here as a test case for validation, as it allows shorter computation due to not simulating the initial development phase of the thermal.

3.1.1. Rising thermal in a dry stable atmosphere

In order to separate the moist dynamics from discretization effects, the rise of a dry thermal in a Bousinesq fluid was simulated first.

The model domain was 3.6 km wide in the horizontal and 2.4 km in the vertical direction with equidistant mesh resolution. Different grid sizes of 20, 10, 5, 2.5, and 1.25 m were tested in order to see mesh sensitivity of the solution. The lateral boundaries were defined as periodic boundary, the top and bottom boundaries as free slip adiabatic walls. The initial circular perturbation was placed at $x = 0$ km and $z = 0.8$ km with a radius of 500 m and 0.5 K higher initial temperature than the constant ambient temperature 287 K. Third order MUSCL schemes (monotone upstream-centered schemes for conservation laws, (*van Leer*, 1979)) were used when solving the momentum and energy equations, as they can effectively suppress the non-physical oscillations with the introduction of adaptive numerical dissipation into numerical solutions. All transformation source terms in Eqs. (2)–(5) were turned off in this case. The total flow time was 8 min with a time step of 1 s. Results were compared to standard nonoscillatory MPDATA simulations showed in Section 4 in *Margolin et al.* (1997).

At 20 m and lower resolutions, results were starting to degrade rapidly, the interfacial eddies were smeared out (not shown here). A converged solution could be obtained at higher resolutions, the 5, 2.5, and 1.25 m cases were virtually identical (see *Fig. 1*). During the solution, the viscosity was explicitly defined and was varied among the different cases. *Fig. 2* shows that the results are less sensitive to the changes of the predefined viscosity in the investigated range.

Overall, a good correspondence can be found regarding the gross features; the rise height and size of the final shape of the bubble agrees well. There are differences in the fine details, though, the size and position of interfacial eddies slightly differ from the MPDATA solutions.

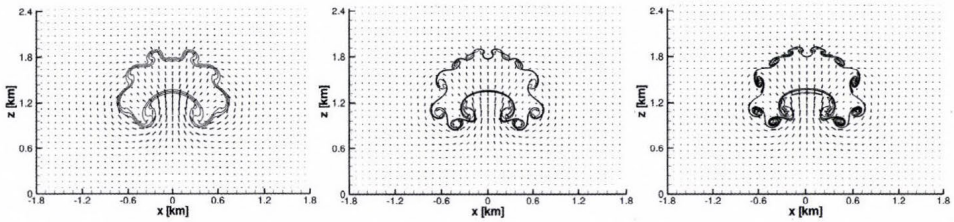

Fig. 1. Mesh sensitivity of the developed interfacial eddies. The equidistant mesh resolution is 20 m, 5 m, 1.25 m from left to right, and the viscosity is 0.5 $m^2 s^{-1}$ for all cases.

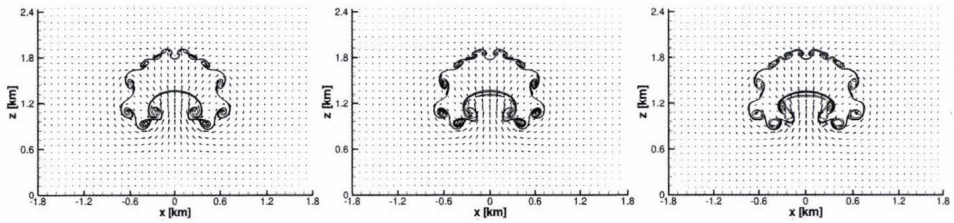

Fig. 2. Sensitivity of the developed interfacial eddies to the viscosity. The viscosity is 1, 0.5, 0.1 $m^2 s^{-1}$ from left to right, and the mesh resolution is 2.5 m for all cases.

3.1.2. Rising of a moist thermal

Model behavior changed significantly when moist dynamics were activated. The domain in this case was the same as above with an equidistant resolution in both spatial directions of 40, 20, 10, 5, 2.5 m. The initial perturbation of relative humidity (RH = 100 %) was placed at 0.8 km height with a diameter of 200 m that was smoothly relaxed to the environmental value within approximately 250 m radius. The environmental base state stability and the relative humidity were set to $dln\theta/dz$ = 1.3 10^{-5} m^{-1} and 20%, and the perturbation relaxation of RH was defined as:

$$RH = 20\% + 80\% \cos^2\left(\frac{\pi}{2}\frac{r-200}{100}\right), 200\text{m} < r < 300\text{m}. \tag{25}$$

The lateral, top, and bottom boundaries were defined as periodic and free slip adiabatic walls with a temperature of 289 K at the lower surface. The eddy viscosity of the air was explicitly defined and varied between 0.25 and 2 $m^2 s^{-1}$ among the simulation cases.

Third order MUSCL schemes, pressure staggering option (PRESTO) (*ANSYS Inc.*, 2013) were used when solving the momentum and energy equations,

and for pressure interpolation. Results were compared to series of non-oscillatory MPDATA solutions presented in Section 3 in (*Grabowski* and *Clark*, 1991)

The general formation of the liquid water field of the thermal is illustrated in *Fig. 3*. During the initial 4 min of rise, a very good match can be found. This period was weakly affected by the mesh resolution or the predefined viscosity (not shown here). At higher resolutions (5 m and 2.5 m), the model predictions were fairly close to the semi-Lagrangian and Eulerian MPDATA solutions, the overall shape and rise height were similar, the interfacial eddies were well resolved. Differences can be found in the fine details, though, the exact position and shape of interfacial eddies are somewhat different but still close to the semi-Lagrangian model results that is superior in capturing the interface instability (see Section 4a of *Grabowski* and *Smolarkiewicz* (1996)). At low spatial resolutions, the CFD model still captured the overall shape, but the quality degraded quickly, no interfacial eddies could be found at 20 m resolution. However, the erosion of cloud water field was not as strong as the Eulerian MPDATA model showed at the same resolution.

Overall, the model output is in *Figs. 4* and *5* suggest that the results are converging to a common solution, and it is in a good agreement with the MPDATA results. Differences are possibly due to the different numerical schemes and the lack of precipitation scheme in the CFD model.

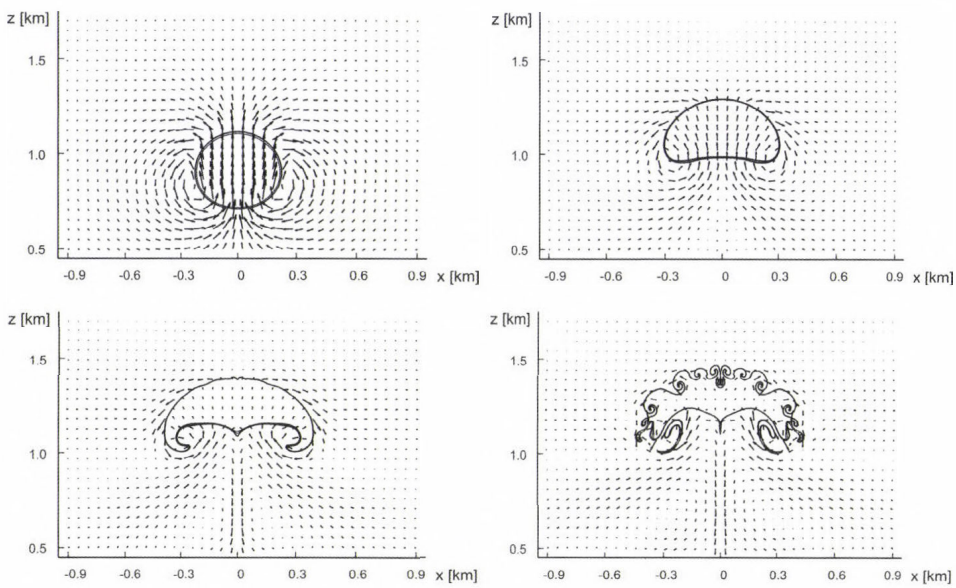

Fig. 3. Development of the initial water vapor perturbation. Isolines of q_l field at $t = 2$, 4, 6, and 8 min of the moist thermal rise. The viscosity and the mesh resolution are 0.5 $m^2 s^{-1}$ and 2.5 m in each panel. Contour intervals for q_l are 0.05, 0.1, 0.2, and 0.3 g kg^{-1}.

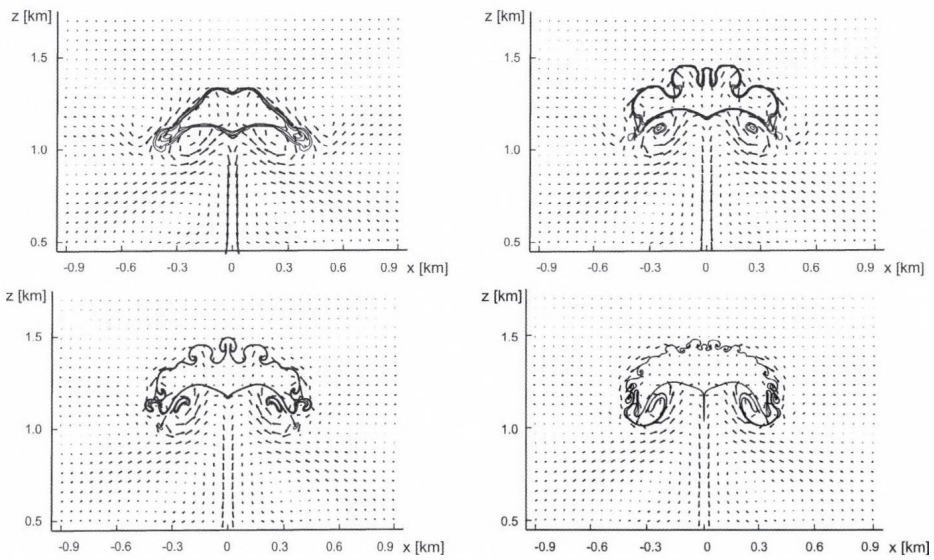

Fig. 4. Same as *Fig. 3.* but for different mesh resolutions. From left to right, the mesh sizes are 20, 10, 5, and 1.25 m. The viscosity is 0.5 m^2s^{-1}.

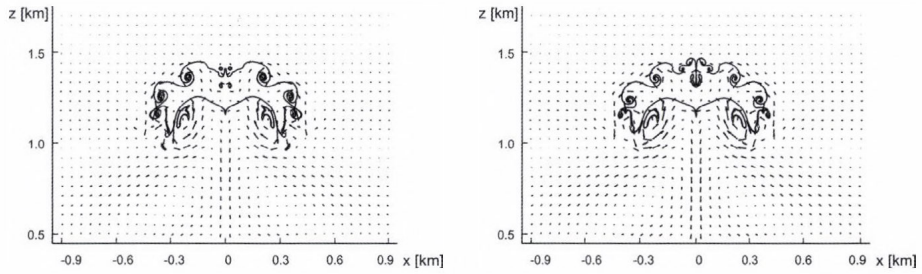

Fig. 5. Same as *Fig. 3* but for different viscosities. Mesh resolution is 2.5 m, viscosity is 0.1 and 0.25 $m^2 s^{-1}$ (from left to right).

3.2. Simulation of plume formation of a wet cooling tower, the Bugey 1980 field campaign

In this chapter, the CFD simulation results will be compared to full scale measurement data that was collected during a large measurement survey around wet cooling towers of a nuclear power plant around Bugey, France. Radio-

soundings, droplet spectra, airborne measurements, measurements describing the ambient thermodynamic states as well as photographic records are available for comparision (*Bouzereau et al.*, 2008).

3.2.1. Initial and boundary conditions

During the campaign, very different plume shapes were observed from which two of the characteristic cases were selected for comparison. The first one (March 11, 1980) was characterized by high wind shear, conditionally unstable stratification, and an upper layer with high relative humidity. The second one (March 12, 1980) had lower ambient wind speed, more stable stratification and as a result, smaller horizontal plume extent characterized by sharp plume bent-over.

The domain in both cases covers a 10 km × 4 km area with a total height of 4 km. An equidistant grid was used during the simulations with a resolution of 40 m that was adaptively refined in two steps around the tower and the plume, resulting a minimum grid size of 10 m in critical areas. The interpolated initial and boundary profiles for the domain as well as the plume exit conditions, the vertical velocity, temperature, turbulence profiles, and the liquid water content were based on the radiosoundings and previous calculations of *Bouzereau et al.* (2008) (see *Fig. 6* for the atmospheric profiles and *Table 1* for tower exit conditions). Turbulent kinetic energy k and its dissipation ε at the tower exit were set to 1.7 $m^2 s^{-2}$ and 0.07 $m^2 s^{-3}$ in both cases. Droplet number concentration at the tower exit was deduced from measurements, i.e., $N_c = 10^4$ cm^{-3}. The nucleation parameterization was after *Cohard et al.* (1998) using parameters for a continental type of air mass, i.e., $C = 3270$ cm^{-3}, $k = 1.56$, $\mu = 0.70$, $\beta = 136$, and $\sigma_c = 0.28$. The time step was 1 s and the total integration time was 3600 s in both cases.

Table 1. Plume exit conditions for March 11 and 12, 1980. Exit conditions for the towers 4E–W and 5E–W are given separately. Subscript "env" refers to environmental values. The tower exit temperature ΔT is given compared to the environmental values. w and q_l are the vertical velocity component and the liquid water content, respectively, at the tower exit.

Tower exit conditions	q_l [g kg^{-1}]		ΔT [°C]		w [ms^{-1}]		T_{env} [°C]	p_{env} [Pa]
	4E-W	5E-W	4E-W	5E-W	4E-W	5E-W		
March 11	0.889	0.719	18.34	17.77	3.8	3.73	4.44	97771
March 12	0.8	0.8	18.2	17.7	3.8	3.7	3.31	97994

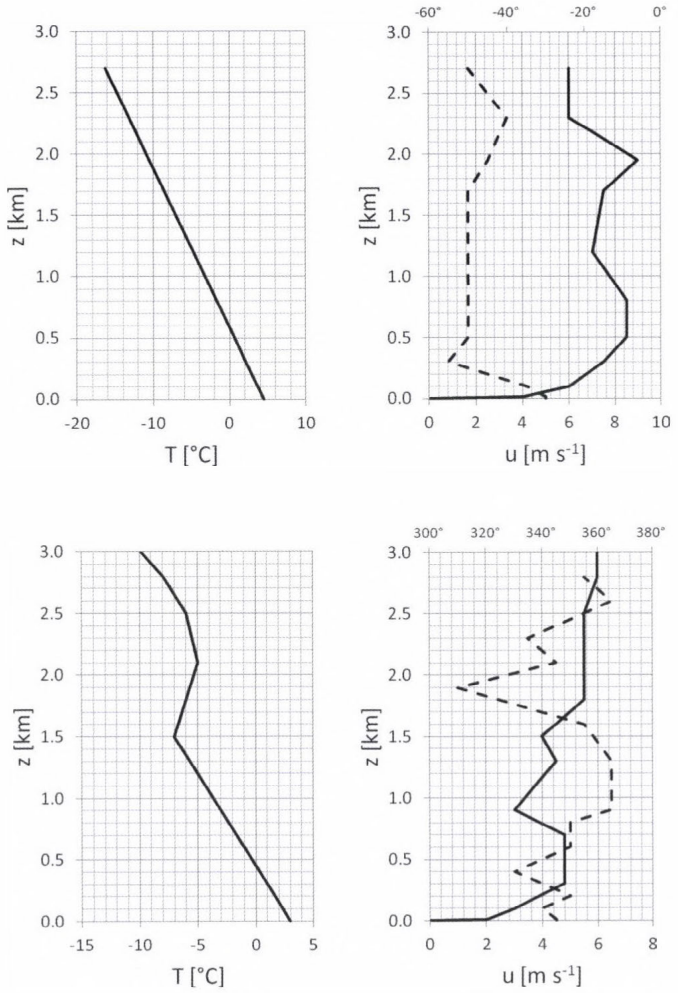

Fig. 6. Ambient initial and boundary conditions for the March 11, 1980 (top) and March 12, 1980 (bottom) cases. Left panel: ambient temperature. Rigth panel: wind speed (solid line) and wind direction (dashed line).

3.2.2. Simulation results of plume formation

Moist air is injected at the tower exit into the atmosphere characterized by strong shear with a high relative humidity upper layer, resulting in a periodic cumulus like plume formation farther downstream of the tower. This phenomena is well captured by the CFD code compared to visual observations and existing calculations (see Chapter 4 and Appendix A of *Bouzereau et al.* (2008)). The

oscillation in the liquid water content (LWC) field observed as rising thermals in *Fig. 7.* shows a wave length of about the same as the model output of the MERCUR code presented in *Bouzereau et al.* (2008) and of the observations. The first thermal-like structure appears closer downstream of the tower in the CFD model, that could be explained by differences in the turbulence level, and by the effect of higher resolution mesh in critical areas.

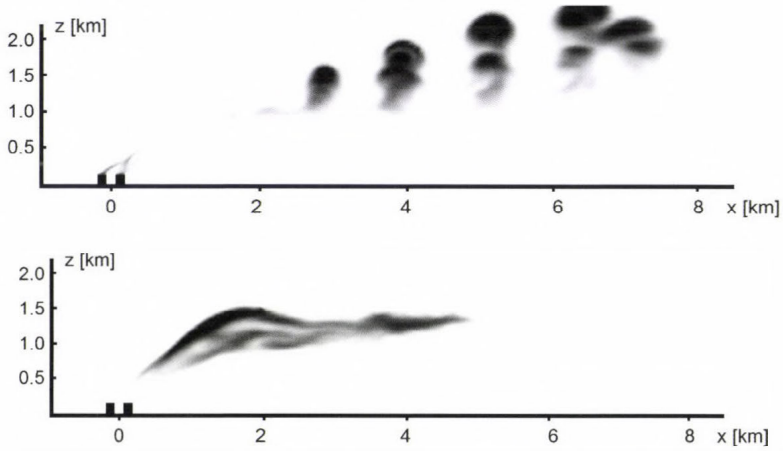

Fig. 7. Volume rendering of the LWC field of the simulated plumes, March 11, 1980 (top) and March 12, 1980 (bottom). The field is transparent below $q_l = 0.01$ g kg^{-1} and opaque when higher than 1.0 g kg^{-1} with 0.1 g kg^{-1} steps in the opacity.

A quantitative comparison is shown in *Fig. 8* where CFD model output is plotted against available aircraft data. In order to obtain valuable results on plume formation and dispersion, it is important to have good initial data on the vertical thermal structure as well as wind shear and humidity. The temperature field was well captured by the simulation, it follows the ambient temperature profile, and the aircraft data lies well between the simulated extremum. The maximum simulated values of LWC field were also compared to recorded data during the campaign. Although aircraft data for LWC was not available for comparison for the initial rise, in the layer between 900 m and 1800 m the simulation compares well, tendencies in liquid water field are well captured for the high wind case with a slight overestimation along the plume axis. During aircraft data sampling, data for instantaneous vertical velocity was also collected. This cannot be compared directly to simulation output, as vertical velocity from URANS simulations does not contain the fluctuation component of the wind speed. However, it is possible to deduce approximate values from the turbulence kinetic energy field. The survey shows significant fluctuations in the velocity field, which is also well reflected in the simulation results.

The simulated plume height could be extracted from *Fig. 8*, where the liquid water content is starting to drop significantly. The simulation showed slight overestimation for the high wind case, it gave values between 2000 m and 2500 m, while during the survey a height of ~1950 m and ~2250 m was observed.

In general, the model showed good overall performance with the CFD model improved with the bulk microphysical scheme. Further steps will include the implementation of sedimentation and precipitation schemes.

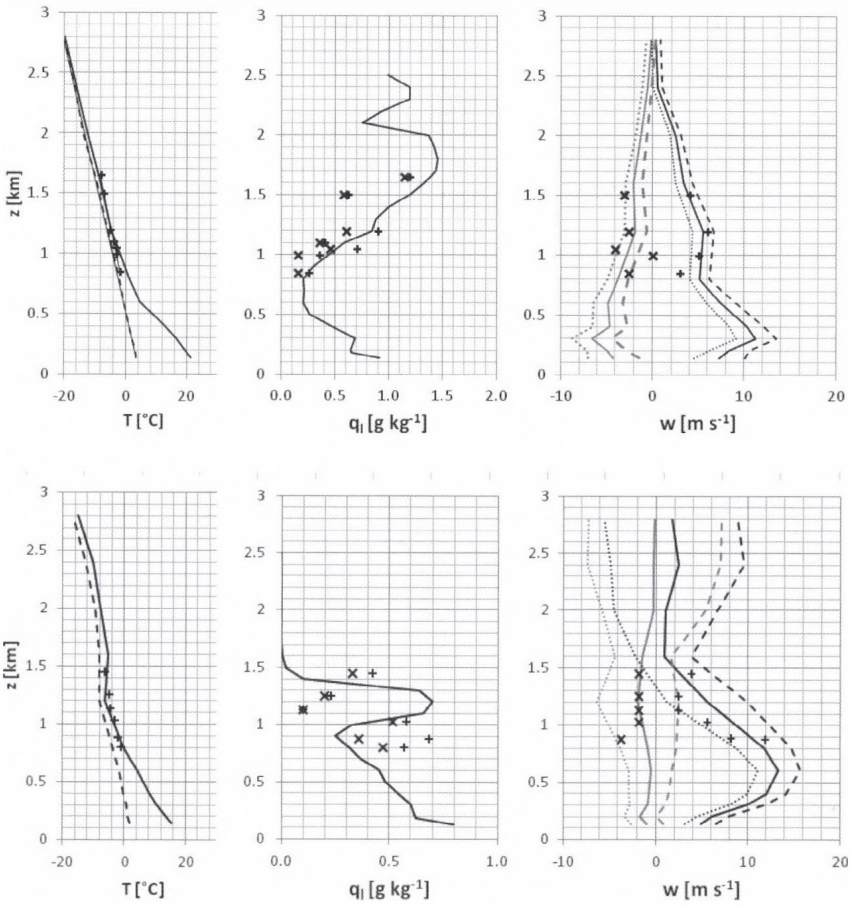

Fig. 8. Simulation results for March 11, (top panels) and March 12,1980 (bottom panels) compared to the aircraft measurements. On the left: maximum (solid line) and minimum (dashed line) of the simulated temperature. Symbols: measured temperature average through the plume. Center: predicted maximum of the LWC field (solid line) at each level. Symbols: 'x' and '+' represent the measured minimum and maximum of the LWC. Right panels: simulated vertical velocity *w* (solid lines: maximum in black, minimum in grey). Doted and dashed lines show the fluctuation components. Symbols: 'x' and '+' represent the minimum and maximum instantaneous vertical velocities observed at each flight level.

4. Summary and conclusions

A transformation method was developed in the past in order to extend the capabilities of commercial CFD solvers with mesoscale effects. Thermal stratification, adiabatic cooling caused by hydrostatic pressure driven expansion, compressibility, and Coriolis force were taken into account with the help of a transformation system and customized volume sources applied to the governing equations. In this paper further advances were shown. A bulk warm microphysical scheme was implemented in the solver in order to simulate humidity transport and phase change in atmospheric flows.

Model results were successfully validated with the rise of idealized two-dimensional dry and wet thermals. We have then applied the model to the simulation of wet plume formation originated from a cooling tower of a large nuclear power plant.

Results obtained from our simulations are encouraging with regard to the predictability of cumulus-like plume structures in the far field of the tower formed in complex wind field and thermal stratification, the overall liquid water content along the plume axis, and also the turbulent fluctuations caused by the vertical movements in the plume.

Using only one single unstructured grid and a uniform physical description for close- and far-field flow, one can take the advantage of the model adaption in the simulation of mesoscale atmospheric phenomena. In a single framework, one can investigate the finely structured microscale flow around complex geometrical features, such as flow around buildings with pollution dispersion or study the close- and far-field of wet cooling tower plumes and its effects to the environment.

Acknowledgments: The scientific work presented in this article was supported by the project K108936 "Flow and dispersion phenomena in urban environment" of the Hungarian Scientific Research Fund.

References

Ackerman, A. S., Kirkpatrick, M. P., Stevens, D. E., and *Toon, O. B.*, 2004: The impact of humidity above stratiform clouds on indirect aerosol climate forcing. *Nature 432*, 1014–1017.

Al-Waked, R., and Behnia, M., 2006: CFD simulation of wet cooling towers. *Appl. Therm. Eng. 26*, 382–395.

ANSYS Inc., 2013: FLUENT 13 documentation. In: Fluent User Services Center.

Balczó, M., Balogh, M., Goricsán, I., Nagel, T., Suda, J., and *Lajos, T.*, 2011: Air quality around motorway tunnels in complex terrain–Computational Fluid Dynamics modeling and comparison to wind tunnel data. *Időjárás 115*, 179–204.

Barber, F., Martin, A., Shepherd, J., and *Spurr, G.*, 1974: The persistence of plumes from natural draft cooling towers. *Atmos. Environ. 8*, 407–418.

Bolton, D., 1980: The computation of equivalent potential temperature. *Mon. Weather Rev. 108*, 1046–1053.

Bouzereau, E., Musson Genon, L., and *Carissimo, B.*, 2008: Application of a semi-spectral cloud water parameterization to cooling tower plumes simulations. *Atmos. Res. 90*, 78–90.

Brenguier, J.-L., and *Grabowski, W. W.*, 1993: Cumulus entrainment and cloud droplet spectra: A numerical model within a two-dimensional dynamical framework. *J. Atmos. Sci. 50*, 120–136.

Briggs, G. A., 1975: Plume rise predictions. *Lect. Air Pollut. Environ. Impact Anal. AS, 59-1 1.*

Briggs, G. A., 1984: Plume rise and buoyancy effects. *Atmos. Sci. Power Prod.* 327–366.

Brown, G. J., and Fletcher, D. F., 2005: CFD prediction of odour dispersion and plume visibility for alumina refinery calciner stacks. *Process Saf. Environ. Prot. 83*, 231–241.

Campistron, B., 1987: Interaction between a natural snowfall and a cooling tower plume: An experimental study with a millimetric Doppler radar. *Atmos. Environ. 21*, 1375–1383.

Carhart, R. A. and *Policastro, A. J.*, 1991: A second-generation model for cooling tower plume rise and dispersion—I. Single sources. *Atmos. Environ. Part A. Gen. Top. 25*, 1559–1576.

Carruthers, D. and *McHugh, C.*, 2009: Comparison of ADMS and AERMOD meteorological preprocessor and dispersion algorithms. Proc. Air Waste Manag. Assoc. Air Qual. Model. Next Gener. Model.

Chaumerliac, N., Richard, E., Pinty, J.-P., and *Nickerson, E. C.*, 1987: Sulfur scavenging in a mesoscale model with quasi-spectral microphysics: Two-dimensional results for continental and maritime clouds. *J. Geophys. Res. Atmos. 92*, 3114–3126.

Cohard, J., Pinty, J., and *Bedos, C.*, 1998: Extending Twomey's analytical estimate of nucleated cloud droplet concentrations from CCN spectra. *J. Atmos. Sci., 55,* 3348–3357.

Cohard, J.-M. and *Pinty, J.-P.*, 2000: A comprehensive two-moment warm microphysical bulk scheme. I: Description and tests. *Q. J. Roy. Meteorol. Soc. 126*, 1815–1842.

Csanady, G. T., 1973: Turbulent diffusion in the environment. D. Reidel Pub. Co.,.

Davidson, G. A., 1989: Simultaneous trajectory and dilution predictions from a simple integral plume model. *Atmos. Environ. 23*, 341–349.

Davidson, G. A., 1994: Dimensionless correlations for buoyant plume behaviour in cross-flows and scaling criteria for physical modeling of dispersion processes. *J. Wind Eng. Ind. Aerodyn. 51*, 135–155.

Feingold, G., Stevens, B., Cotton, W. R., and *Walko, R. L.*, 1994: An explicit cloud microphysics/LES model designed to simulate the Twomey effect. *Atmos. Res. 33*, 207–233.

Gangoiti, G., Sancho, J., Ibarra, G., Alonso, L., García, J. A., Navazo, M., Durana, N., and *Ilardia, J. L.*, 1997: Rise of moist plumes from tall stacks in turbulent and stratified atmospheres. *Atmos. Environ. 31*, 253–269.

Grabowski, W. W., 2006: Indirect impact of atmospheric aerosols in idealized simulations of convective – radiative quasie quilibrium. *J. Clim. 19*, 4664–4682.

Grabowski, W. W., and *Clark, T. L.*, 1991: Cloud–environment interface instability: Rising thermal calculations in two spatial dimensions. *J. Atmos. Sci. 48*, 527–546.

Grabowski, W. W., and *Smolarkiewicz, P. K.*, 1996: Two-time-level semi-Lagrangian modeling of precipitating clouds. *Mon. Weather Rev. 124*, 487–497.

Greig, J. E., Carnie, J. A., Tallis, G. F., Ryan, N. J., Tan, A. G., Gordon, I., Zwolak, B., Leydon, J. A., Guest, C. S., and *Hart, W. G.*, 2004: An outbreak of Legionnaires' disease at the Melbourne Aquarium, April 2000: Investigation and case-control studies. *Med. J. Aust. 180*, 566–572.

Hanna, S. R., 1972: Rise and condensation of large cooling tower plumes. *J. Appl. Meteorol. 11*, 793–799.

Hanna, S. R., 1976: Predicted and observed cooling tower plume rise and visible plume length at the John E. Amos power plant. *Atmos. Environ. 1967 10*, 1043–1052.

Hanna, S. R., Briggs, G. A., and Hosker, R. P. J., 1982: *Handbook on Atmospheric Diffusion.*

Huff, F. A., 1972: Potential augmentation of precipitation from coolingtower effluents. *Bull. Am. Meteorol. Soc. 53*, 639–644.

Janicke, U., and Janicke, L., 2001: A three-dimensional plume rise model for dry and wet plumes. *Atmos. Environ. 35*, 877–890.

Kessler, E., 1969: On the distribution and continuity of water substance in atmospheric circulations. *Meteor. Monogr., Amer. Meteor. Soc. No. 32*, 84.

Klaassen, G. P. and *Clark, T. L.*, 1985: Dynamics of the cloud-environment interface and entrainment in small cumuli: Two-dimensional simulations in the absence of ambient shear. *J. Atmos. Sci. 42*, 2621–2642.

Kloppers, J. C. and *Kröger, D. G.*, 2005: Influence of temperature inversions on wet-cooling tower performance. *Appl. Therm. Eng. 25*, 1325–1336.

Kogan, Y. L., 1991: The simulation of a convective cloud in a 3-D model with explicit microphysics. part I: Model description and sensitivity experiments. *J. Atmos. Sci. 48*, 1160–1189.

Kristóf, G. and *Balogh, M.*, 2010: Fine scale simulation of turbulent flows in urban canopy layers. *Időjárás 114*, 135–148.

Kristóf, G., Rácz, N., and *Balogh, M.*, 2009: Adaptation of pressure based CFD solvers for mesoscale atmospheric problems. *Bound.-Lay. Meteorol. 131*, 85–103.

Lasher-trapp, S. G., Cooper, W. A., and *Blyth, A. M.*, 2005: Broadening of droplet size distributions from entrainment and mixing in a cumulus cloud. *Q. J. Roy. Meteorol. Soc. 131*, 195–220.

Van Leer, B., 1979: Towards the ultimate conservative difference scheme. V. A second-order sequel to Godunov's method. *J. Comput. Phys. 32*, 101–136.

Lewis, W. K., 1922: The evaporation of liquid into gas. *Trans ASME 44*, 325–340.

Lohasz, M. M., and *Csaba, G.*, 2012: Investigation of exit loss of cooling towers at different wind speeds and Archimedes numbers. Proceeding of THMT-12. Proceedings of the Seventh International Symposium On Turbulence, Heat and Mass Transfer Palermo, Italy, 24-27 September, 2012, Connecticut, Begellhouse, 11.

Lucas, M., Martínez, P. J., Ruiz, J., Kaiser, A. S., and *Viedma, A.*, 2010: On the influence of psychrometric ambient conditions on cooling tower drift deposition. *Int. J. Heat Mass Transf. 53*, 594–604.

Margolin, L., Reisner, J. M., and *Smolarkiewicz, P. K.*, 1997: Application of the volume-of-fluid method to the advection–condensation problem. *Mon. Weather Rev. 125*, 2265–2273.

Mcalpine, J. D. and *Ruby, M.*, 2004: Using CFD to study air quality in urban microenvironments. Environmental Sciences and Environmental Computing. Vol. II, P. Zannetti, Ed., Vol. II of, The EnviroComp Institute, 1–31.

Meroney, R., 2006: CFD prediction of cooling tower drift. *J. Wind Eng. Ind. Aerodyn. 94*, 463–490.

Mochida, A., Murakami, S., Ojima, T., Kim, S. J., Ooka, R., and *Sugiyama, H.*, 1997: CFD analysis of mesoscale climate in the Greater Tokyo area. *J. Wind Eng. Ind. Aerodyn. 67-8*, 459–477.

Mokhtarzadeh-Dehghan, M. R., König, C. S., and *Robins, a. G.*, 2006: Numerical study of single and two interacting turbulent plumes in atmospheric cross flow. *Atmos. Environ. 40*, 3909–3923.

Morrison, H., Curry, J. A., and *Khvorostyanov, V. I.*, 2005: A new double-moment microphysics parameterization for application in cloud and climate models. Part I: description. *J. Atmos. Sci. 62*, 1665–1677.

Moussiopoulos, N., 2010: Air quality in cities: SATURN: EUROTRAC-2 Subproject final report. Springer, Berlin,.

Netterville, D. D. J., 1990: Plume rise, entrainment and dispersion in turbulent winds. *Atmos. Environ. Part A. Gen. Top. 24*, 1061–1081.

Olesen, H. R., Berkowicz, R., Ketzel, M., and *Løfstrøm, P.*, 2007: Validation of OML, AERMOD/PRIME and MISKAM using the Thompson wind tunnel data set for simple stack-building configurations. 6th International Conference on Urban Air Quality, Cyprus, March 27-29, 2007.

Ooka, R., Sato, T., Harayama, K., Murakami, S., and *Kawamoto, Y.*, 2010: Thermal energy balance analysis of the Tokyo metropolitan areausing a mesoscale meteorological model incorporating anurban canopy model. *Bound.-Lay. Meteorol. 138*, 77–97.

Otte, T. L., Lacser, A., Dupont, S., and *Ching, J. K. S.*, 2004: Implementation of an urban canopy parameterization in a mesoscale meteorological model. *J. Appl. Meteorol. 43*, 1648–1665.

Overcamp, T. J, and *Hoult, D. P.*, 1971: Precipitation in the wake of cooling towers. *Atmos. Environ. 5*, 751–765.

Paluch, I. R., and *Knight, C. A.*, 1984: Mixing and the evolution of cloud droplet size spectra in a vigorous continental cumulus. *J. Atmos. Sci. 41*, 1801–1815.

Petersen, R. L., 2004: ISC3 and PRIME versus wind tunnel observations for a power plant with hyperbolic cooling towers. 13th Conference on the Applications of Air Pollution Meteorology, Fifth Conference on Urban Environment, Vancouver, BC 23-26 August 2004.

Pinsky, M. B., and Khain, A. P., 2002: Effects of in-cloud nucleation and turbulence on droplet spectrum formation in cumulus clouds. *Q. J. Roy. Meteor. Soc. 128*, 501–533.

Policastro, A. J., Dunn, W. E., Breig, M., and *Ziebarth, J.*, 1978: Comparison of ten drift deposition models to field data acquired in the Chalk Point dry tracer experiment. Environmental Effects of Cooling Tower Plumes, Symposium on (Supplement),May 2-4, 1978, U. ofMaryland, 76–84.

Policastro, A. J., Dunn, W. E., and *Carhart, R. A.*, 1994: A model for seasonal and annual cooling tower impacts. *Atmos. Environ. 28*, 379–395.

Presotto, L., Bellasio, R., and *Bianconi, R.*, 2005: Assessment of the visibility impact of a plume emitted by a desulphuration plant. *Atmos. Environ. 39*, 719–737.

Pruppacher, H. R., Klett, J. D., and *Wang, P. K.*, 1998: Microphysics of Clouds and Precipitation. *Aerosol Sci. Technol. 28*, 381–382.

Rácz, N., Kristóf, G., and *Weidinger, T.*, 2013: Evaluation and validation of a CFD solver adapted to atmospheric flows: Simulation of topography-induced waves. *Időjárás 117*, 239–275.

Richard, E., and *Chaumerliac, N.*, 1989: Effects of different rain parameterizations on the simulation of mesoscale orographic precipitation. *J. Appl. Meteorol. 28*, 1197–1212.

Robinson, C. S., 1923: The design of cooling towers. *Mech Eng 15*, 99–102.

Schatzmann, M., and *Policastro, A. J.*, 1984: An advanced integral model for cooling tower plume dispersion. *Atmos. Environ. 18*, 663–674.

Schulman, L. L., Strimaitis, D. G., and *Scire, J. S.*, 1997: Addendum to ISC3 user's guide: the prime plume rise and building downwash model.

Shih, T. H., Liou, W. W., Shabbir, A., Yang, Z., and *Zhu, J.*, 1994: A new k-epsilon eddy viscosity model for high Reynolds number turbulent flows: Model development and validation. *Comput. Fluids 24*, 227–238.

Slawson, P. R. and *Csanady, G. T.*, 1967: On the mean path of buoyant, bent-over chimney plumes. *J. Fluid Mech. 28*, 311–322.

Spillane, K. T. and *Elsum, C. C.*, 1983: Prediction of cloud effects in chimney plumes. *Atmos. Environ. 17*, 983–990.

Sturman, A. and *Zawar-Reza, P.*, 2011: Predicting the frequency of occurrence of visible water vapour plumes at proposed industrial sites. *Atmos. Environ. 45*, 2103–2109.

Su, C.-W., Krueger, S. K., McMurtry, P. A., and *Austin, P. H.*, 1998: Linear eddy modeling of droplet spectral evolution during entrainment and mixing in cumulus clouds. *Atmos. Res. 47–48*, 41–58.

Twomey, S., 1959: The nuclei of natural cloud formation part II: The supersaturation in natural clouds and the variation of cloud droplet concentration. *Geofis. Pura e Appl. 43*, 243–249.

Tyagi, S. K., Pandey, a. K., Pant, P. C., and *Tyagi, V. V.*, 2012: Formation, potential and abatement of plume from wet cooling towers: A review. *Renew. Sustain. Energy Rev. 16*, 3409–3429.

Wang, J., Wang, S., Xu, X., and *Xiao, F.*, 2009: Evaluation of alternative arrangements of a heat pump system for plume abatement in a large-scale chiller plant in a subtropical region. *Energy Build. 41*, 596–606.

Wang, S. W., Tyagi, S. K., Sharma, A., and *Kaushik, S. C.*, 2007: Application of solar collectors to control the visible plume from wet cooling towers of a commercial building in Hong Kong: A case study. *Appl. Therm. Eng. 27*, 1394–1404.

Warner, J., 1969: The microstructure of cumulus cloud. Part I. general features of the droplet spectrum. *J. Atmos. Sci. 26*, 1049–1059.

Wei, Q. D., Zhang, B. Y., Liu, K. Q., Du, X. D., and *Meng, X. Z.*, 1995: A study of the unfavorable effects of wind on the cooling efficiency of dry cooling towers. *J. Wind Eng. Ind. Aerodyn. 54-55*, 633–643.

Weil, J. C., 1974: The Rise of moist, buoyant plumes. *J. Appl. Meteorol. 13*, 435–443.

Wigley, T. M. L., and *Slawson, P. R.*, 1971: On the condensation of buoyant, moist, bent-over plumes. *J. Appl. Meteorol. 10*, 253–259.

Xu, X., Wang, S., and *Ma, Z.*, 2008: Evaluation of plume potential and plume abatement of evaporative cooling towers in a subtropical region. *Appl. Therm. Eng. 28*, 1471–1484.

Yamada, T., 2003: Numerical simulation of airflows around buildings by using a mesoscale atmospheric model. Air & Waste Management Associations 96th Annual Conference and Exhibition, San Diego, California, June 23 - 25, 2003, San Diego, California.

Ziegler, C. L., 1985: Retrieval of thermal and microphysical variables in observed convective storms. Part 1: Model development and preliminary testing. *J. Atmos. Sci. 42*, 1487–1509.

IDŐJÁRÁS

Quarterly Journal of the Hungarian Meteorological Service
Vol. 120, No. 2, April – June, 2016, pp. 255–264

Correlation analysis of tilted and horizontal photovoltaic panel's electricity generation and horizontal global radiation

Miklós Horváth* and **Tamás Csoknyai**

Department of Building Services and Process Engineering,
Budapest University of Technology and Economics,
Műegyetem rkp. 3-9., 1111 Budapest, Hungary

*Corresponding author E-mail: horvath@epgep.bme.hu

(Manuscript received in final form June 3, 2015)

Abstract—Present paper aims at analyzing the correlation between global radiation and electricity production of photovoltaic (PV) panels. In case of high correlation, the electricity production can be estimated by the measured or predicted global radiation. Such solution can be applied for forecast purposes if global radiation data are available. On the other hand, global radiation can be measured based on the performance of a small and cheap PV system, which can be a reasonable solution if global radiation data is not available and a high precision monitoring system is too expensive.

The study is based on on-site measurements for the period of four months. At the station, seven PV panels are installed with different orientation and tilt angle and their electricity production is registered. The solar radiation is measured with a pyranometer. In the first group, there are four PV panels. One is placed horizontally and the other three are placed with a tilt angle of 45°. In the second, three-panel group the panels are placed with 90° tilt angle. The station is located in Debrecen, Hungary and the paper focuses on the Hungarian climatic conditions.

The research proves that the correlation strongly depends on the orientation and the tilt angle of the panel, and for prediction and estimation purposes the 45° tilted, south oriented surface is the most recommended option.

Key-words: PV panels, electricity production, energy performance, monitoring, global radiation, on-site monitoring, daily courses of electricity production

1. Introduction

For PV system installations it is fundamental to estimate the energy output of the systems. In most cases PV panels are placed with optimized tilt angle and orientation. A four-step optimization is described by Mehleri et al. (*Mehleri et al.*, 2010). The first step of the optimization process is to select the best performing diffuse radiation model to calculate the radiation components. As a second step, the global radiation can be calculated from the previously calculated radiation components for any tilt angle and orientation. As a third step, linear regression and RBF (radial basis-function) are applied to identify the best fitting model for the measured global radiation data. Further on, this model was used for the calculations. As a fourth step, a nonlinear programming (NLP) problem is formulated taking into account constraints and limitations of the system.

In several cases, the PV panels cannot be optimally tilted and as a result are oriented simply according to the site conditions. Several papers were published on this issue. A case study on a Korean office building was made by Hwang et al. *(Hwang et al.*, 2012). In that paper different options were examined focusing on the energy output of the BIPV (building integrated PV) arrays. The aim of the study was to determine the maximal electricity production for different tilt angles and orientations along with the effect of the installation distance to module length ratio. The study found that "it is efficient to install BIPV systems at a horizontally inclined angle of 60° and a vertically inclined angle that is smaller than 15°".

A different research was conducted in Australia, where PV production was measured at different tilt angles and orientations (*Yan et al.*, 2013). The measured electricity output was compared to calculated data, and the results showed that the chosen model was acceptable, thus further calculations and optimization were made. Based on the measurements and calculations, the yearly system efficiency and energy output for different orientations and the optimal tilt angle and orientation were determined.

Further parametric analysis was carried out by Bhattacharya et al. in Rajasthan, India (*Bhattacharya et al.*, 2014). The aim of the research was to perform PV output modeling under the climatic conditions of India. The effect of orientation, tilt angle, temperature, and humidity on the PV system efficiency and energy output was examined. The meteorological parameters were collected from five different stations, and the effect of orientation and tilt angle was examined by applying model calculations. The conducted research included determination of optimal orientation and tilt angle.

Further research was conducted by *Ding et al.* for three different stations, from which two were located in the USA and the third one in Kenya, Africa (*Ding et al.*, 2015). In the paper, different PV types and ways of their installation were examined and their effect on the PV system output and efficiency was monitored. They proved that by using the optimal orientation and tilt angle, the output of the system can be increased by 30%. As a result of PV type investigations, it was

clearly visible that not optimal placement of PV panels in some cases can lead to significant drop in the system efficiency. Consequently, for such panels, imperfect installation must be avoided.

Mulcué-Nieto and Mora-López examined the effect of orientation and tilt angle of PV panels at several stations in Columbia and Spain *(Mulcué-Nieto* and *Mora-López,* 2015). As a result of the research, it was concluded, that in case of nation-wide characterization it is necessary to divide the country into appropriate zones. In case of Columbia, the zone borders were defined by longitudes. In each zone, the incoming solar energy was calculated for big cities within the region. The results were taken as an average for the given area. The results also showed that the effect of orientation is smaller in countries which are exposed to higher diffuse radiation.

In case of nearly zero energy buildings (NZEB), it is important to utilize the renewable energies to a high extent. Sánchez and Izard performed a research aiming at the determination of energy yield of PV panels placed on the external walls of buildings (*Sánchez* and *Izard,* 2015). The measurement was performed on southwest facing façades. In addition, four other orientations were also modeled. It was concluded, that in the case of PV panels placed on the southwest side of the building, a more balanced and stable electricity output is produced, which better fits the electricity consumption.

The aim of this paper is to determine the electricity production of different PV panel installations under climatic conditions of Hungary. The output of PV panels is also compared to the global radiation measured on a horizontal surface. In the paper, the measurement station is described along with its limitations.

2. Measurement station

The measurement station is located in Debrecen, Hungary, in the 'Megújuló Energiapark' (4031 Debrecen, Kishegyesi út 187.). The solar radiation is measured with a KIPP & ZONEN CM-3 pyranometer, which is placed at 2 m above the ground (*Fig. 1*). The radiation measuring device is connected to a Campbell CR 1000 data logger. The sample rate of the device is 1 s, which is collected by the data logger. The data logger from the 1 s data calculates 10 min averages. The data logger is connected to a server through an Ethernet interface (NL120), and sends data every 10 minutes.

At the station the PV panels are installed in two groups (*Fig. 2*). The installed PV panels are Istar Solar® IS4000P, with 210 W peak power. The manufacturer's catalog claims a maximal efficiency of 15.4% for these panels. There are four PV panels in the first group. One is placed horizontally and the other three are placed with a tilt angle of 45°. The inclined PV panels are oriented to the east, south and west. In the second group, three panels are placed with 90° tilt angle facing towards east, south and west. The beginning of data

logging was September 20, 2014. The electricity output of PV panels is measured and logged every 10 minutes.

In this paper, data from September 20, 2014 to January 18, 2015 were analyzed. The measured data were first processed in order to exclude errors, and then statistical analysis was performed for the filtered data.

Fig. 1. The KIPP & ZONEN CM-3 pyranometer at the station.

Fig. 2. The PV arrays at the station.

3. Measured data and statistical analysis

3.1. Correlation of PV electricity production and global radiation measured on a horizontal plane

The daily average of global radiation and PV output of the horizontal PV panel for the entire period of monitoring are shown in *Fig. 3*. From the figure it can be seen, that the electricity output is at least twice as high as the output in December and January.

Based on the measured output of the horizontal PV panel and the global radiation, the calculated average efficiency of the PV panel is 14%. The calculated daily maximum efficiency was 19%, whilst the lowest was nearly 0%. The actual maximal daily efficiency was higher than the PV panel's maximum efficiency of 15.4% given by the manufacturer. The reason for the higher efficiency is possibly a result of a shading obstruction on the global radiation measurement device. This resulted in a lower value of measured global radiation, while the unshaded PV panels production was not lower. The calculated correlation coefficient of the measured global radiation and PV output was 0.930.

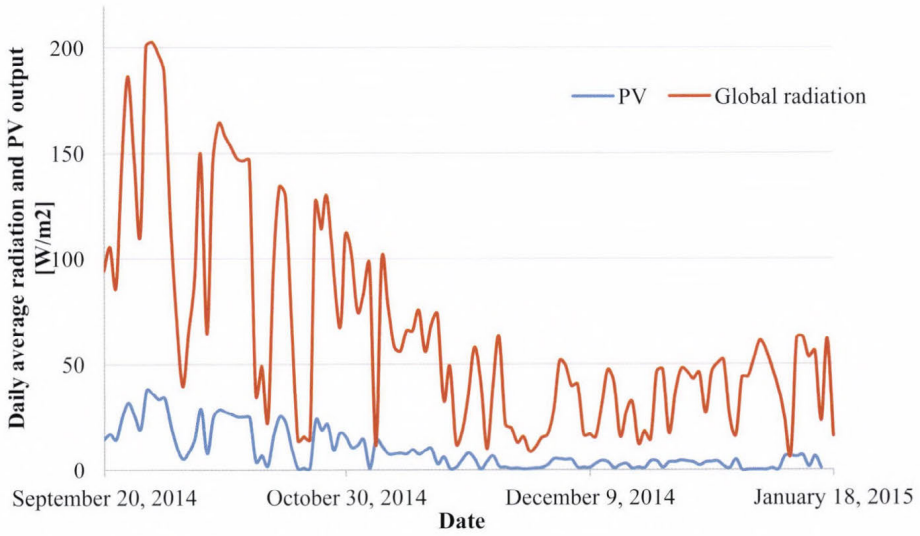

Fig. 3. Daily average of global radiation and PV output.

3.2. *Comparison of the outputs of tilted, oriented and horizontally installed PV panels*

The output of different PV panels are shown in *Table 1*. The table shows that with PV panels oriented to the south, more energy can be produced, than with a horizontally placed PV panel. The results also show that the biggest energy yield in the autumn-winter period is on a 90° tilted, south oriented panel, due to the low solar altitude. On the East oriented surface the incoming energy was nearly equal to the energy output of the horizontal panel. The east and west oriented, 45° tilted panels could produce acceptable amount of electricity, however, the 90° tilted panels oriented the same way have low energy output. Based on the values of correlation coefficients, it can be concluded that only the 45° tilted, south oriented PV panel has similar production profile to the horizontal one. The other panels show significant differences, thus they cannot be characterized by the horizontal panel.

Table 1. The produced electricity and calculated correlation coefficient for each PV panel in comparison with the horizontal panel's measurement data

	0°	**S45°**	**S90°**	**E45°**	**E90°**	**W45°**	**W90°**
Produced electricity [%]	100	119.6	136.1	101.3	47.9	72.9	39.6
Correlation [–]	1	0.930	0.818	0.853	0.556	0.758	0.300

For the measurement period, the daily average output profile was developed for every month for every panel. *Fig. 4* shows the daily average electricity output for the horizontally placed PV panel. The daily electricity production drops by 75% in the winter months compared to the daily data of September. This is due to the lower solar altitude and the higher fraction of diffuse radiation during winter.

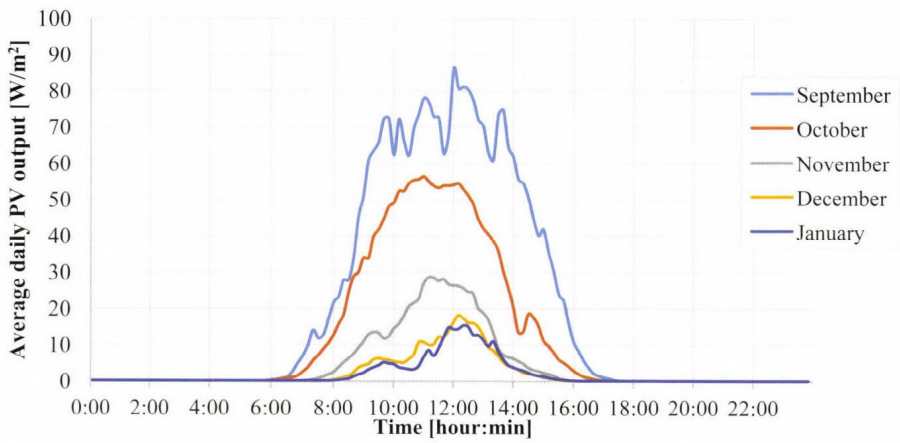

Fig. 4. Daily average electricity output of the horizontal PV panel.

The electricity output of the south oriented PV panels is shown in *Fig. 5* and *Fig. 6*. From the figures it can be seen that in case of south oriented panels, the daily electricity output is nearly symmetrical. In *Fig. 6* it is presented that in December and January in the morning and afternoon, small peaks occur at the low solar altitude. These small peaks can be results of a shading object, as in case of the 45° tilted surface, these peaks do not occur.

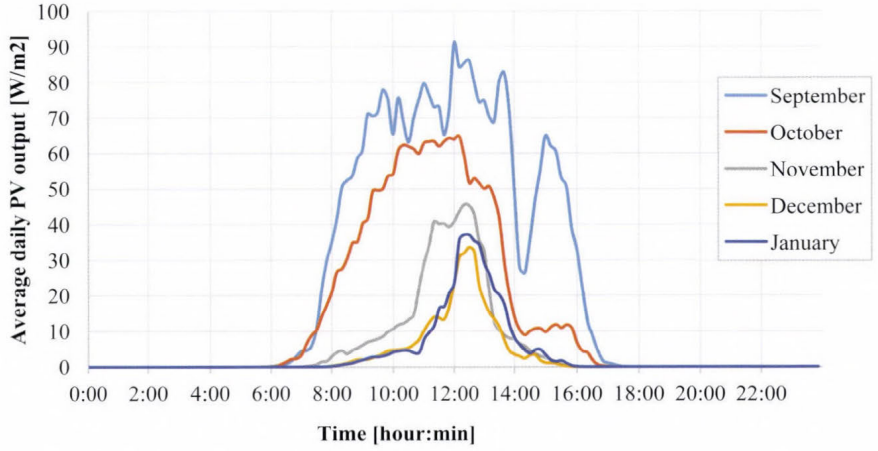

Fig. 5. Daily average electricity output of the 45° tilted, south oriented PV panel.

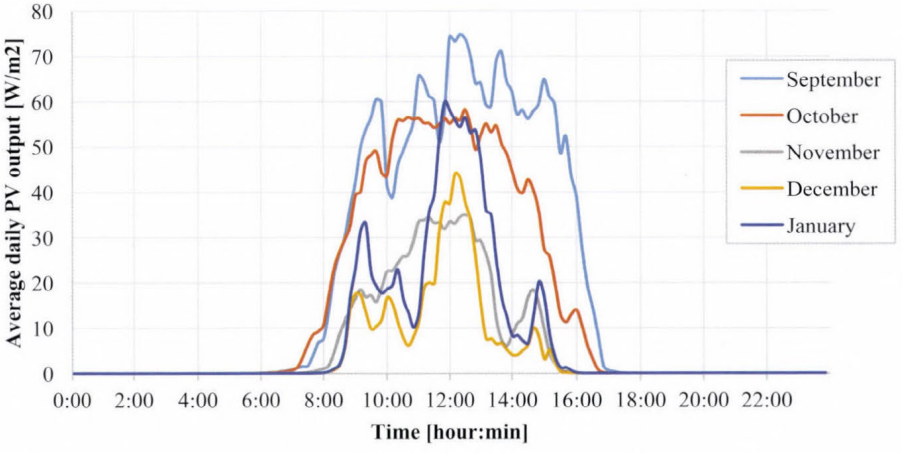

Fig. 6. Daily average electricity output of the 90° tilted, south oriented PV panel.

For east oriented PV panels, the daily electricity profiles are shown on *Fig. 7* and *Fig. 8*. On the 45° tilted panel, the highest energy output can be seen before 14:00, in case of the 90° tilted panel, the peak of the output can be found around 10:00. In case of the 45° tilted panel, a setback occurs in every month except October, this can be a result of shading objects. For the 90° tilted panel, the peak of electricity production is in the morning, when the panel is receiving direct sunlight, whilst in the afternoon the panel can not utilize the incoming diffuse radiation.

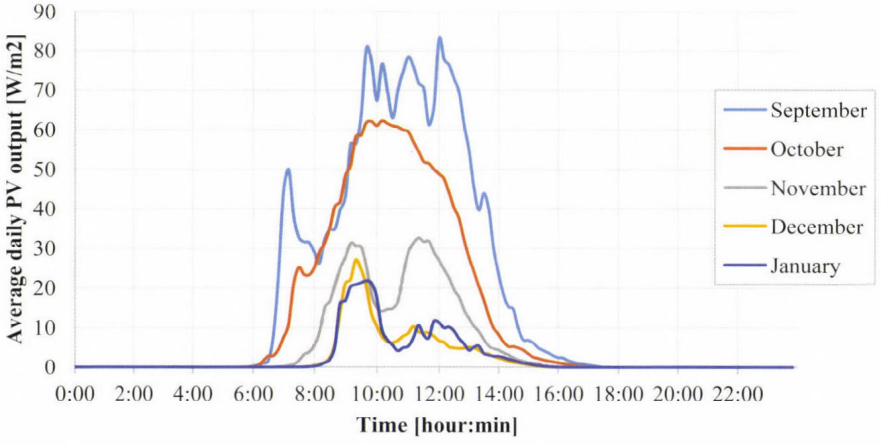

Fig. 7. Daily average electricity output of the 45° tilted, east oriented PV panel.

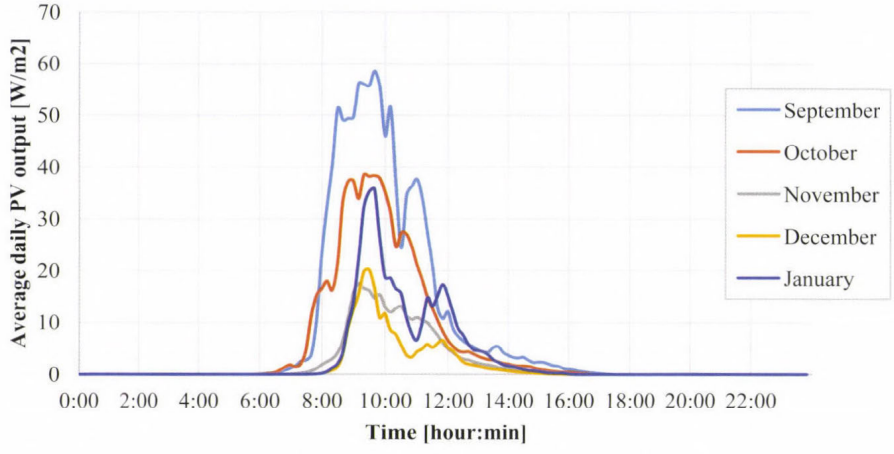

Fig. 8. Daily average electricity output of the 90° tilted, east oriented PV panel.

The average daily electricity output of west oriented surfaces are shown in *Fig. 8* and *Fig. 9*. For the west oriented surfaces nearly the same conclusions can be made as for the east oriented surfaces. The only significant difference is the time of the highest production, which, in case of west oriented surfaces, occurs in the afternoon. In *Fig. 8* it is visible, that after 12:00, the output of the panel experiences a setback which could be a result of a shading object. This problem in September is not occurring, possibly due to higher solar altitude. In *Fig. 9*, for the 90° tilted panel this setback is not visible, which also proofs the theory of the shading object.

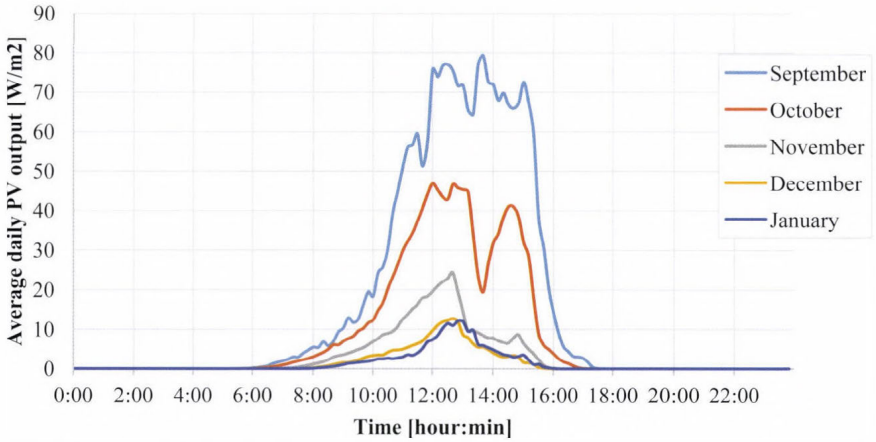

Fig. 8. Daily average electricity output of the 45° tilted, west oriented PV panel.

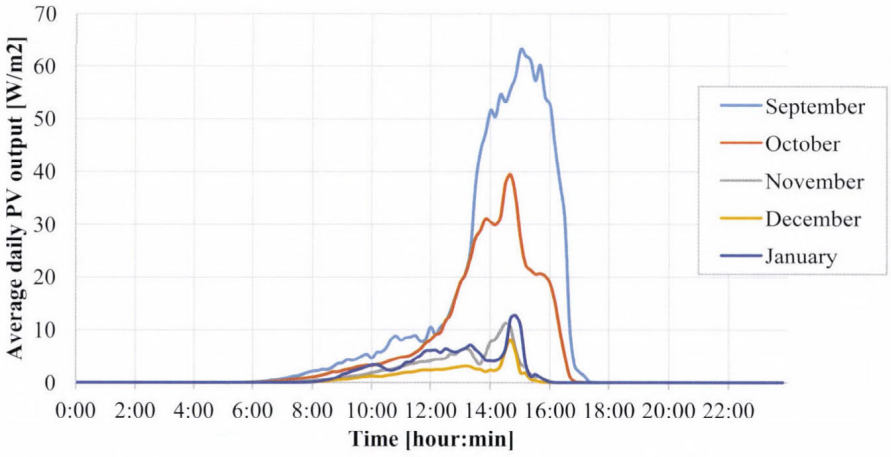

Fig. 9. Daily average electricity output of the 90° tilted, west oriented PV panel.

4. Summary

In this paper, a PV panel measurement station was described and the measured data from this station was statistically analyzed. The Hungarian station is unique due to the fact that at this station the outputs from differently oriented and tilted PV panels and global radiation are measured at the same time.

From the data measured it was concluded that, in case of the horizontally installed PV panel, the average efficiency is 14%. The correlation coefficient of the horizontal PV output and the measured global radiation is 0.930. This correlation coefficient proves linear correlation between the two datasets.

In the paper the measured PV outputs were compared. According to the measurement, in the autumn-winter period the highest energy yield is on the vertical, south oriented PV panel. Compared to the horizontal PV panel, only the south oriented panels have higher energy output in the measurement period.

Based on the values of correlation coefficients, it can be concluded that only the 45° tilted, south oriented PV panel has similar production profile to the horizontal one. The other panels show significant differences, thus they cannot be characterized by the horizontal panel.

References

Bhattacharya, P., Dey, S., and *Mustaphi, B.*, 2014: Some Analytical Studies on the Performance of Grid Connected Solar Photovoltaic System with Different Parameters. *Procedia Materials Science 6*, 1942–1950.

Ding, Y., Young, M., Zao, Y., Traverse, C., Benard, A., and *Lunt, R.R.*, 2015. Influence of photovoltaic angle-dependence on overall power output for fixed building integrated configurations. *Sol. Ener. Mat. Sol. C. 132*, 523–527.

Hwang, T., Kang, S. and *Kim, J.T.*, 2012. Optimization of the building integrated photovoltaic system in office buildings. Focus on the orientation, inclined angle and installed area. *Energ. Buildings 46*, 92–104.

Mehleri, E.D., Zervas, P.L., Sarimveis, H., Palyvos, J.A., and *Markatos, N.C.*, 2010. Determination of the optimal tilt angle and orientation for solar photovoltaic arrays. *Renew. Energ. 35*, 2468–2475.

Mulcué-Nieto, L.F. and *Mora-López, L.*, 2015. Methodology to establish the permitted maximum losses due to shading and orientation in photovoltaic applications in buildings. *Appl. Energ.* 137, 37–45.

Sánchez, E. and *Izard, J.*, 2015. Performance of photovoltaics in non-optimal orientations: An experimental study. *Energ. Buildings 87*, 211–219.

Yan, R., Saha, T.K., Meredith, P., and *Goodwin, S.*, 2013. Analysis of yearlong performance of differently tilted photovoltaic systems in Brisbane, Australia. *Energ. Convers. Manage. 74*, 102–108.

NEWS

IN MEMORIAM ISTVÁN MATYASOVSZKY (1960–2015)

István Matyasovszky died suddenly at his family's home in Érd at Christmas tim, on December 25, 2015. He was only 55. He is survived by his wife, Ildikó Simon; an adult daughter, Csilla, and younger twin daughters, Emma and Nelli who surely foresee difficult years without their father.

István Matyasovszky graduated as a meteorologist at the Eötvös Loránd University in 1984 with the second large group of students (altogether 15) having meteorology as a unique major subject. Most of his fellow graduated students are still working for the Hungarian Meteorological Service (e.g., Ákos Horváth, István Ihász, Márta Puskás, László Tölgyesi, and Szilvia Jenki). He started to work for the Department of Meteorology right after the graduation, and two years later he obtained the title of dr.univ. with a dissertation on the analysis of the statistical structure of the long temperature time series of Central England. He spent his entire academic career at the Eötvös Loránd University, first as a researcher, then, as assistant professor (from 1990), and finally as associate professor (since 1997). From 1991 to 1995 he spent 30 months at the University of Nebraska-Lincoln as visiting scientist, where he made joint research with Prof. István Bogárdi.

His main expertise was statistical climatology, to which Ottó Gulyás (a mathematician from the Hungarian Meteorological Service teaching generations of students) introduced him. He made detailed research on statistical climatology, i.e., time series analysis, spectral analysis, climate variability and change. He published his results in high quality meteorology-related journals, e.g., Journal of Geophysical Research, Theoretical and Applied Climatology, Climate Research, Atmospheric Environment, International Journal of Biometeorology, Meteorologische Zeitschrift. Altogether he had 51 and 30 research papers in English in international and Hungarian journals, respectively. He regularly sent interesting manuscripts to Időjárás, where he published a total of 19 journal papers. For his publications he was granted by the Szádecky-Kardoss Elemér Award in 1996 and 1997. In addition, the Hungarian Meteorological Society awarded him the Róna Zsigmond Award in 1992, and the Hungarian Academy of Science granted him the Bolyai János Fellowship during 1998-2001. He authored the book titled Statistical Climatology, which is a well-written basis for current students and anyone interested in the common scientific area of mathematics and climatology. For his great contribution to the national research and university teaching in meteorology, he received the Pro Meteorologia Award in 2005. His influence on meteorology-related research is very high, which is illustrated by the high number of independent citations (752 according to MTMT). In 2015, he obtained the DSc degree of the Hungarian

Academy of Science with his dissertation on new statistical methodologies applied to climatological studies.
He died unexpectedly, unpredictably – he was not ill. The recent years were probably the most happy and successful period both in his private life with having a supporting wife and two small children, and his academic career with completed DSc degree. He could have several decades ahead being spent in peace with his family, achieving more research goals with great success, and teaching several more generations of students to statistical climatology... We will surely miss István and will preserve his legacy at the Department of Meteorology at the Eötvös Loránd University.

Judit Bartholy

INSTRUCTIONS TO AUTHORS OF *IDŐJÁRÁS*

The purpose of the journal is to publish papers in any field of meteorology and atmosphere related scientific areas. These may be

- research papers on new results of scientific investigations,
- critical review articles summarizing the current state of art of a certain topic,
- short contributions dealing with a particular question.

Some issues contain "News" and "Book review", therefore, such contributions are also welcome. The papers must be in American English and should be checked by a native speaker if necessary.

Authors are requested to send their manuscripts to

Editor-in Chief of IDŐJÁRÁS
P.O. Box 38, H-1525 Budapest, Hungary
E-mail: journal.idojaras@met.hu

including all illustrations. MS Word format is preferred in electronic submission. Papers will then be reviewed normally by two independent referees, who remain unidentified for the author(s). The Editor-in-Chief will inform the author(s) whether or not the paper is acceptable for publication, and what modifications, if any, are necessary.

Please, follow the order given below when typing manuscripts.

Title page: should consist of the title, the name(s) of the author(s), their affiliation(s) including full postal and e-mail address(es). In case of more than one author, the corresponding author must be identified.

Abstract: should contain the purpose, the applied data and methods as well as the basic conclusion(s) of the paper.

Key-words: must be included (from 5 to 10) to help to classify the topic.

Text: has to be typed in single spacing on an A4 size paper using 14 pt Times New Roman font if possible. Use of S.I. units are expected, and the use of negative exponent is preferred to fractional sign. Mathematical formulae are expected to be as simple as possible and numbered in parentheses at the right margin.

All publications cited in the text should be presented in the *list of references*, arranged in alphabetical order. For an article: name(s) of author(s) in Italics, year, title of article, name of journal, volume, number (the latter two in Italics) and pages. E.g., *Nathan, K.K.,* 1986: A note on the relationship between photosynthetically active radiation and cloud amount. *Időjárás 90,* 10-13. For a book: name(s) of author(s), year, title of the book (all in Italics except the year), publisher and place of publication. E.g., *Junge, C.E.,* 1963: *Air Chemistry and Radioactivity.* Academic Press, New York and London. Reference in the text should contain the name(s) of the author(s) in Italics and year of publication. E.g., in the case of one author: *Miller* (1989); in the case of two authors: *Gamov* and *Cleveland* (1973); and if there are more than two authors: *Smith et al.* (1990). If the name of the author cannot be fitted into the text: *(Miller,* 1989); etc. When referring papers published in the same year by the same author, letters a, b, c, etc. should follow the year of publication.

Tables should be marked by Arabic numbers and printed in separate sheets with their numbers and legends given below them. Avoid too lengthy or complicated tables, or tables duplicating results given in other form in the manuscript (e.g., graphs).

Figures should also be marked with Arabic numbers and printed in black and white or color (under special arrangement) in separate sheets with their numbers and captions given below them. JPG, TIF, GIF, BMP or PNG formats should be used for electronic artwork submission.

More information for authors is available: journal.idojaras@met.hu

Published by the Hungarian Meteorological Service

Budapest, Hungary

INDEX 26 361

HU ISSN 0324-6329